RADAR CROSS SECTION REDUCTION OF CYLINDRICAL CAVITIES USING RAY-TRACING METHOD

A THESIS SUBMITTED TO
THE GRADUATE SCHOOL OF NATURAL AND APPLIED SCIENCES
OF
MIDDLE EAST TECHNICAL UNIVERSITY

BY

YUSUF SEZGİN

IN PARTIAL FULFILLMENT OF THE REQUIREMENTS
FOR
THE DEGREE OF MASTER OF SCIENCE
IN
ELECTRICAL AND ELECTRONIC ENGINEERING

MAY 2022

Approval of the thesis:

RADAR CROSS SECTION REDUCTION OF CYLINDRICAL CAVITIES USING RAY-TRACING METHOD

submitted by **YUSUF SEZGİN** in partial fulfillment of the requirements for the degree of **Master of Science** i**n Electrical and Electronic Engineering, Middle East Technical University** by,

Prof. Dr. Halil Kalıpçılar
Dean, Graduate School of **Natural and Applied Sciences** _____

Prof. Dr. İlkay Ulusoy
Head of the Department, **Electrical and Electronics Eng.** _____

Prof. Dr. M. Gülbin Dural Ünver
Supervisor, **Electrical and Electronics Engineering, METU** _____

Examining Committee Members:

Prof. Dr. Mustafa Kuzuoğlu
Electrical and Electronics Engineering, METU _____

Prof. Dr. M. Gülbin Dural Ünver
Electrical and Electronics Engineering, METU _____

Prof. Dr. Özlem Aydın Çivi
Electrical and Electronics Engineering, METU _____

Prof. Dr. Sencer Koç
Electrical and Electronics Engineering, METU _____

Prof. Dr. Özlem Özgün
Electrical and Electronics Engineering, Hacettepe University _____

Date: 16.05.2022

I hereby declare that all information in this document has been obtained and presented in accordance with academic rules and ethical conduct. I also declare that, as required by these rules and conduct, I have fully cited and referenced all material and results that are not original to this work.

Name Last name : Yusuf Sezgin

Signature :

ABSTRACT

RADAR CROSS SECTION REDUCTION OF CYLINDRICAL CAVITIES USING RAY-TRACING METHOD

Sezgin, Yusuf
Master of Science, Electrical and Electronic Engineering
Supervisor : Prof. Dr. Mevlüde Gülbin Dural Ünver

May 2022, 140 pages

Low observability technology, which aims to make it difficult to be detected, tracked, and hit by the enemy forces is one of the most critical technologies for 5th generation fighter aircraft. Low observability in Radio Frequency (RF) band is achieved by minimizing the Radar Cross Section (RCS) of the aircraft at specific angular zones and frequencies. RCS is a quantity related to the amount of reflection of the incoming electromagnetic wave by the aircraft and it is generated by different scattering mechanisms. Scatterings due to specular reflections and diffraction can be directly controlled by angular alignment, geometric shaping, and radar absorbing material (RAM) applications. However, multiple reflection scatterings in the cavities cannot be directly controlled due to their chaotic nature. In this study, a basic Shooting and Bouncing Rays (SBR) tool is developed to calculate the RCS and it is aimed to reduce the RCS of cylindrical cavities by optimizing the cavity geometry and RAM performance with the help of the statistical outputs of the ray-tracing method.

Keywords: Ray-tracing, Shooting and Bouncing Rays (SBR), Radar Cross Section (RCS), Low Observability Technology, Cavity, Radar Absorbing Material (RAM)

ÖZ

IŞIN TAKİP YÖNTEMİ İLE SİLİNDİRİK KAVİTELERİN RADAR KESİT ALANI AZALTIMI

Sezgin, Yusuf
Yüksek Lisans, Elektrik ve Elektronik Mühendisliği
Tez Yöneticisi: Prof. Dr. Mevlüde Gülbin Dural Ünver

Mayıs 2022, 140 sayfa

Hava aracının düşman kuvvetleri tarafından tespitini, takibini ve vurulmasını zorlaştırmayı amaçlayan düşük görünürlük teknolojisi, 5. Nesil savaş uçakları için en kritik teknolojilerden biridir. Radyo Frekansı (RF) bantta düşük görünürlük, hava aracının belirli açısal bölgelerde ve frekanslarda Radar Kesit Alanı'nı (RKA) en düşük seviyeye getirerek sağlanır. RKA, gelen elektromanyetik dalganın uçak tarafından yansıtılma oranı ile ilgili bir niceliktir ve farklı saçılma mekanizmalarıyla oluşturulur. Direkt aydınlanma ve kırınıma bağlı saçılımları, açısal hizalama, geometrik şekillendirme ve radar soğurucu malzeme (RSM) uygulamaları ile doğrudan kontrol edebilmek mümkündür. Ancak kavitelerdeki çoklu yansımalar kaotik yapıları dolayısıyla doğrudan kontrol edilemezler. Bu çalışmada, RKA hesaplamak için temel bir Seken Işın Yöntemi (SIY) geliştirilmiş ve ışın takibi yönteminin istatiksiksel çıktıları ile kavite geometrisi ve RAM performansını en iyileştirerek silindirik kavitelerin RKA değerlerinin düşürülmesi amaçlanmıştır.

Anahtar Kelimeler: Işın Takibi, Seken Işın Yöntemi (SIY), Radar Kesit Alanı (RKA), Düşük Görünürlük Teknolojisi, Kavite, Radar Soğurucu Malzeme (RSM)

To my beloved wife

and our precious son.

ACKNOWLEDGMENTS

I would like to express my deepest gratitude to my supervisor Prof. Dr. M. Gülbin Dural Ünver, for her guidance, advice, criticism, encouragement, and insight throughout the research.

The support of my family should not be forgotten. I would like to thank my wife, Fatmanur, for her understanding and patience. I am grateful to her for the evenings she had to take care of our son, Kerem Sina, alone. Keeping our son, who loves his father the most, away from his father was never easy. Finally, I would like to thank my son Kerem Sina. Without him, I could have finished my thesis sooner, but I wouldn't have been so happy and satisfied when I did.

TABLE OF CONTENTS

ABSTRACT v

ÖZ vi

ACKNOWLEDGMENTS viii

TABLE OF CONTENTS ix

LIST OF TABLES xii

LIST OF FIGURES xiii

LIST OF ABBREVIATIONS xx

LIST OF SYMBOLS xxiii

1 INTRODUCTION 1

1.1 Purpose of the Study 1

1.2 Electromagnetic Wave Theory 2

1.3 Definition of RCS 4

1.4 Stealth or Low Observability 6

1.5 RCS Reduction Techniques: Geometry and Materials 7

1.6 RCS Computation: Analytical and Numerical Methods 11

1.7 RCS Scattering Mechanisms – Cavities 13

1.8 Ray-Tracing and SBR Method 16

1.9 Hypotheses Presented in the Study 18

2 LITERATURE REVIEW: RAY TRACING PROCESSES, RAY-TRIANGLE INTERSECTION ALGORITHMS, AND FIELD AND RCS CALCULATIONS 21

2.1 Launching Rays 21

2.2 Finding the Intersection Points 22

2.2.1 Badouel Algorithm 23
2.2.2 Möller – Trumbore Algorithm 26
2.3 Determining the Reflected Rays 29
2.4 Field Calculations 31
2.4.1 Planar Reflection Coefficient 32
2.4.2 Direction of Fields 35
2.4.3 Aperture and Backscattering Fields 38
3 CODING RAY TRACING ALGORITHM, GUI OF RAY TRACING TOOL AND FIELD AND RCS CALCULATION PROCESS 41
3.1 Coding Ray Tracing Algorithm 41
3.1.1 Inputs 41
3.1.2 The Decision of Ray Starting Points 44
3.1.3 The Decision of Intersection Points 45
3.1.4 Recursion 46
3.1.5 Outputs 47
3.2 GUI of Ray Tracing Tool 47
3.2.1 Inputs Tab 48
3.2.2 Outputs Tab 50
3.3 Field Calculations 53
4 CONVERGENCE TESTS 57
4.1 Mesh Size Tests 57
4.2 Ray Density Tests 60
4.3 Maximum Bounce Numbers Tests 63
4.4 RCS of basic geometries 66

4.4.1 Square Plate 66
4.4.2 Dihedral Corner Reflector 73
5 COMPARATIVE ANALYSIS OF DIFFERENT CYLINDRICAL CAVITY MODELS 83
5.1 Straight Cylindrical Cavity 86
5.2 Bended Cavity 89
5.3 Material Optimization Procedure 93
5.4 Analysis with Optimized Material 97
5.5 Bend in z-direction 102
5.6 Bend Location 106
5.7 Slope of Bend 115
6 CONCLUSION 131
6.1 Overall Results 131
6.2 Discussions and Conclusion 132
6.3 Future Works 135
REFERENCES 137
A. ARC Technologies Technical Data Sheets 139

LIST OF TABLES

TABLES

Table 1 Input parameters required for ray tracing algorithm 44
Table 2 Computation times for different mesh sizes 60
Table 3 Computation times for different ray densities 63
Table 4 Computation times for different bounce limits 64
Table 5 Average RCS values in dBsm of different cases for a square plate 72
Table 6 Average RCS values in dBsm of different cases for dihedral corner reflector 80
Table 7 Average RCS values in dBsm for different cases of Model_02 and Model_03 106
Table 8 Average RCS values in dBsm for different cases of Model_03, Model_04, and Model_05 114
Table 9 Average RCS values in dBsm for different cases of Model_06, Model_07, and Model_08 125
Table 10 Average RCS results in dBsm for the effect of bend slope 126
Table 11 The average RCS values in dBsm for different cases of Model_08 127
Table 12 The average RCS values in dBsm for both co-polarizations and cross polarizations of Model_08 and Model_08_v2 128
Table 13 Average RCS values in dBsm for all cases 131
Table 14 Maximum RCS values in dBsm for all cases 132

LIST OF FIGURES

FIGURES

Figure 1.1 RCS signature patterns for conventional (left) and low observable (right) aircraft 1
Figure 1.2 Monostatic (left) and bistatic (right) radar configurations 4
Figure 1.3. War scenario for a conventional aircraft 6
Figure 1.4. War scenario for a stealth aircraft..... 7
Figure 1.5 Conductive coating on F-22 Raptor canopy 8
Figure 1.6 Copper filled conductive sealant application between the CFRP panels 8
Figure 1.7 Angular alignment representations 9
Figure 1.8 Angular alignment on F-22 Raptor aircraft from front view..... 10
Figure 1.9 Angular alignment on representative geometry of F-22 Raptor aircraft from the side view..... 10
Figure 1.10 Absorption mechanism for RAMs..... 11
Figure 1.11 RAM application on J-20 aircraft..... 11
Figure 1.12. Classification of CEM solution methods..... 13
Figure 1.13 Normal reflection from a planar surface..... 14
Figure 1.14 Specular reflection from a tilted surface..... 14
Figure 1.15 Reflection from a curved surface..... 14
Figure 1.16 Surface traveling and creeping waves 14
Figure 1.17 Diffraction from edges and tip points..... 15
Figure 1.18 Cavity effects due to dihedral and trihedral structures 15
Figure 1.19 Scattering from the convoluted cavity..... 15
Figure 1.20 Representative ray-tracing process as shown in [9] 17
Figure 2.1. Ray front with starting points (on the left) and launched rays (on the right)..... 22
Figure 2.2 Normal of a triangle..... 23
Figure 2.3 Parametric ray representation 24
Figure 2.4. Barycentric coordinates representation of a point inside a triangle..... 25

Figure 2.5. Translation and transformation applied in Möller - Trumbore algorithm 27
Figure 2.6. Reflection from a triangle 29
Figure 2.7. Reflection plane with the incident and reflected rays' components 30
Figure 2.8 Transmission line analogy for the planar reflection coefficient 32
Figure 2.9 Reflection Coefficient Comparison for HH Polarization 34
Figure 2.10 Reflection Coefficient Comparison for VV Polarization 35
Figure 2.11 Reflection on HH Polarization 36
Figure 2.12 Reflection at VV Polarization 37
Figure 2.13 Direction of Electric Field for Oblique Reflections 37
Figure 2.14 Reflected Field in terms of Incident Field 38
Figure 3.1 Surface normal representation on FEKO 42
Figure 3.2 Azimuth and Elevation definitions used in ray-tracing tool 43
Figure 3.3 Code of the comparison functions 45
Figure 3.4 The recursive algorithm used in the ray-tracing tool 46
Figure 3.5 Inputs Tab of ray tracing tool's GUI 48
Figure 3.6 Mesh inputs 48
Figure 3.7 Angular inputs 49
Figure 3.8 Inputs related to the analysis' conditions 49
Figure 3.9 Outputs Tab of ray tracing tool's GUI 50
Figure 3.10 Plotting the mesh 51
Figure 3.11 2D Angular Distribution 51
Figure 3.12 Critical Rays 52
Figure 3.13 Hit Map 52
Figure 3.14 3D Angular Distribution 53
Figure 3.15 Horizontal and vertical polarized electric field vectors and propagation vector 54
Figure 4.1 Coarse (top), standard (middle) and fine (bottom) meshes 58
Figure 4.2 2D and 3D angular distributions for coarse mesh case 59
Figure 4.3 2D and 3D angular distributions for standard mesh case 59

Figure 4.4 2D and 3D angular distributions for fine mesh case 59
Figure 4.5 2D angular distribution comparison for different mesh cases..... 60
Figure 4.6 2D and 3D angular distributions for sparse ray density case 61
Figure 4.7 2D and 3D angular distributions for default ray density case 61
Figure 4.8 2D and 3D angular distributions for dense ray density case 62
Figure 4.9 Normalized 2D angular distributions for different ray density cases.... 62
Figure 4.10 2D angular distributions for maximum bounce numbers: (a) 30, (b) 25, (c) 20, (d) 15, (e) 10, and (f) 5 63
Figure 4.11 Normalized 2D angular distributions for maximum bounce numbers 64
Figure 4.12 3D angular distributions for maximum bounce limits 30 (top) and 15 (bottom)..... 65
Figure 4.13 Square Plate 66
Figure 4.14 Angular scan on square plate..... 67
Figure 4.15 RCS of a metallic square plate for HH polarization..... 67
Figure 4.16 RCS of a metallic square plate for HH polarization (zoomed in) 68
Figure 4.17 RCS of a metallic square plate for VV polarization..... 69
Figure 4.18 RCS of a metallic square plate for VV polarization (zoomed in) 69
Figure 4.19 RCS of a coated square plate for HH polarization 70
Figure 4.20 RCS of a coated square plate for HH polarization (zoomed in)..... 70
Figure 4.21 RCS of a coated square plate for VV polarization 71
Figure 4.22 RCS of a coated square plate for VV polarization (zoomed in)..... 72
Figure 4.23 Dihedral Corner Reflector 73
Figure 4.24 Angular scan on dihedral corner reflector 74
Figure 4.25 RCS of a metallic dihedral corner reflector for HH polarization 74
Figure 4.26 RCS of a metallic dihedral corner reflector for HH polarization (zoomed in) 75
Figure 4.27 RCS of a metallic dihedral corner reflector for VV polarization 76
Figure 4.28 RCS of a metallic dihedral corner reflector for VV polarization (zoomed in) 77
Figure 4.29 RCS of a coated dihedral corner reflector for HH polarization..... 78

Figure 4.30 RCS of a coated dihedral corner reflector for HH polarization (zoomed in)..... 79
Figure 4.31 RCS of a coated dihedral corner reflector for VV polarization 79
Figure 4.32 RCS of a coated dihedral corner reflector for VV polarization (zoomed in)..... 80
Figure 5.1 Engine Interface with details of blades 84
Figure 5.2 Representative planar circular plate 84
Figure 5.3 Angular intervals on azimuth (left) and elevation (right) 85
Figure 5.4 The representation of the LHS duct on an aircraft model (in red borders) 85
Figure 5.5 Mesh of Model_01 86
Figure 5.6 CAD model of Model_01 from the top (left) and right (right) views..... 86
Figure 5.7 2D angular distribution of the rays on Model_01 87
Figure 5.8 3D angular distribution of rays on Model_01 87
Figure 5.9 RCS graphs of Model_01 for VV (left) and HH (right) polarizations... 88
Figure 5.10 RCS comparison of insect, bird, and air platforms 89
Figure 5.11 Top (left) and right side (right) views of Model_02 90
Figure 5.12 Shadowed rear face of Model_02 at the head-on angle (0° azimuth and 90° elevation)..... 90
Figure 5.13 Rear face of Model_02 is seen at 10° azimuth and 85° elevation..... 90
Figure 5.14 2D angular distribution of rays on Model_02 91
Figure 5.15 3D angular distribution of rays on Model_02 92
Figure 5.16 RCS graphs of Model_02 for VV (left) and HH (right) polarizations. 92
Figure 5.17 FEKO Planar multilayer substrate construction..... 93
Figure 5.18 FEKO dielectric medium creation 94
Figure 5.19 FEKO Reflection coefficient goal..... 95
Figure 5.20 FEKO Optimization parameters..... 95
Figure 5.21 FEKO Optimization for Model_02 96
Figure 5.22 FEKO Optimization with higher resolution of optimization angles 96
Figure 5.23 Change of "t_layer1" parameter during optimization 97

Figure 5.24 Material optimized for 0° incidence (2.05 mm UD-11738) 97
Figure 5.25 Material optimized for 15° incidence (1.9 mm UD-14502) 98
Figure 5.26 Material optimized for 65° incidence (1.52 mm FD-12331) 98
Figure 5.27 Material application for Model_02_RAM (left) and Model_02_optRAM (right) 99
Figure 5.28 RCS graph of Model_01_RAM for VV (left) and HH (right) polarizations 99
Figure 5.29 RCS graph of Model_01_optRAM for VV (left) and HH (right) polarizations 100
Figure 5.30 RCS graph of Model_02_RAM for VV (left) and HH (right) polarizations 101
Figure 5.31 RCS graph of Model_02_optRAM for VV (left) and HH (right) polarizations 101
Figure 5.32 Top (left) and right side (right) views of Model_03 102
Figure 5.33 Mode_03 from x-direction (left) and 80° elevation 15° azimuth (right) 102
Figure 5.34 RCS graphs of Model_03 for VV (left) and HH (right) polarizations 103
Figure 5.35 2D angular distribution of rays on Model_03 103
Figure 5.36 3D angular distribution of rays on Model_03 104
Figure 5.37 RCS graph of Model_03_RAM for VV (left) and HH (right) polarizations 104
Figure 5.38 RCS graph of Model_03_optRAM for VV (left) and HH (right) polarizations 105
Figure 5.39 Top (left) and right side (right) views of Model_04 106
Figure 5.40 Top (left) and right side (right) views of Model_05 107
Figure 5.41 2D angular distribution of rays on Model_04 108
Figure 5.42 2D angular distribution of rays on Model_05 108
Figure 5.43 3D angular distribution (top) and material application zones (bottom) for Model_04 109

Figure 5.44 3D angular distribution (top) and material application zones (bottom) for Model_05 110
Figure 5.45 RCS graph of Model_04 (top), Model_04_RAM (middle), and Model_04_optRAM (bottom) for VV (left) and HH (right) polarizations..... 111
Figure 5.46 RCS graph of Model_05 (top), Model_05_RAM (middle), and Model_05_optRAM (bottom) for VV (left) and HH (right) polarizations..... 113
Figure 5.47 Top (left) and right side (right) views of Model_06 115
Figure 5.48 Top (left) and right side (right) views of Model_07 115
Figure 5.49 Top (left) and right side (right) views of Model_08 116
Figure 5.50 2D angular distribution of rays on Model_06 117
Figure 5.51 2D angular distribution of rays on Model_07 117
Figure 5.52 2D angular distribution of rays on Model_08 118
Figure 5.53 3D angular distribution of rays on Model_06 118
Figure 5.54 3D angular distribution of rays on Model_07 118
Figure 5.55 3D angular distribution of rays on Model_08 119
Figure 5.56 Shortest ray path with two reflections for Model_07 119
Figure 5.57 The material application zones for Model_06 120
Figure 5.58 The material application zones for Model_07 120
Figure 5.59 The material application zones for Model_08 121
Figure 5.60 RCS graph of Model_06 (top), Model_06_RAM (middle), and Model_06_optRAM (bottom) for VV (left) and HH (right) polarizations..... 122
Figure 5.61 RCS graph of Model_07 (top), Model_07_RAM (middle), and Model_07_optRAM (bottom) for VV (left) and HH (right) polarizations..... 123
Figure 5.62 RCS graph of Model_08 (top), Model_08_RAM (middle), and Model_08_optRAM (bottom) for VV (left) and HH (right) polarizations..... 124
Figure 5.63 The second iteration of material application zones for Model_08..... 126
Figure 5.64 RCS graph of the second iteration of Model_08_optRAM for VV (left) and HH (right) polarizations..... 127
Figure 5.65 2D RCS graphs of VH (left) and HV (right) cross polarizations for Model_8 cases (top to bottom: PEC, RAM, opt_RAM, _v2_opt_RAM,)..... 129

Figure 6.1 Octree structure for two levels 135
Figure 6.2 2D ISAR image example of an aircraft 136
Figure 6.3 EM properties of UD-11738 139
Figure 6.4 EM properties of UD-14502 139
Figure 6.5 EM properties of DD-10322 140
Figure 6.6 EM properties of FD-12331 140

LIST OF ABBREVIATIONS

ABBREVIATIONS

2D: Two-Dimensional

3D: Three-Dimensional

A-A: Air-to-Air

A-S: Air-to-Surface

ANSYS: Analysis System

CAD: Computer-Aided Design

CATIA: Computer-Aided Three-Dimensional Interactive Application by Dassault Systèmes

CEM: Computational Electromagnetics

CFRP: Carbon Fiber-Reinforced Polymers

cm: Centimeter

CPU: Central Processing Unit

dB: Decibel

dBsm: Decibel square meter

DE: Differential Equation

ed. : Edition

EM: Electromagnetics

FD: Frequency Domain

FDFD: Finite Difference Frequency Domain

FDTD: Finite Difference Time Domain

FEKO: Feldberechnung für körper mit beliebiger oberfläche (field calculations involving bodies of arbitrary shape) by Altair Engineering, Inc.

GHz: Gigahertz

GO: Geometric Optics

GPU: Graphical Processing Unit

GTD: Geometric Theory of Diffraction

GUI: Graphical User Interface

HFSS: High Frequency Structure Simulator by ANSYS, Inc.

HH: Horizontal Transmit and Horizontal Receive

IE: Integral Equation

IEEE: Institute of Electrical and Electronics Engineering

IR: Infrared

LE: Leading Edge

LHS: Left Hand Side

MATLAB: Matrix Laboratory by The MathWorks, Inc.

mm: Millimeter

MoM: Method of Moments

no. : Number

PEC: Perfect Electric Conductor

PO: Physical Optics

PTD: Physical Theory of Diffraction

pp. : Pages

Radar: Radio Detection and Ranging

RAM: Radar Absorbing material

RCS: Radar Cross Section

RF: Radio Frequency

RL-GO: Ray Launching – Geometric Optics

SBR: Shooting and Bouncing Rays

TD: Time Domain

TE: Transverse Electric

TM: Transverse Magnetic

TWTD: Thin-Wire Time Domain

vol. : Volume

VV: Vertical Transmit and Vertical Receive

LIST OF SYMBOLS

SYMBOLS

$\vec{D}$: Electric Flux Density

$\vec{B}$: Magnetic Flux Density

$\vec{E}$: Electric Field Intensity

$\vec{H}$: Magnetic Field Intensity

$\vec{J}$: Electric Current Density

ρ : Electric Charge Density

$\nabla \times$: Curl Operator

$\nabla \cdot$: Divergence Operator

∞ : Infinity

σ : Radar Cross Section

λ : Wavelength

ε : Permittivity

μ : Permeability

Γ : Reflection coefficient

CHAPTER 1

INTRODUCTION

1.1 Purpose of the Study

"First kill" is an important term in the military. The critical point of "killing first" is "detecting first" before being detected by the enemy. Especially in the air combats, where the targets have high speeds such as compatible with the speed of the sound, the importance of "being stealth" (low observability) is critical since even milliseconds are crucial during the detection phase. Stealth technology for aircraft has become inevitable for the latest fifth-generation aircraft.

A stealth aircraft has clean zones with low Radar Cross Section (RCS) levels and sacrificial zones with high RCS levels, as shown in Figure 1.1. It is not physically possible to have a stealth aircraft with no high RCS regions.

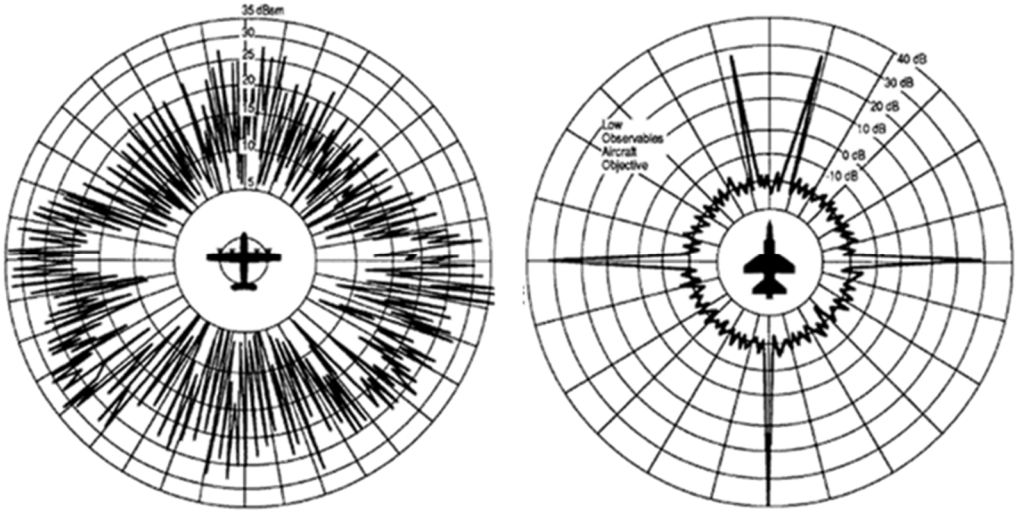

Figure 1.1 RCS signature patterns for conventional (left) and low observable (right) aircraft

Two of the most critical tactical zones are the forward and rear zones for attack (ingress) and return (regress), respectively. For both the forward and rear zones, the most critical RCS contributors are the cavities of the engines. In the forward zone, intake and duct; in the rear zone, the jet pipe of the exhaust are the most critical scatterers. The study aims to reduce the RCS level of cylindrical cavities using the statistical outputs of ray-tracing analyses. RCS levels are calculated by the code based on Shooting and Bouncing Rays (SBR) method. However, calculating RCS levels is not the primary purpose of this study. The primary purpose could be defined as diagnosing the high RCS values with the help of the ray-tracing analyses of the cavities and reducing the RCS levels by optimizing the geometry and the absorbing material.

In this Introduction chapter, basic information about electromagnetism, the definition of RCS, the concept of low observability or stealth, the methods to reduce the RCS and compute the RCS, the scattering mechanisms, and the main RCS contributors for an aircraft are mentioned in the following sections. Then, a brief introduction to one of the most important contributors, cavities on the aircraft, is given. Finally, the ray-tracing method used in this study is explained with the study's hypotheses.

1.2 Electromagnetic Wave Theory

Electromagnetism is the relationship between electricity and magnetism, and this relationship is ruled by Maxwell's Equations [1], given in Equation (1) to Equation (4). Maxwell's equations say that changing magnetic fields yield electric fields, and currents and changing electric fields create magnetic fields. The first part of this sentence is found by Faraday as the law of induction, given in Equation (3). And the second part is known as Ampère's Law with the correction of Maxwell, given in Equation (4).

$$\nabla \cdot \vec{D} = \rho \tag{1}$$

$$\nabla \cdot \vec{B} = 0 \tag{2}$$

$$\nabla \times \vec{E} = -\frac{\partial \vec{B}}{\partial t} \tag{3}$$

$$\nabla \times \vec{H} = \vec{J} + \frac{\partial \vec{D}}{\partial t} \tag{4}$$

As is understood from the name of the equations, Maxwell is not the first person who discovered the relationship between electricity and magnetism. For the first time in history, Hans Christian Ørsted linked electricity and magnetism in 1820. He observed that the needle of a compass moves when it is brought next to a current-carrying wire. In the same year, André-Marie Ampère demonstrated that two parallel current-carrying wires attract or repulse each other depending on the currents' directions. In 1831, Michael Faraday performed a critical experiment with magnets. In the experiment, a magnet moves through a loop of wire. This movement generates current on the wire.

In the same year, 1831, James Clerk Maxwell was born. He would gather these relations between electricity and magnetism and systematize them. He firstly introduced the displacement current as a correction to Ampère's Law. In the following years, the 1860s and 1870s, Maxwell has shown the relations with 20 equations. After he died, Oliver Heaviside reduced the number of equations from 20 to four, and "Maxwell's equations" have taken the form of up-to-date, given in Equation (1) to Equation (4) in 1879 [2].

The foundations and the history of the classical theory of electromagnetism have been mentioned above briefly. The theory is used in practices for different areas such as health, transportation, aviation, telecommunication, military, etc. One of the most critical application areas is the calculation of scattered electromagnetic (EM) fields from objects. Since, especially, detecting and calculating scattered EM fields from

the enemy targets have gained high importance since World War II, radar systems were developed during and after World War II.

Radar is the abbreviation of **RA**dio **D**etection **A**nd **R**anging [3]. Radar systems detect the objects and determine the range, speed, direction, and altitude of the objects by using radio waves. The process of the detection and determination of the range is based on Maxwell's Equations. The radar system's transmitter antenna transmits radio waves. The transmitted radio waves are reflected from the objects on their paths. The radar system's receiver antenna receives the reflected radio waves. The mentioned process (transmitting, reflecting, and receiving of the EM waves) is in a frame ruled by Maxwell's Equations. Radar is called monostatic if the transmitter and the receiver are located at the same point. In the bistatic radar case, the transmitter and the receiver are located at different points as in Figure 1.2. In this study, all analyses are performed according to the monostatic radar structure.

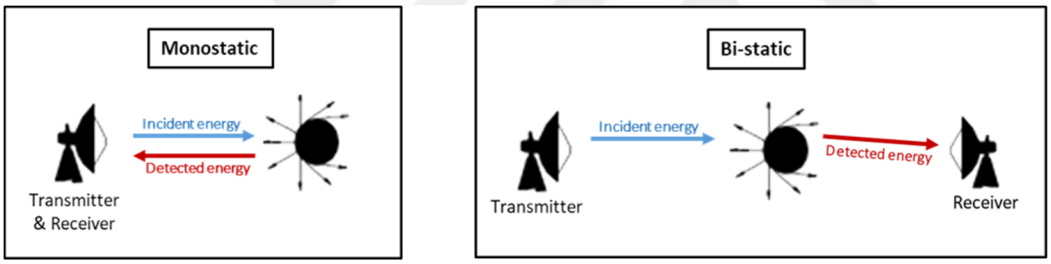

Figure 1.2 Monostatic (left) and bistatic (right) radar configurations

1.3 Definition of RCS

The relation between the transmitted and the reflected waves depends on several factors such as the EM characteristics of the media, range of the object, gain and losses of antennas, etc. The only parameter related to the object itself (besides the range or velocity of the object) is called the *Radar Cross Section* (RCS) of the object. RCS is a hypothetical area of the object, and it determines the amount of energy scattered from the object itself. For the simplified radar range equation, the power density radiated from the omnidirectional transmitter antenna (at distance R) is given by the formula in Equation (5):

$$\frac{P_{peak}}{4\pi R^2} \tag{5}$$

where P_{peak} is the peak power radiated from the antenna. For a directional antenna, the power density becomes:

$$\frac{P_{peak}G}{4\pi R^2} \tag{6}$$

where G is the gain of the antenna. The reflected power from the object is calculated by using the RCS of the target:

$$\frac{P_{peak}G\sigma}{4\pi R^2} \tag{7}$$

where σ is the RCS of the target. The power density at the receiver antenna of a monostatic radar system (where the transmitter and the receiver antennas are at the exact location) is defined as in Equation (8):

$$\frac{P_{peak}G\sigma}{(4\pi R^2)^2} \tag{8}$$

The received power is proportional to the effective aperture A_e of the receiver antenna. Finally, the received power P_r is found by using Equation (9):

$$P_r = \frac{P_{peak}G\sigma A_e}{(4\pi R^2)^2} \tag{9}$$

As seen from the above equations, the only parameter, besides the range, related to the object is the RCS of the object. The only way to increase an object's detection range is to reduce the RCS of the object. The objects (such as ships, marines, or aircraft) are called low observable or stealth if radar systems are challenging to detect them.

1.4 Stealth or Low Observability

Stealth or low observability technology has become one of the most important and popular topics in the military since the last quarter of the 20th century. In the war scenarios, there is a chain of rules of thumb: Who detects first has more chance for the first shoot. Who shoots first has more chance for the first kill. Who kills first has more chance for victory. Low observability is inevitable for the 5th generation aircraft. The following example could describe the importance of stealth technology. In comparing conventional and stealth aircraft, it isn't easy to find a route to destroy the target for a conventional aircraft. In contrast, for a stealth aircraft, it is possible to find routes for incoming and outgoing. In the following figures (Figure 1.3 and Figure 1.4), a basic illustration of this comparison is given. Orange circles represent the range that radar systems could detect enemy aircraft. These circles are larger for conventional enemy aircraft, whereas they are smaller for stealth enemy aircraft. For the latter case, it is much more possible to find a route for stealth aircraft, as shown in the dashed red line in Figure 1.4.

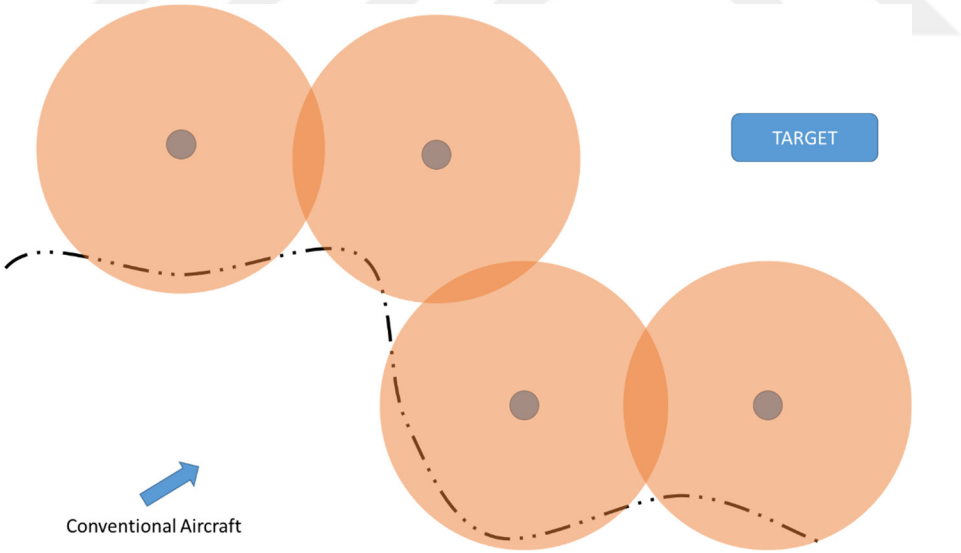

Figure 1.3. War scenario for a conventional aircraft

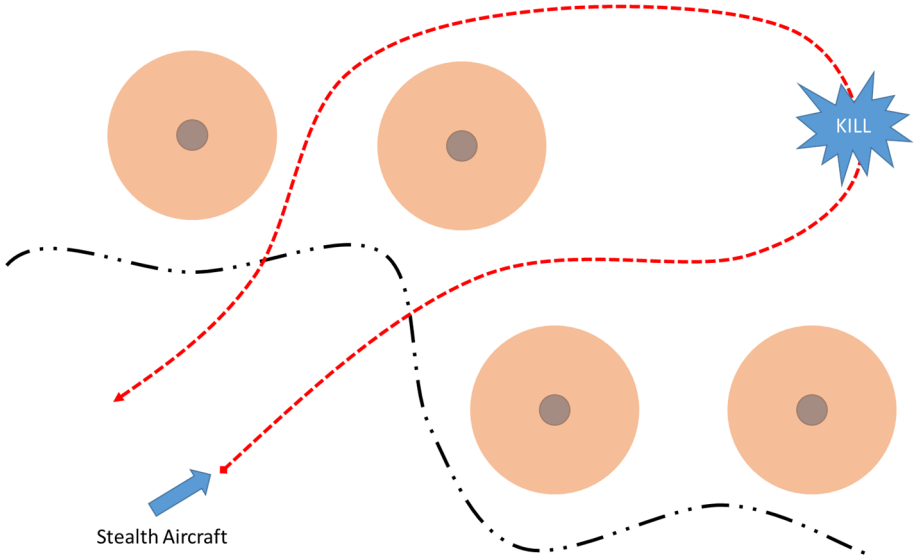

Figure 1.4. War scenario for a stealth aircraft

1.5 RCS Reduction Techniques: Geometry and Materials

Stealth platforms could be designed by applying RCS reduction techniques. The way to reduce RCS starts with understanding the concept and physics of RCS. RCS of an object physically depends on the EM characteristics and the geometry of the object. The design of an object with low RCS, which is difficult to detect by radar (stealth for radars), starts with geometry optimization. In the second phase, the geometry is coated with absorber materials which absorb the energy of the incoming EM waves [3][4]. For specific cases, conductive materials are used for the coating to prevent discontinuities as on the canopy. Canopy surfaces are coated with conductive thin films to be sure that the EM waves are not interacting with the cockpit elements and do not backscatter strongly from the cockpit cavity. The conductive thin film coating, which likely contains gold, used on the F-22 Raptor is shown in Figure 1.5.



Figure 1.5 Conductive coating on F-22 Raptor canopy

In some cases, using conductive coatings instead of absorbing coatings is more practical in terms of low RCS. For instance, the gap between Carbon Fiber-Reinforced Polymers (CFRP) panels can be filled with conductive sealant in order to maintain the electrical conductivity as in F-35 Lightning II (in Figure 1.6). In such a case, the diffraction effect due to the interface between CFRP panels and the absorbing material is eliminated.

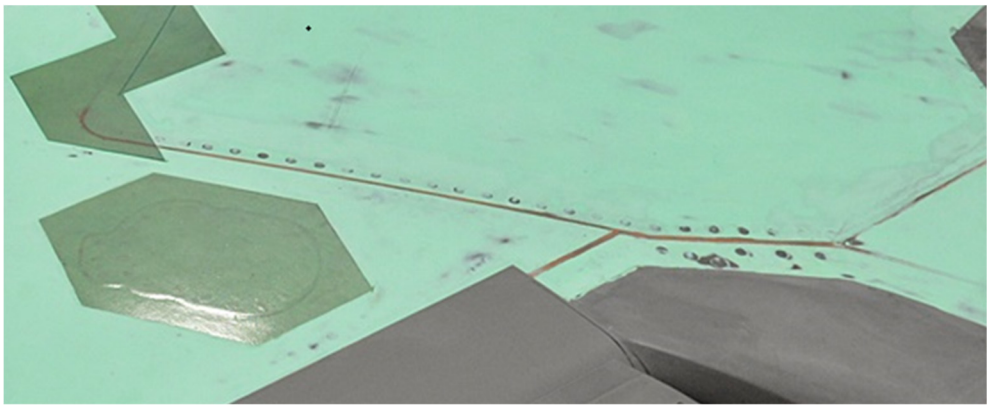

Figure 1.6 Copper filled conductive sealant application between the CFRP panels

Fifth-generation stealth fighters have basic stealth design approaches on their outer geometry. For example, internal weapon bays could be seen as inevitable for stealth aircraft. High scatterings from the cylindrical body, tip diffractions of weapons, and the interactions between weapons and wings or fuselage are eliminated using internal weapon bays. The other example is one of the most important design patterns for fifth-generation stealth aircraft: Angular alignment. All the possible edges, mainly leading edges (LE) and trailing edges, and discontinuities are aligned to the same angles on the top and bottom view or side view, including the chevrons. For the ideal case, only one angle was chosen as the sacrificial angle. However, it is not possible to align all the edges and discontinuities to one angle along with high aerodynamic performance. The sacrificial angles are determined, and all the edges, discontinuities, access panels, etc., are designed according to the determined angles, as illustrated in Figure 1.7. The angular alignment applications are observed on the 5th generation aircraft such as the F-22 Raptor. In the following figures, Figure 1.8 and Figure 1.9, the angular alignment from front and side views are shown.

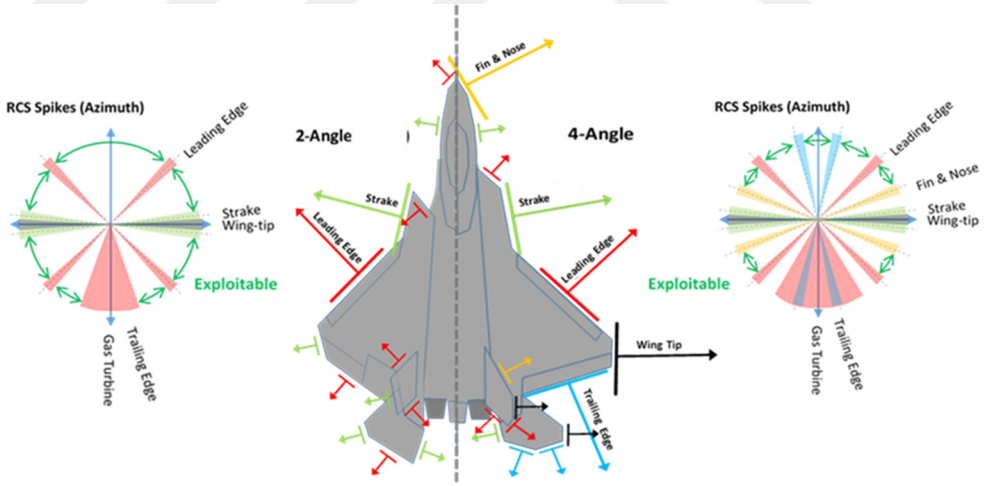

Figure 1.7 Angular alignment representations



Figure 1.8 Angular alignment on F-22 Raptor aircraft from front view



Figure 1.9 Angular alignment on representative geometry of F-22 Raptor aircraft from the side view

In the second phase, absorbing materials (in Figure 1.10) are applied to the scattering centers of the aircraft. Doors and access panels, edges and tips, control surface interfaces, inlets, exhausts, and cavities are coated with absorbing materials of different types (a general application shown in Figure 1.11, including LE aligned chevron cut of the RAM on the trailing edges). The type of the absorbing material and the optimization angle and frequency bands are also objected to change for various scattering centers. The panels and doors are coated with replaceable elastomeric absorbers. In parallel, for cavities, for instance, absorbing paint could reduce the energy of the scattered field. In the specific areas, materials with optimum

performance at specular reflection are preferred. On the other hand, in another particular region, surface wave absorbing materials could be used for the best absorption performance. The optimum decision could be made if the scattering characteristics of the corresponding regions are known.

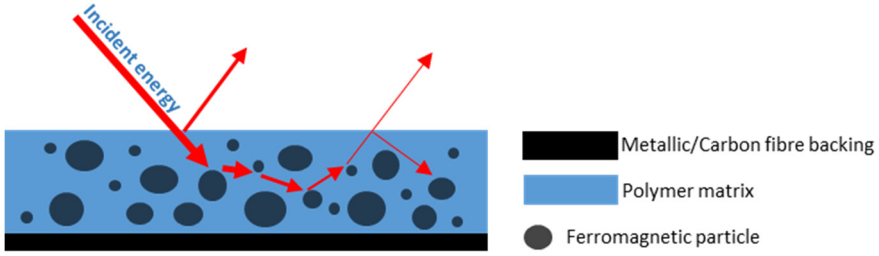

Figure 1.10 Absorption mechanism for RAMs



Figure 1.11 RAM application on J-20 aircraft

Before starting the stealth design, it is obligatory to see the aircraft's RCS level and characteristics. As a result, the calculation of the RCS of objects is one of the most critical points of the stealth (low observable) design.

1.6 RCS Computation: Analytical and Numerical Methods

The unit of RCS is square-meter. However, it is not a physical area; as mentioned above, it is a hypothetical area. RCS of an object could be defined as the ratio of the

square of the signal amplitude reflected from the object to the square of the signal amplitude reflected from a sphere with a 1 m^2 cross-sectional area. In IEEE, RCS is defined as "scattered cross-section" as follows:

> "The projected area required to intercept and isotropically radiate the same power that a scatterer (target) scatters toward the receiver [5]."

The formulation of the RCS, σ, is given as in Equation (10):

$$\sigma_{pq} = \lim_{R\to\infty}\left[4\pi R^2 \frac{\langle|\vec{E}^s{}_p|^2\rangle}{\langle|\vec{E}^i{}_q|^2\rangle}\right] \tag{10}$$

where R is the distance between the source and the target, $\vec{E}^s{}_p$ is the p-polarized component of the field scattered from the receiver and $\vec{E}^i{}_q$ is the q-polarized incident field at the target. In this representation, $\vec{E}^i$ is assumed as planar over the target. As mentioned previously, all analyses are performed under the monostatic placement of the antennas. The RCS is referred to the monostatic RCS in this study.

In the world of engineering, problems that are solvable analytically are generally fundamental and straightforward problems. The other problems that consist of complex geometries and complex computational domains (such as permittivity and permeability of the media) could be solved using numerical solution techniques. Computational Electromagnetics (CEM) is the field that deals with the solution techniques to electromagnetic problems.

CEM solution techniques are classified in terms of the target size. For the targets that have a comparable size with the wavelength of interest, low-frequency methods are used. For the case of large objects, high-frequency methods are appropriate [6].

Low-frequency methods, also known as numerical methods, are classified as Integral Equation (IE) and Differential Equation (DE) methods or Time Domain (TD) and Frequency Domain (FD) methods. Method of Moments (MoM) is an instance of the Frequency Domain Integral Equation method. As an example of the Time Domain

Differential Equation method, the Finite Difference Time Domain (FDTD) method could be given [7].

High-frequency methods can be examined in two sub-group: field-based and current-based methods. Geometric Optics (GO) and Geometric Theory of Diffraction (GTD) methods are field-based methods, whereas Physical Optics (PO) and Physical Theory of Diffraction (PTD) methods are current-based methods [8].

All these methods, both low and high-frequency methods, could be suitable for specific implementations. At that point, the scattering mechanism is usually the most critical factor in choosing the most appropriate solution method.

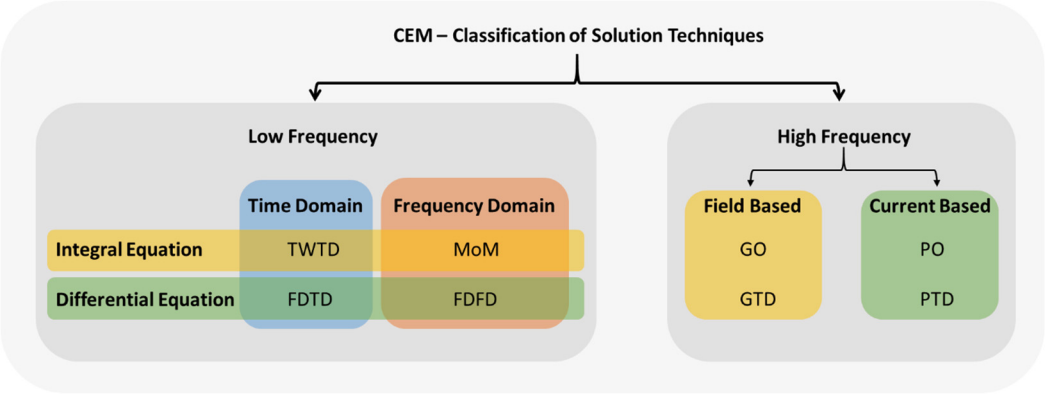

Figure 1.12. Classification of CEM solution methods

1.7 RCS Scattering Mechanisms – Cavities

Aircraft are complex geometries with wings, tails, canopy, inlets, exhausts, cavities, doors, external weapons, antennas, etc. All of these components have different scattering mechanisms, as shown in the following figures from Figure 1.13 to Figure 1.19. For example, at the discontinuities, diffraction is the primary source of the scattering, and surface wave absorbing materials are used to reduce the diffraction effect with an optimized design.

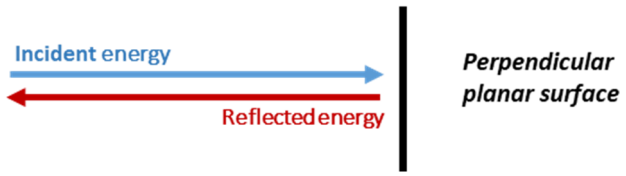

Figure 1.13 Normal reflection from a planar surface

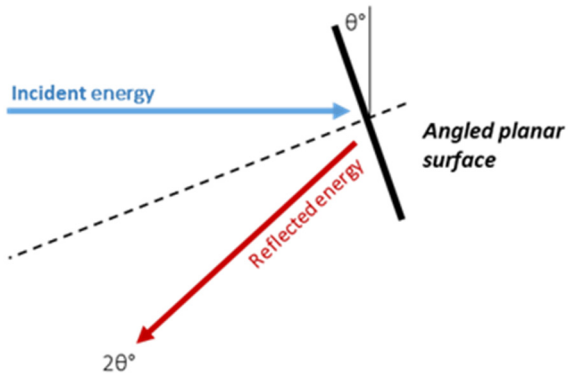

Figure 1.14 Specular reflection from a tilted surface

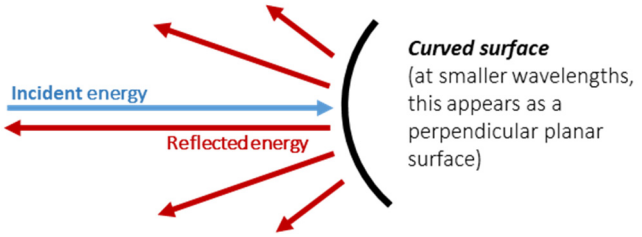

Figure 1.15 Reflection from a curved surface

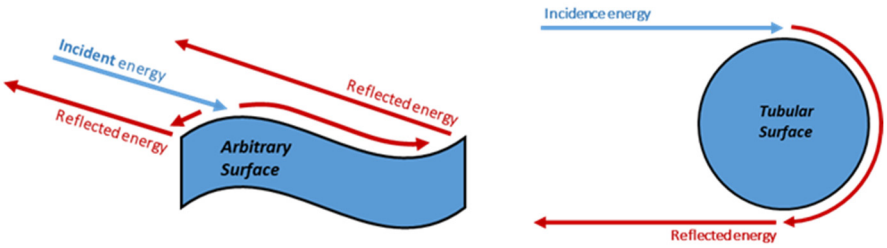

Figure 1.16 Surface traveling and creeping waves

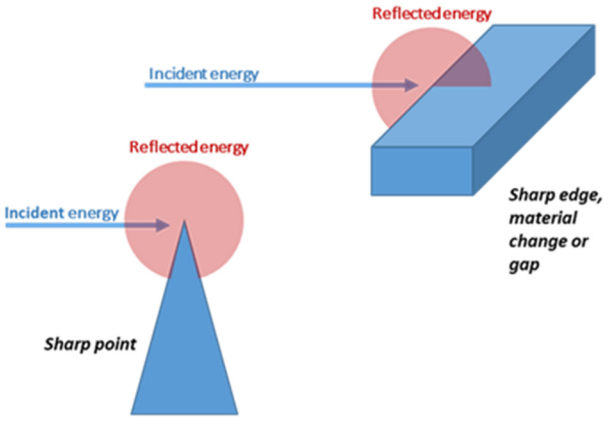

Figure 1.17 Diffraction from edges and tip points

The cavities have the most critical and unpredictable scattering mechanism for a stealth platform. The stealth design and absorbing material optimization processes eliminate the high RCS effect due to cavities. During the design process, RCS simulations/analyses are used to determine the RCS contribution of the cavities. Due to the cavities' geometry, the RCS analyses' convergence could be a problem for full-wave solvers. At that point, asymptotic methods become useful options. The Shooting and Bouncing Rays (SBR) [9] method is used to simulate the RCS of the objects with cavity structures. In the SBR method, the EM waves are modeled as rays. Rays are shot from given aspects of the object and bounce from the surfaces of the object, as in Figure 1.19. This process is called "ray tracing".

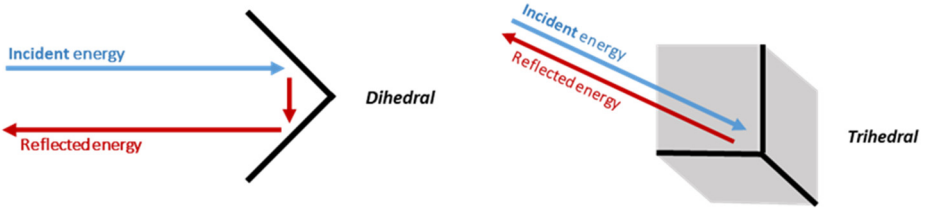

Figure 1.18 Cavity effects due to dihedral and trihedral structures

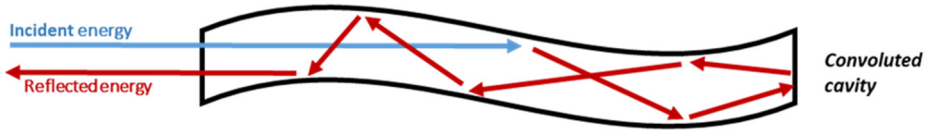

Figure 1.19 Scattering from the convoluted cavity

1.8 Ray-Tracing and SBR Method

In the case of high frequency, or in other words, in the case of large objects, where the wavelength of the interest is much smaller than the object's size, the motion of the electromagnetic waves could be represented by straight rays. The movement of the rays obeys the optical rules in this representation. Reflection and refraction mechanisms are also similar to the optical cases. For instance, reflections are modeled according to Snell's Law, where the reflection angle is equal to the incident angle.

For large cavities, the ray-tracing-based method, SBR, is used to calculate RCS. There are three major parts of the SBR method [9]:

1. *Ray-tracing* to determine the ray paths

2. *Determining the field amplitude* based on Geometrical Optics (GO) approximations

3. *Determining the backscattering field and RCS* by using Physical Optics (PO) approximations

In the first part, parallel rays are shot from the given aspects to the cavity model. Then for each ray, intersection points are found. At the intersection point, reflected ray directions are calculated according to Snell's Law. Then the ray-tracing procedure continues for each ray until the ray exits from the cavity or reaches the maximum bounce number. This whole process is called the ray-tracing phase and is illustrated in Figure 1.20. This phase only depends on the geometry [9].

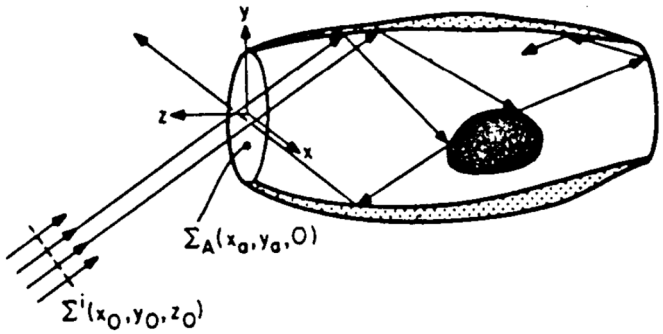

Figure 1.20 Representative ray-tracing process as shown in [9]

Field and RCS calculations are subjects of the other parts of the SBR method. Cavity surfaces could be Perfect Electric Conductor (PEC) or coated with radar absorbing material (RAM). The effect of absorbing material is also calculated in those steps. Some portion of the incident electromagnetic waves' energy is absorbed in each reflection according to the electromagnetic characteristics of the reflection surface and the incidence angle. Finally, the remaining energy of the returning electromagnetic waves determines the RCS of the object.

The high-frequency methods, also called asymptotic methods, such as PO and GO, use the illuminated surfaces of the models in the RCS calculation steps. They are useful methods for basic geometric shapes which have no cavities. For more complex geometries with cavities, these methods become inadequate. The effects of the shadowed surfaces inside the cavities are not taken into consideration in PO and GO methods. On the other hand, both illuminated and shadowed surfaces contribute to RCS in the SBR method. SBR calculates the multi-reflection effects in complex geometries. This point makes the SBR method more suitable than PO and GO for complex geometries that especially have cavities with multi-reflection effects. Even though SBR uses PO and GO approximations in the field calculation steps, it eliminates the drawbacks of these methods by taking into account the RCS contributions due to the shadowed faces of the targets.

1.9 Hypotheses Presented in the Study

In this study, an SBR tool is developed for field and RCS calculations. The ray-tracing part of the SBR tool is used to store the necessary information about the ray statistics. Ray statistics are used to design optimized geometry and optimized material for the related geometry. Two main hypotheses are investigated in this study:

1. Since some portion of the energy of the incident electromagnetic wave is absorbed in each reflection from a coated surface, an increase in "the minimum bounce number" results in a lower RCS level.

2. Since material characteristics affect absorption performance at different incident angles, properly selected material (optimized for the incident angle which is observed mostly) results in a lower RCS level.

For the former one, geometric changes are applied to increase the minimum bounce number. Critical ray paths with the lowest bounce numbers can be investigated in this geometric optimization process. For instance, if there is a direct interaction with a flat surface, obscuring that surface by modifying the geometry is one of the possible solutions to increase the reflection numbers.

For the latter part, the effect of different materials is shown with the help of commercial RCS simulation tools. By changing the thickness of the absorbing material, the optimized reflection angle can be updated. In this study, the material thicknesses are limited from 0.5 mm to 2 mm to have a bounded solution space.

The outline of the thesis is summarized as follows: First, literature knowledge about the ray-tracing method, including different ray–triangle intersection algorithms, and the details of field and RCS calculations of the SBR tool will be investigated in Chapter 2. Then, the developed algorithm and graphical user interface, GUI, of the ray-tracing tool will be shown in Chapter 3. In the next step, convergence tests for mesh and ray densities and maximum allowable bounce numbers will be undertaken

in Chapter 4. In the next chapter, Chapter 5, different parameters will be investigated for an optimized geometry. A bend will be placed on the straight cylindrical cavity to obscure the flat rear surface and to increase the minimum reflection number. The location and the slope of the bend are the main parameters that were investigated during the study. At that step, RCS analyses will be performed with PEC and coated cavity models. In the first phase, the coating material will be the same. Then for the second phase, the coating material will be optimized to the most seen reflection angle in ray statistics. The effects of these optimizations will be observed carefully from RCS graphs and RCS averages. In the final chapter, Chapter 6, the conclusion and the future works are presented. The comments about the RCS results for different models are shared in the conclusion part. If there are any unexpected results, the possible reasons will also be discussed. Possible contributions to the current work will be mentioned in the future work section.

CHAPTER 2

LITERATURE REVIEW: RAY TRACING PROCESSES, RAY-TRIANGLE INTERSECTION ALGORITHMS, AND FIELD AND RCS CALCULATIONS

Literature knowledge about the ray-tracing method, including all procedure steps, will be presented in the first sections of this part. The field and RCS calculation steps of the SBR method are investigated in the last sections of this part.

Ray tracing procedure consists of three steps:

- Launching rays from starting points $\vec{P}^0$ and the direction $\vec{D}^i$,

- Intersecting the incident rays with the triangular meshed model at the intersection point $\vec{P}^1$,

- Calculating the reflected rays' directions $\vec{D}^r$.

The second and third steps of this procedure are repeated recursively until the ray exits from the cavity or reaches to maximum reflection number limit, if it exists. All steps will be investigated in detail in the following parts.

2.1 Launching Rays

Rays could be defined as lines with a starting point and direction. A ray window, which consists of a high number of starting points (Figure 2.1– left side), is generated for each incidence aspect. From the ray window, parallel rays are launched (Figure 2.1– right side).

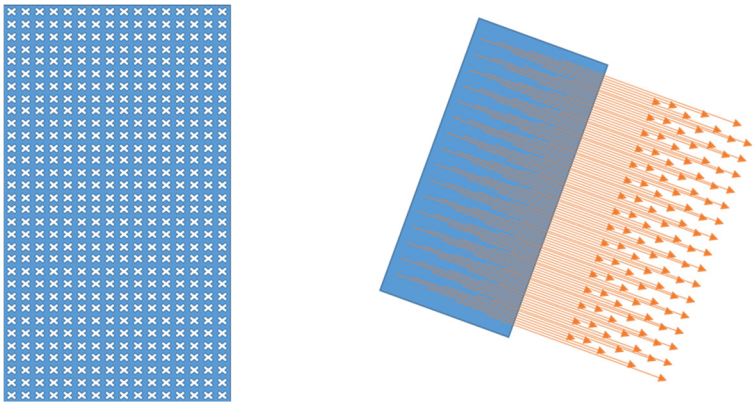

Figure 2.1. Ray front with starting points (on the left) and launched rays (on the right)

The parameters, starting point ($\vec{P}^0$) and direction ($\vec{D}^i$), are defined according to the location of the model in the space and angle of the incidence, relatively. The details used in the algorithm will be given in the following sections.

2.2 Finding the Intersection Points

In the next step, the intersection point of the ray and meshed model will be found. Let's define $\vec{P}^0$ as in Equation (11) and $\vec{D}^i$ as in Equation (12):

$$\vec{P}^0 = \left[{p^0}_x, {p^0}_y, {p^0}_z\right] \tag{11}$$

$$\vec{D}^i = \left[{d^i}_x, {d^i}_y, {d^i}_z\right] \tag{12}$$

Any point $\vec{P}^1$ on this line could be defined as in Equation (13) and Equation (14):

$$\vec{P}^1 = \vec{P}^0 + \vec{D}^i t \tag{13}$$

$$\left[{p^1}_x, {p^1}_y, {p^1}_z\right] = \left[{p^0}_x, {p^0}_y, {p^0}_z\right] + \left[{d^i}_x, {d^i}_y, {d^i}_z\right] t \tag{14}$$

where t is a positive quantity if $\vec{P}^1$ is in the direction of $\vec{D}^i$ from $\vec{P}^0$.

In the ray-tracing algorithm, the most crucial part is the ray–triangle intersection part since this part is called and executed at each recursion of the algorithm. The intersection of incidence ray and triangular mesh model requires the highest source in terms of computation power and time. It is essential to find the fastest and cheapest way to calculate the intersection point.

There are several ray–triangle intersection algorithms in the literature. In this study, two of them are investigated:

2.2.1 Badouel Algorithm

Deciding whether the ray intersects with the plane that contains the polygon (triangle in this case) is the first step of the Badouel algorithm [10]. A triangle is described by its vertices, $\vec{V_i}$ where $i = (0, 1, 2)$. The plane that contains the triangle is described by a normal vector and a point on that plane. The normal vector $\vec{N}$ is given by the cross product of edge vectors of the triangle as shown in Figure 2.2:

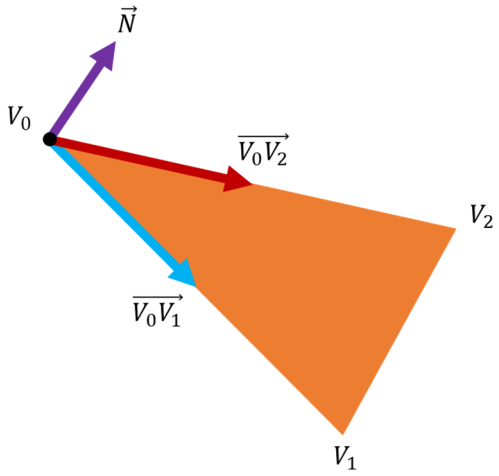

Figure 2.2 Normal of a triangle

$$\vec{N} = \overrightarrow{V_0V_1} \times \overrightarrow{V_0V_2} \tag{15}$$

For any point $\vec{P}$ on the plane, dot product $\vec{P} \cdot \vec{N}$ is constant, and it equals the dot product of $\overrightarrow{V_0} \cdot \vec{N}$ since $\overrightarrow{V_0}$ is a point on the plane. Let this constant value be equal to $-d$. Then Equation (16) is the description of the plane:

$$\overrightarrow{V_0} \cdot \vec{N} + d = 0 \tag{16}$$

For a parametric ray defined in Equation (17), the intersection point (let it be vertex $\overrightarrow{V_0}$ for this case) could be found for parameter t given in Equation (18):

$$\vec{r}(t) = \vec{O} + \vec{D}t \tag{17}$$

(where $\vec{O}$ is the origin of the parametric ray $\vec{r}(t)$ and $\vec{D}$ is the direction of the corresponding ray as in Figure 2.3)

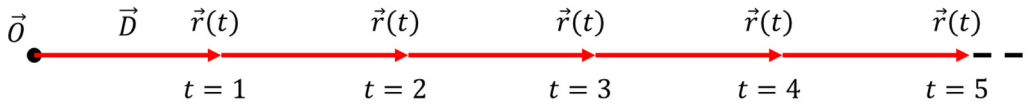

Figure 2.3 Parametric ray representation

$$t = -\frac{d + \vec{O} \cdot \vec{N}}{\vec{D} \cdot \vec{N}} \tag{18}$$

For the cases of:

parallel ray and triangle, where $\vec{D} \cdot \vec{N} = 0$,

intersection behind the origin of the ray, where $t \leq 0$,

already found a closer intersection, where $t > t_{min}$,

there is no valid intersection. For the intersection case, determining the intersection point is the second step.

Badouel algorithm uses the concept of "barycentric coordinates" for the second step. The term "*bary*" is a Greek word that means "*weight*" [11]. Barycentric coordinates could be understood with an example: Let E is any point inside the triangle ABC. And three masses (u, v, w) are placed at the corners of triangle ABC. These three

masses' center of gravity (barycenter) coincident with point E for specific values of u, v, and w. These u, v, and w values are the barycentric coordinates of point E. In the Badouel algorithm, normalized barycentric coordinates, where u+v+w = 1, are used.

Figure 2.4 shows the triangle ABC. For point E, inside triangle ABC, the vectorial equation given in Equation (19) is valid for the condition in Equation (20):

$$\overrightarrow{AE} = \alpha \cdot \overrightarrow{AC} + \beta \cdot \overrightarrow{AB} \tag{19}$$

$$\alpha \geq 0, \beta \geq 0, \alpha + \beta \leq 1 \tag{20}$$

If $\alpha + \beta = 1$, then point E is on the BC edge. Point E is on AB or AC edges for $\alpha = 0$ or $\beta = 0$, respectively. These α and β values are the barycentric coordinates of point E.

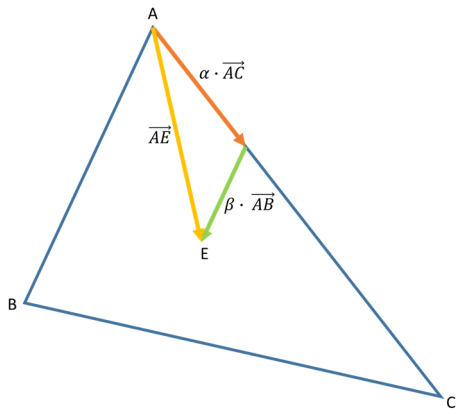

Figure 2.4. Barycentric coordinates representation of a point inside a triangle

To find the values of α and β, Equation (19) must be decomposed into x, y, and z components as in Equation (21):

$$\begin{aligned} E_x - A_x &= \alpha \cdot (C_x - A_x) + \beta \cdot (B_x - A_x) \\ E_y - A_y &= \alpha \cdot (C_y - A_y) + \beta \cdot (B_y - A_y) \\ E_z - A_z &= \alpha \cdot (C_z - A_z) + \beta \cdot (B_z - A_z) \end{aligned} \tag{21}$$

There exist a unique solution for α and β. The system is reduced to two dimensions to find this unique solution. Primary planes (xy, yz, xz) are used for reduction. The projections of the triangle onto these planes are calculated. The triangle could be perpendicular to one of these primary planes, which results in a single line for the projection onto that perpendicular plane. The dominant component of the normal vector is found, and the projection is taken onto the primary plane perpendicular to the dominant component to avoid the described problem. Define i_0 as x or y or z for $max(|N_x|, |N_y|, |N_z|)$ is $|N_x|$ or $|N_y|$ or $|N_z|$, respectively. Then i_1 and i_2 are indices different from i_0. At that point, for a vector at $i_1 i_2$ plane, two-dimensional coordinates of that vector could be defined as (u, v). $\overrightarrow{AE}$, $\overrightarrow{AC}$, and $\overrightarrow{AB}$ are projected onto that plane as in Equation (22):

$$\begin{aligned} u_0 &= E_{i_1} - A_{i_1} & u_1 &= C_{i_1} - A_{i_1} & u_2 &= B_{i_1} - A_{i_1} \\ v_0 &= E_{i_2} - A_{i_2} & v_1 &= C_{i_2} - A_{i_2} & v_2 &= B_{i_2} - A_{i_2} \end{aligned} \tag{22}$$

These equations reduce Equation (21) into Equation (23):

$$\begin{aligned} u_0 &= \alpha \cdot u_1 + \beta \cdot u_2 \\ v_0 &= \alpha \cdot v_1 + \beta \cdot v_2 \end{aligned} \tag{23}$$

Finally, the solutions for α and β are given in Equation (24):

$$\alpha = \frac{det\begin{pmatrix} u_0 & u_2 \\ v_0 & v_2 \end{pmatrix}}{det\begin{pmatrix} u_1 & u_2 \\ v_1 & v_2 \end{pmatrix}}, \qquad \beta = \frac{det\begin{pmatrix} u_1 & u_0 \\ v_1 & v_0 \end{pmatrix}}{det\begin{pmatrix} u_1 & u_2 \\ v_1 & v_2 \end{pmatrix}} \tag{24}$$

2.2.2 Möller – Trumbore Algorithm

In the Badouel algorithm, before finding the intersection point of ray and triangle, the intersection of ray and plane that contains the triangle is checked. However, in Möller – Trumbore algorithm [12], there is no need to check the intersection of ray and plane that includes the triangle. This situation yields a decrease in memory usage

since there is no need to store the plane's normal; only the triangle's vertices are stored.

The definition of the ray is the same as in Equation (17). The definition of point E in terms of barycentric coordinates could be given as in Equation (25):

$$\vec{E}(u,v) = (1-u-v)\vec{A} + v\vec{B} + u\vec{C} \tag{25}$$

where $u \geq 0, v \geq 0, u+v \leq 1$ for an interior point E as in the previous case. The intersection could be computed by solving $\vec{r}(t) = \vec{E}(u,v)$ as in Equation (26):

$$\vec{O} + \vec{D}t = (1-u-v)\vec{A} + v\vec{B} + u\vec{C} \tag{26}$$

Equation (26) is written in linear system form as in Equation (27):

$$[-\vec{D} \quad \vec{C}-\vec{A} \quad \vec{B}-\vec{A}]\begin{bmatrix} t \\ u \\ v \end{bmatrix} = \vec{O} - \vec{A} \tag{27}$$

The given system can be described as a process of translation and transformation geometrically. Firstly, the triangle and the ray are translated with $-A$, which results in a triangle translated to the origin. Then the transformation M (where transformation matrix given by $M = [-\vec{D} \quad \vec{C}-\vec{A} \quad \vec{B}-\vec{A}]$) is applied to the whole system to have a unit triangle with aligned edges to u and v axes as in Figure 2.5.

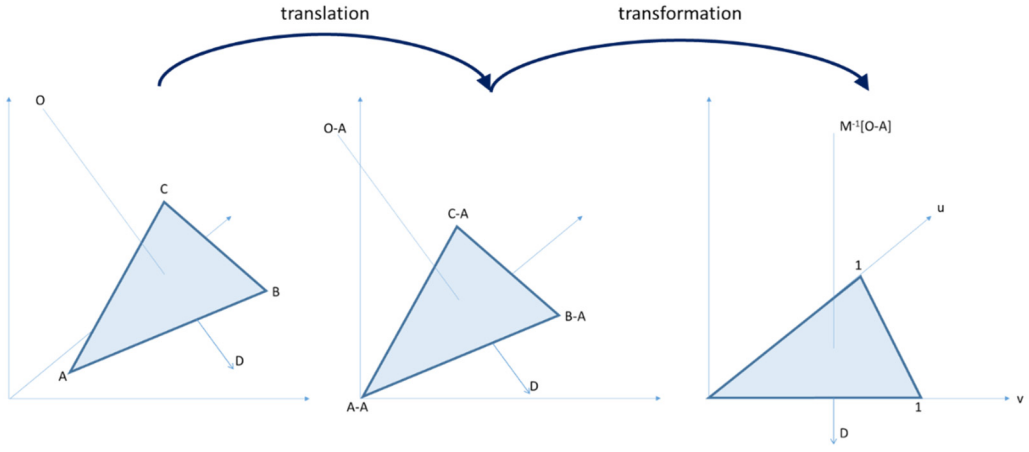

Figure 2.5. Translation and transformation applied in Möller - Trumbore algorithm

For the solution of the linear system given in Equation (27), let's define $\overrightarrow{E_1} = \vec{C} - \vec{A}$, $\overrightarrow{E_2} = \vec{B} - \vec{A}$ and $\vec{T} = \vec{O} - \vec{A}$. By applying Cramer's rule, the solution of Equation (27) is given as in Equation (28):

$$\begin{bmatrix} t \\ u \\ v \end{bmatrix} = \frac{1}{det\left(\left[-\vec{D} \quad \overrightarrow{E_1} \quad \overrightarrow{E_2}\right]\right)} \begin{bmatrix} det\left(\left[\vec{T} \quad \overrightarrow{E_1} \quad \overrightarrow{E_2}\right]\right) \\ det\left(\left[-\vec{D} \quad \vec{T} \quad \overrightarrow{E_2}\right]\right) \\ det\left(\left[-\vec{D} \quad \overrightarrow{E_1} \quad \vec{T}\right]\right) \end{bmatrix} \tag{28}$$

Since $det([\vec{A} \quad \vec{B} \quad \vec{C}]) = -(\vec{A} \times \vec{C}) \cdot \vec{B} = -(\vec{C} \times \vec{B}) \cdot \vec{A} = -(\vec{B} \times \vec{A}) \cdot \vec{C}$, Equation (28) could be rewritten as in Equation (29):

$$\begin{bmatrix} t \\ u \\ v \end{bmatrix} = \frac{1}{(\vec{D} \times \overrightarrow{E_2}) \cdot \overrightarrow{E_1}} \begin{bmatrix} (\vec{T} \times \overrightarrow{E_1}) \cdot \overrightarrow{E_2} \\ (\vec{D} \times \overrightarrow{E_2}) \cdot \vec{T} \\ (\vec{T} \times \overrightarrow{E_1}) \cdot \vec{D} \end{bmatrix} = \frac{1}{\vec{P} \cdot \overrightarrow{E_1}} \begin{bmatrix} \vec{Q} \cdot \overrightarrow{E_2} \\ \vec{P} \cdot \vec{T} \\ \vec{Q} \cdot \vec{D} \end{bmatrix} \tag{29}$$

where $\vec{P} = \vec{D} \times \overrightarrow{E_2}$ and $\vec{Q} = \vec{T} \times \overrightarrow{E_1}$.

During the implementation phase, firstly $\vec{P}$ is calculated to find the determinant value of the transformation matrix. If the determinant is zero, then there is no intersection between the ray and triangle. A negative determinant means that the ray hits the triangle from the back (opposite side according to the surface normal). In the next step, $\vec{T}$ is computed to find u. For the case that $0 \leq u \leq 1$, Q is calculated to find v. If $0 \leq v$ and $u + v \leq 1$, then t is calculated, finally. t value must be checked if there already exists a smaller t_{min} value. This latest control is done at the first step (ray–plane intersection step) of the Badouel algorithm.

Both Badouel and Möller – Trumbore algorithms are investigated. In the Badouel case, the ray is intersected with the plane that contains the triangle. As a second step, the intersection point is checked whether it is in the triangle or not with the help of the barycentric coordinates. However, in the Möller – Trumbore case, the ray is directly intersected with the triangle. In this study, due to less storage (memory) requirement and slightly faster implementation [12][13], Möller – Trumbore algorithm is preferred.

2.3 Determining the Reflected Rays

Rays are launched, and the intersection points with triangles are found. It is time to find the reflected ray. Then, a new tracing process will be handled with a new ray. The intersection point of the previous ray will be the starting point of the new ray, and the direction of the reflected ray will be the direction of the new ray. This procedure will continue until the ray exits from the cavity or the maximum reflection number limit is reached (if it exists).

The direction of the reflected ray could be found for the given incident ray direction and surface normal vector of the reflection surface with the help of Snell's Law. According to Snell's law, it is known that the incident vector, normal vector, and the reflected vector are coplanar. The other property of Snell's law is that the reflection angle θ^r is equal to incidence angle θ^i as in Figure 2.6.

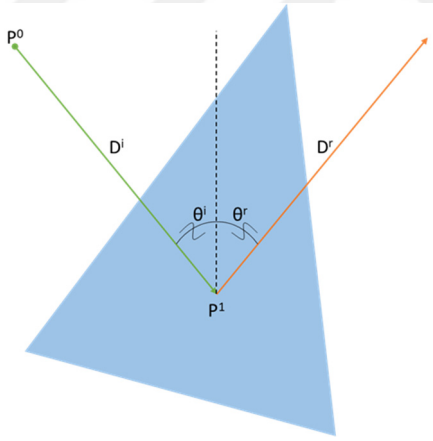

Figure 2.6. Reflection from a triangle

As mentioned above, the incident ray, surface normal, and the reflected ray are on the same plane. The case could be examined in detail by using the perpendicular view shown in Figure 2.7.

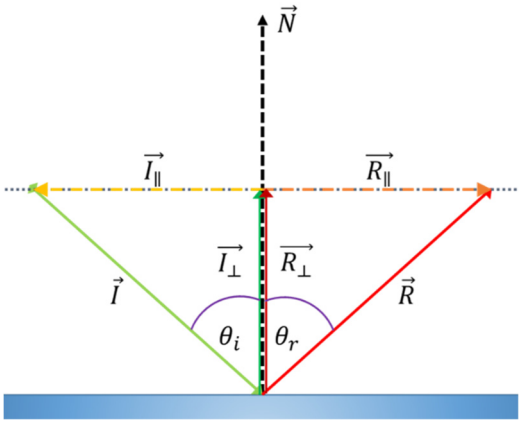

Figure 2.7. Reflection plane with the incident and reflected rays' components

As mentioned above, the reflection angle θ_r is equal to incidence angle θ_i. This equality leads us to the Equation (30):

$$\vec{R} \cdot \vec{N} = -\vec{I} \cdot \vec{N} \tag{30}$$

The second result of the incident and reflected angles equation is that the parallel and perpendicular components of the incident and reflected vectors are equal in length. For convenience, the incident vector is decomposed into parallel and perpendicular components with reversed directions (parallel and perpendicular components of $-\vec{I}$ vector are taken into account as in the figure). From the figure, it is known that:

$$\overrightarrow{R_{\parallel}} = -\overrightarrow{I_{\parallel}} \tag{31}$$

The parallel components are the difference between the vectors themselves and their perpendicular components. The perpendicular components are the projection of vectors onto the surface normal vector. Then the following equations could be found:

$$\begin{aligned} \overrightarrow{R_{\parallel}} &= \vec{R} - \overrightarrow{R_{\perp}} = \vec{R} - (\vec{R} \cdot \vec{N})\vec{N} \\ \overrightarrow{I_{\parallel}} &= -\vec{I} - \overrightarrow{I_{\perp}} = -\vec{I} - (-\vec{I} \cdot \vec{N})\vec{N} \end{aligned} \tag{32}$$

When Equation (31) and Equation (32) are combined, Equation (33) is acquired:

$$\vec{R} - (\vec{R} \cdot \vec{N})\vec{N} = -(-\vec{I} - (-\vec{I} \cdot \vec{N})\vec{N}) \tag{33}$$

From the figure, it is also known that the perpendicular components are equal. The reflection vector part of Equation (32) could be rewritten as in Equation (34):

$$\overrightarrow{R_{\parallel}} = \vec{R} - \overrightarrow{R_{\perp}} = \vec{R} - \overrightarrow{I_{\perp}} = \vec{R} - \left(-\vec{I} \cdot \vec{N}\right)\vec{N} \tag{34}$$

This equation could be replaced in Equation (33), and then the reflection vector is calculated as in Equation (35) [14]:

$$\vec{R} - \left(-\vec{I} \cdot \vec{N}\right)\vec{N} = -\left(-\vec{I} - \left(-\vec{I} \cdot \vec{N}\right)\vec{N}\right)$$

$$\vec{R} = \vec{I} + \left(-\vec{I} \cdot \vec{N}\right)\vec{N} + \left(-\vec{I} \cdot \vec{N}\right)\vec{N} \tag{35}$$

$$\vec{R} = \vec{I} + 2\left(-\vec{I} \cdot \vec{N}\right)\vec{N}$$

All three steps of the ray-tracing procedure are completed. The process is recursive. The reflected ray will be the incidence ray for the second iteration. All the intersection and calculating the reflected ray direction steps are repeated.

2.4 Field Calculations

The field calculations of the SBR method are based on the field formulations given in [9]. By using the ray paths, the field at the exit ray, which is also called the aperture field, is determined by using the recursive relation between the incident and reflected fields at each reflection. The amplitude of the field after the reflection can be calculated by using the formula shown in Equation (36):

$$E_{i+1} = (DF)_i (\Gamma)_i E_i e^{-j\varphi} \tag{36}$$

where E_i is the incident and E_{i+1} is the reflected field at i^{th} reflection. $(DF)_i$ is the divergence factor used in the study in [9]. However, in this study, since the planar triangular meshes are used for modeling the cavities, the divergence factor is taken as one ($(DF)_i = 1$ for all reflections in this study). $(\Gamma)_i$ is the planar reflection coefficient at i^{th} reflection. The details about the planar reflection coefficient

calculation will be given in the next section. Finally, φ is the phase term, and it is given in (37):

$$\varphi = k_0\sqrt{(x_{i+1} - x_i)^2 + (y_{i+1} - y_i)^2 + (z_{i+1} - z_i)^2} \tag{37}$$

2.4.1 Planar Reflection Coefficient

The absorbing materials used in this study are PEC-backed one-layer materials. In this scope, the reflection coefficient formulas given in [9] are used. In this formulation, there is an analogy between the reflection of the rays and the reflection from transmission lines. As seen in Figure 2.8, two mediums on the left side, air, and the absorbing material, are modeled as impedances on the figure on the right side. The planar reflection coefficients are determined by this analogy.

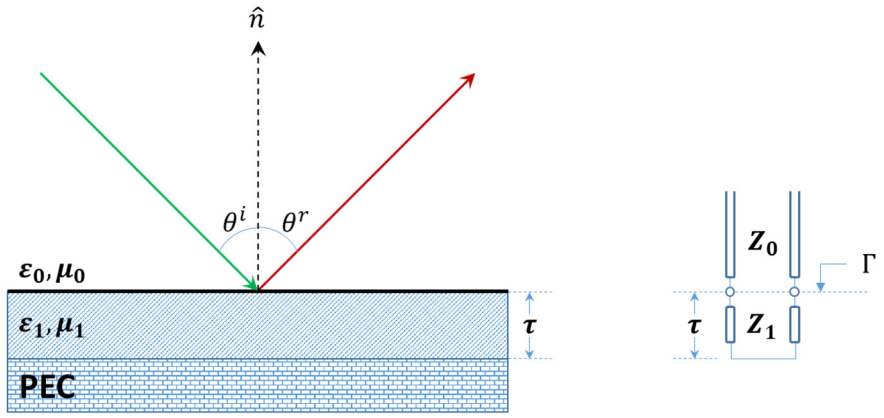

Figure 2.8 Transmission line analogy for the planar reflection coefficient

For the oblique incidence case, the propagation vector $(\vec{k})$ and the surface normal vector $(\vec{n})$ form a plane, namely the "plane of incidence". The electric field is polarized in two different ways according to that plane of incidence: either it is perpendicular to this plane or in this plane. These two polarizations are called perpendicular (transverse electric [TE] or horizontal) and parallel (transverse magnetic [TM] or vertical) polarizations, respectively. Reflection coefficients are decomposed to these components of transverse electric (TE) and transverse magnetic

(TM). For each mesh element, according to the material of the related mesh element, the reflection coefficients are calculated and stored for different reflection angles. The calculation steps are given in the following formulations for TE and TM cases separately:

$$\beta_{Z_0} = \omega\sqrt{\varepsilon_0\mu_0}\cos\theta_i \tag{38}$$

$$\beta_{Z_1} = \omega\sqrt{\varepsilon_1\mu_1 - \varepsilon_0\mu_0\sin^2\theta_i} \tag{39}$$

where ε_0 and μ_0 are the permittivity and permeability values for free space, ε_1 and μ_1 are the permittivity and permeability values for the material medium. θ_i is the reflection angle varying from 0° to 90° and ω is the angular frequency which is equal to $2\pi f$.

2.4.1.1 TE (Perpendicular or Horizontal) Case

$$Z_0 = \omega\mu_0/\beta_{Z_0} \tag{40}$$

$$Z_1 = \omega\mu_1/\beta_{Z_1} \tag{41}$$

$$Z_2 = jZ_1\tan(\beta_{Z_1}\tau) \tag{42}$$

$$\Gamma_{TE} = \left|\frac{1 - Z_0/Z_2}{1 + Z_0/Z_2}\right| \tag{43}$$

where τ is the thickness of the material.

A comparative example is shown in Figure 2.9. The material properties are chosen as follows:

$$\varepsilon = 8 - j1.2$$

$$\mu = 4 - j1.1$$

For this material, the calculated reflection coefficient at TE polarization is compared with the results from FEKO in Figure 2.9. The results are the same for all reflection angles:

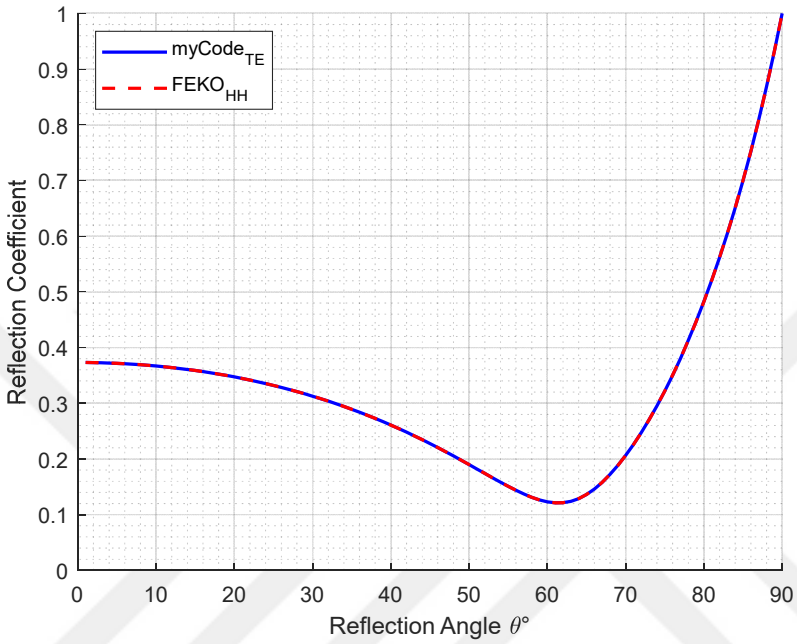

Figure 2.9 Reflection Coefficient Comparison for HH Polarization

2.4.1.2 TM (Parallel or Vertical) Case

$$Z_0 = \beta_{Z_0}/\omega\varepsilon_0 \tag{44}$$

$$Z_1 = \beta_{Z_1}/\omega\varepsilon_1 \tag{45}$$

$$Z_2 = jZ_1 \tan\left(\beta_{Z_1}\tau\right) \tag{46}$$

$$\left|\Gamma_{TM} = \frac{1 - Z_0/Z_2}{1 + Z_0/Z_2}\right| \tag{47}$$

where τ is the thickness of the material.

A comparative example is shown in Figure 2.10. The material properties are chosen as the same in the previous case for TM polarization:

$$\varepsilon = 8 - j1.2$$

$$\mu = 4 - j1.1$$

For this material, the calculated reflection coefficient at TM polarization is compared with the results from FEKO in Figure 2.10. The results are the same for all reflection angles:

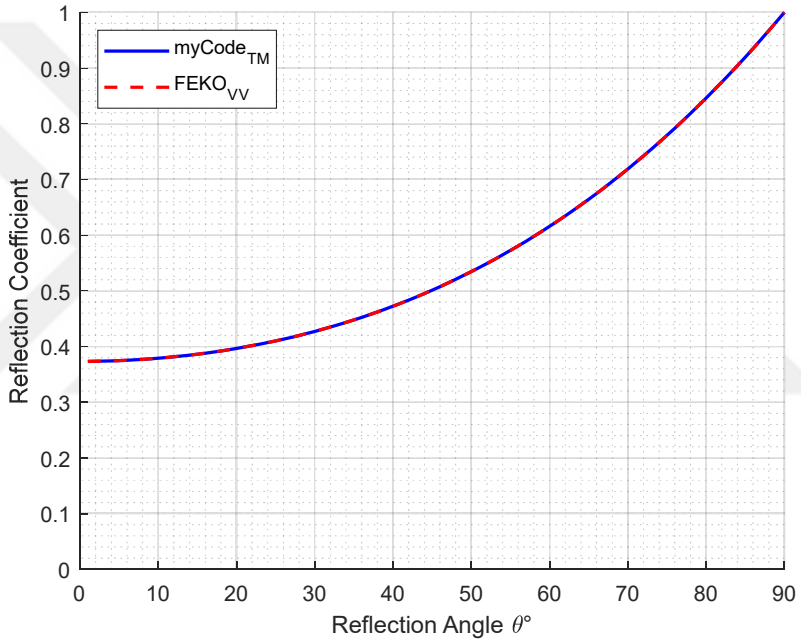

Figure 2.10 Reflection Coefficient Comparison for VV Polarization

2.4.2 Direction of Fields

The directions of the electric field after the reflection and refraction are determined according to Snell's law. Then, the direction of the magnetic field is determined by:

$$\vec{H} = \frac{1}{\eta}\left(\vec{k} \times \vec{E}\right) \tag{48}$$

The incident electric field is decomposed in its polarizations to decide the direction. Two polarization cases are investigated in details in the following sections.

2.4.2.1 TE (Perpendicular or Horizontal) Case

The representation of reflection for TE polarization is shown in the following figure, Figure 2.11:

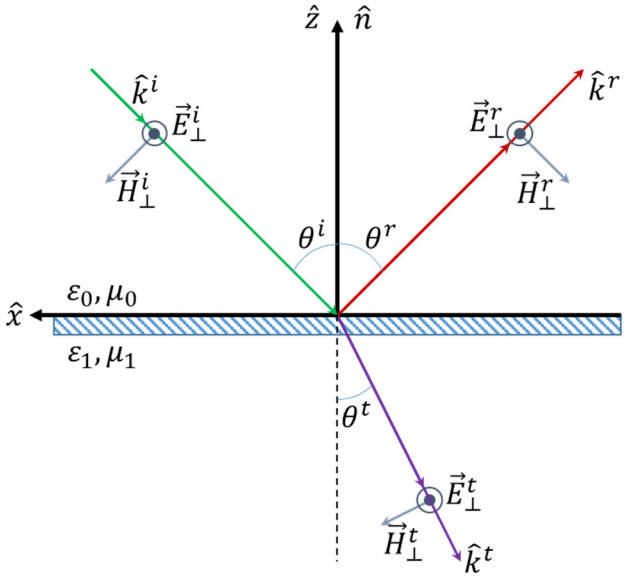

Figure 2.11 Reflection on HH Polarization

In the TE polarization case, the direction of the electric field is not changed according to Snell's law. Since the directions of propagation and electric field are known, the direction of the magnetic field can be found directly by using the formulation given in Equation (48).

2.4.2.2 TM (Parallel or Vertical) Case

The representation of reflection for TM polarization is shown in the following figure, Figure 2.12:

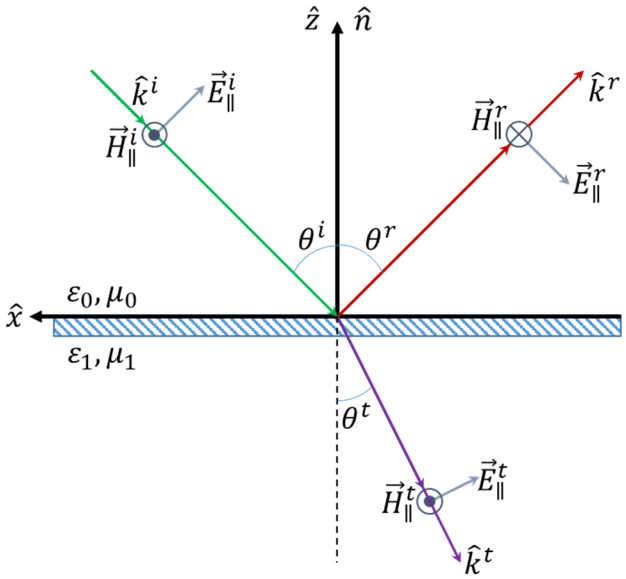

Figure 2.12 Reflection at VV Polarization

In the TM polarization case, the direction of the electric field is found by using Snell's law (as in Figure 2.13). Since the directions of propagation and electric field are known, the direction of the magnetic field can be found directly by using the formulation given in Equation (48).

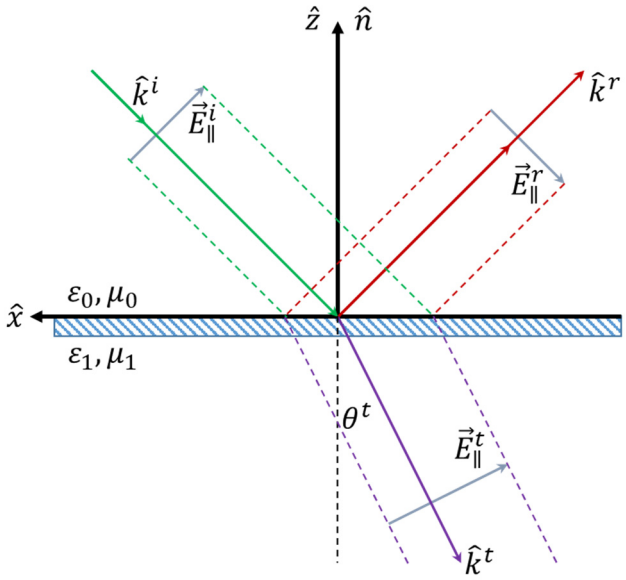

Figure 2.13 Direction of Electric Field for Oblique Reflections

The formulation for the direction of the reflected electric field in terms of incident electric field and the surface normal is given in Equation (49):

$$\vec{E}_r = \left(2\left(\vec{n} \times \vec{E}_i\right)\right) \times \vec{n} - \vec{E}_i \tag{49}$$

In this formulation, steps can be explained in the following equations:

$$\left(\vec{n} \times \vec{E}_i\right) = |\vec{n}|\left|\vec{E}_i\right| \sin\left(90 - \theta^i\right)(-\hat{y}) = \left|\vec{E}_i\right| \cos\theta^i\,(-\hat{y}) \tag{50}$$

$$\left(2\left(\vec{n} \times \vec{E}_i\right)\right) \times \vec{n} = 2\left|\vec{E}_i\right| \cos\theta^i\,(-\hat{y}) \times \vec{n} = 2\left|\vec{E}_i\right| \cos\theta^i\,(-\hat{x}) \tag{51}$$

$$\left(2\left(\vec{n} \times \vec{E}_i\right)\right) \times \vec{n} - \vec{E}_i = 2\left|\vec{E}_i\right| \cos\theta^i\,(-\hat{x}) - \vec{E}_i = 2\vec{E}_{i,x} - \vec{E}_i \tag{52}$$

Equation (52) is illustrated in Figure 2.14 based on the field representation in Figure 2.13.

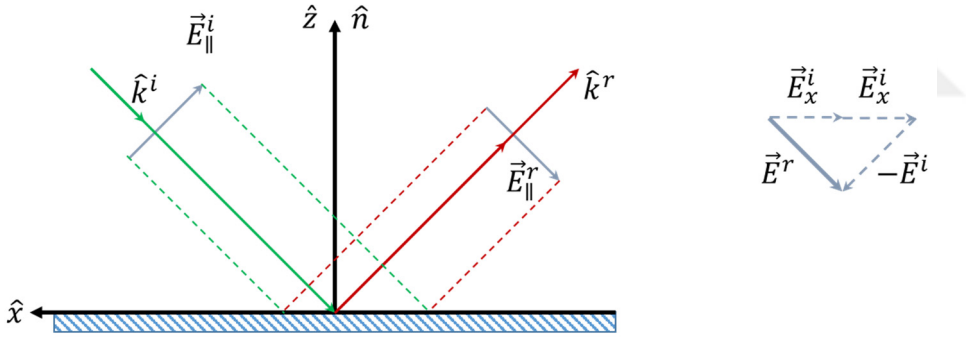

Figure 2.14 Reflected Field in terms of Incident Field

2.4.3 Aperture and Backscattering Fields

In the SBR method, the backscattered field is computed by the Physical Optics (PO) approximation. In PO approximation, a known aperture field is replaced by an equivalent magnetic current on the aperture by using the following formula in Equation (53):

$$\vec{M}_s = \begin{cases} 2\vec{E}^A \times \hat{n}^A, & on\ the\ aperture \\ 0, & out\ of\ the\ aperture \end{cases} \tag{53}$$

where $\vec{E}^A$ is the aperture field and $\hat{n}^A$ is the aperture normal. The aperture fields are the fields at the last reflected ray, which is given by Equation 54:

$$\vec{E}^A = \vec{E}^r e^{-jk_0 l} \tag{54}$$

where l is the ray path taken by the ray.

The backscattered field is calculated by using the aperture field as:

$$\vec{E}^s = \frac{e^{-jk_0 r}}{r}\left[A_\varphi \hat{\varphi}^i + A_\theta \hat{\theta}^i\right] \tag{55}$$

$$\begin{bmatrix} A_\varphi \\ A_\theta \end{bmatrix} = \frac{jk_0}{2\pi} \iint_{\Sigma_A} e^{jk_0[(\cos\varphi^i \sin\theta^i)x + (\sin\varphi^i \sin\theta^i)y]}\, dx\, dy \cdot \begin{bmatrix} E_x \cos\varphi^i + E_y \sin\varphi^i \\ \left(-E_x \sin\varphi^i + E_y \cos\varphi^i\right)\cos\theta^i \end{bmatrix} \tag{56}$$

where E_x and E_y are the x and y components of the aperture field on the aperture Σ_A. The RCS values are obtained from the formulations given in Equations (57)-(60):

$$\sigma_{\varphi\varphi} = 4\pi\left|A_\varphi\right|^2 \ where\ E^i\ is\ horizontally\ polarized. \tag{57}$$

$$\sigma_{\theta\varphi} = 4\pi|A_\theta|^2 \ where\ E^i\ is\ horizontally\ polarized. \tag{58}$$

$$\sigma_{\theta\theta} = 4\pi|A_\theta|^2 \ where\ E^i\ is\ vertically\ polarized. \tag{59}$$

$$\sigma_{\varphi\theta} = 4\pi\left|A_\varphi\right|^2 \ where\ E^i\ is\ vertically\ polarized. \tag{60}$$

CHAPTER 3

CODING RAY TRACING ALGORITHM, GUI OF RAY TRACING TOOL AND FIELD AND RCS CALCULATION PROCESS

In this chapter, the details about the algorithm and GUI of the ray-tracing tool are investigated. The subcategories of the algorithm part are inputs, the decision of ray starting points, the decision of intersection points, recursion, and outputs. In the GUI part, input and output tabs are the subcategories that are investigated. In the last section of this chapter, the details about the field and RCS calculation codes are given.

3.1 Coding Ray Tracing Algorithm

The ray-tracing algorithm requires the model as a mesh of triangles, the angular interval that needs to be scanned, and the conditions related to ray density and bounce number limit. By using these inputs, the ray starting points are determined at first. In the next step, the intersection points are calculated for each ray recursively until the ray exits from the model (no intersection found) or reaches the bounce limit. The outputs are stored in a .txt file with a specific format. The details about the coding process are given in the next sections below.

3.1.1 Inputs

In the algorithm, the model's mesh and the angular interval of interest are the primary inputs. Parameters such as ray density and the maximum number of bounces are also input parameters decided by the user.

The input mesh file stores the nodes (vertices) and connectivity (faces) of triangular meshes used to model the cavity. There are two options for mesh files: FEKO .unv mesh file or separate .txt files for faces, and vertices of mesh could be taken as mesh inputs. In this study, FEKO .unv mesh files are used. However, mesh files from other simulation tools could also be used after some basic manipulations on MATLAB.

There are a few points that need to be taken into account while creating mesh files. First of all, all the surfaces must be stitched to prevent any escaped rays from the spaces between adjacent triangles. In FEKO, *Union* or *Stitch* commands [15] could be used (under the *construct* tab). The second important issue is the direction of the surface normal vectors. All the surface normal vectors must be towards the inside of the cavity. In the following figure (Figure 3.1), the green sides show the direction of the surfaces, whereas the red sides show the opposite direction. The illustration on the right is the correct way of surface normal vector orientation for ray tracing simulation for the cavity. In the algorithm, rays reflect only from the same side of the surface normal, green sides in FEKO.

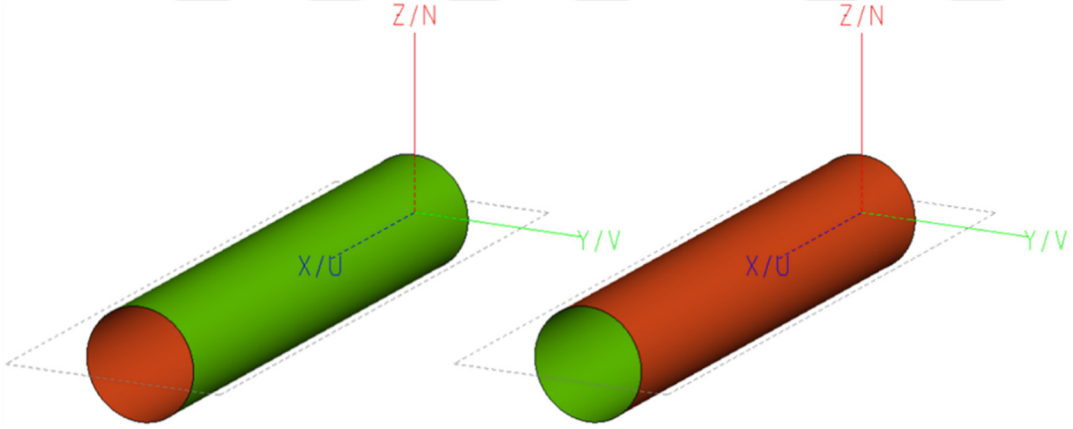

Figure 3.1 Surface normal representation on FEKO

For the second case, the rule for the surface normal vector orientation (given above) must be obeyed. The other issue could be explained with an example. In the *Faces File*, each row consists of three vertex numbers. These numbers give the row number of the corresponding vertex in the *Vertices File*. Some simulation tools refine the mesh, and during the refinement process, some vertices could be merged. At that

point, the numbers of the vertices could not be a series from 1 to the number of vertices. This situation could explode the running code. The last thing about the faces and vertices files is that there must not be an extra empty row at the end of the files.

Azimuth angle φ is defined on xy-plane, from x-axis to y-axis, as in Figure 3.2. Elevation angle θ is defined from z-axis to xy-plane.

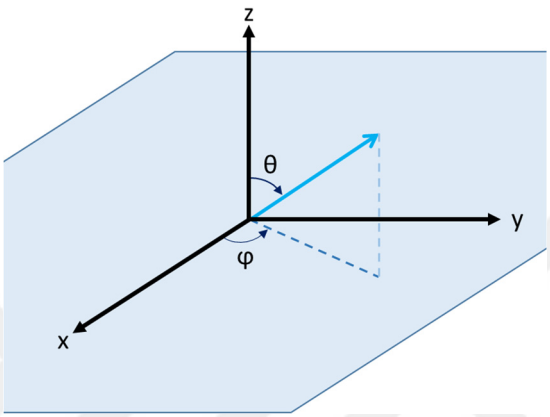

Figure 3.2 Azimuth and Elevation definitions used in ray-tracing tool

The other parameters that should also be defined by the user are listed below:

- The *frequency* value is used to determine the wavelength. The unit of the frequency parameter is taken as GHz in the algorithm.
- *Ray density* is defined as ray per wavelength. An increase in the ray density generates more rays, takes a longer time, and results in a larger output file
- *Bounce Limit* gives the maximum number of reflections that will be traced during the analyses.

The last point that needs to be decided by the user is about to benefit from the cavity entrance nodes. The cavity entrance could be used to minimize the number of rays generated in the first phase. Depending on the user's choice, rays aim only at the cavity entrance in the algorithm, not the rest of the model.

The input parameters required by the ray-tracing algorithm are listed below in Table 1:

Table 1 Input parameters required for ray tracing algorithm

Parameter ID	Type	Notes
freq_G	Double	Frequency in GHz
dist_coef	Double	Ray density
useCavityEntrance	Boolean	Rays to cavity entrance or not
file_entr	String	Cavity entrance nodes (output) file
file_stats	String	Ray statistics (output) file
file_node	String	Vertices file
file_face	String	Faces file
az_start	Double	Start angle of azimuth in degree
az_step	Double	Angular step in azimuth in degree
az_stop	Double	Stop angle of azimuth in degree
el_start	Double	Start angle of elevation in degree
el_step	Double	Angular step in elevation in degree
el_stop	Double	Stop angle of elevation in degree
max_bounce	Integer	Maximum bounce number

3.1.2 The Decision of Ray Starting Points

In the algorithm, there are two ways to determine the start points of rays.

If the user wants to benefit from the cavity entrance nodes to reduce the number of rays at the first phase, then the edges of the cavity opening are found firstly. Maximum and minimum values of x, y, and z components of those edges are found to create a bounding box for cavity entrance. In the next step, the vertices of that box are projected to the plane perpendicular to the incidence direction. The maximum distance of the model decides the distance of that plane from the cavity model. On the projection plane, two perpendicular vectors are found to correspond to the up and right directions. Using these vectors, the most upward, the most right, the most downward, and the most left points of projected bounding box vertices are

determined. An imaginary rectangular region is created on the projection plane, and the start points are located on that rectangular zone with an equally spaced pattern. The user determines the distance between neighbor start points in terms of wavelength.

As a second option, the cavity entrance nodes are not be used by the algorithm, then the same procedure described above is applied with only one difference: The bounding box is generated by using the whole cavity model. In this case, some of the launched rays do not intersect with the inside of the cavity, and they cannot be traced. However, it could be useful for some specific applications, for instance, an application where the outer body of the model is also important.

3.1.3 The Decision of Intersection Points

In the ray–triangle intersection process, before mentioned Möller – Trumbore algorithm is used. One of the most critical issues is the comparison of floating-point numbers [16][17]. During the comparison of determinant values, a pre-defined error term, DBL_EPSILON, is used. The code (Figure 3.3) for comparison functions could be given as follows:

```
bool definitelyGreaterThan(double a, double b) {
    return (a - b) > ( (fabs(a) < fabs(b) ? fabs(b) : fabs(a)) * DBL_EPSILON);
}

bool definitelyLessThan(double a, double b) {
    return (b - a) > ( (fabs(a) < fabs(b) ? fabs(b) : fabs(a)) * DBL_EPSILON);
}
```

Figure 3.3 Code of the comparison functions

The details of the Möller – Trumbore ray-triangle intersection algorithm [12] are already given in section 2.2.2. above.

3.1.4 Recursion

The most complex part of the algorithm is the recursion part. The procedure is summarized in Figure 3.4.

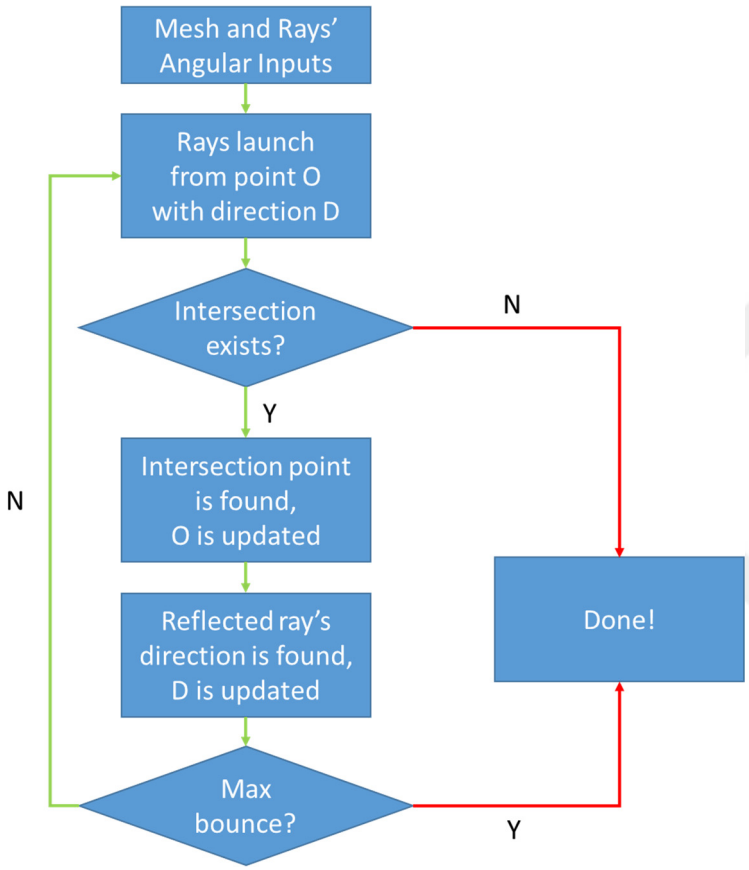

Figure 3.4 The recursive algorithm used in the ray-tracing tool

If the user wants to use a strictly limited bounce number, there will be no stored data for any ray that reflects more than the maximum bounce number limit. If not, the data of reflections up to the maximum bounce number limit will be stored for the rays that reflect more than the maximum bounce number limit.

In C++, handling memory is an essential and critical issue [18]. After each ray's tracing process, output data is written to the output file, and the memory is cleared. Otherwise, memory overflow (heap overflow, stack overflow) errors could lock the computer.

3.1.5 Outputs

The algorithm's output is mainly the statistics of the rays. Rays' starting and bouncing points and directions are stored in a text file for the post-process. In the algorithm, the format of the output file is divided into two different types:

- "%d%f%f%f%f%f%f%f%d" for the start point,
- "%d%f%f%f%f%f%f%d" for reflection point.

The stored data for the start points are bounce order which is 0, x, y, z components of starting point, x, y, z components of the ray direction, the azimuth angle in degree, elevation angle in degree, and the total bounce number for that specific ray. For the other points, reflection points, the stored data are bounce order, x, y, z components of starting point, x, y, z components of the ray direction, reflection angle in degree, and the triangle number that is intersected. They are required to make the post-process simpler and quicker.

3.2 GUI of Ray Tracing Tool

GUI is required to view all work of this study in an organized manner. Two main tabs are designed for this purpose: Inputs and Outputs tabs. In the Inputs tab, all required information provided by the user is taken and stored by the GUI to generate input files. The executable C++ file, "tRays.exe", takes the inputs from a text file called "inputs.txt". In this text file, the input parameters listed in Table 1 should be written. This process is completed at the end of the first tab. After the ray tracing process is completed, a text file called "…_ray_stats.txt" is generated. The main post-process routines are also handled by the GUI in the Outputs tab. The details are provided in the next two sections.

3.2.1 Inputs Tab

The inputs are mainly the mesh inputs, angular definitions, and analysis conditions. The input tab is shown in Figure 3.5.

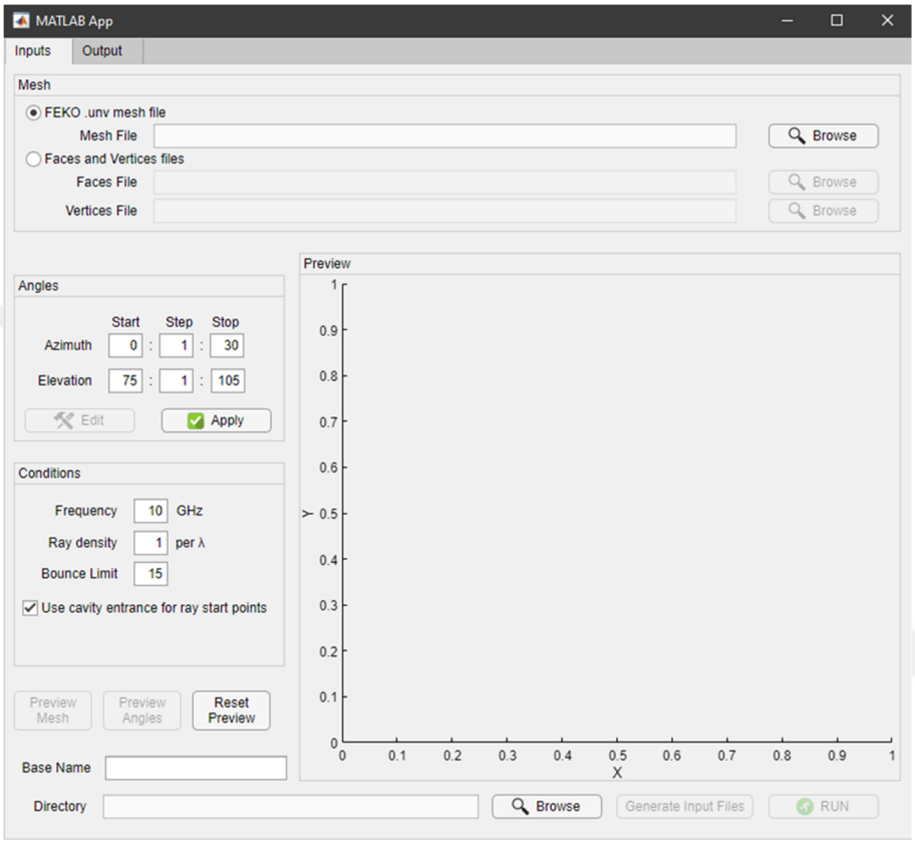

Figure 3.5 Inputs Tab of ray tracing tool's GUI

There are three main blocks in the Inputs tab. Two different alternatives can be chosen for the mesh of the model, as in Figure 3.6. FEKO .unv type of file for mesh input is selected as the default case.

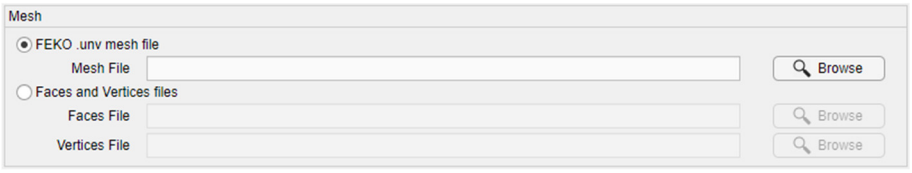

Figure 3.6 Mesh inputs

Angular inputs should be entered in degrees on the Angles block of the Inputs tab in Figure 3.7. If angles are not swept but only one angle exists for the analysis, the angular step must be 0. For instance, to define the ray towards $+x$ to $-x$ direction, the values should be 0, 0, 0, and 90, 0, 90 for azimuth and elevation rows, respectively.

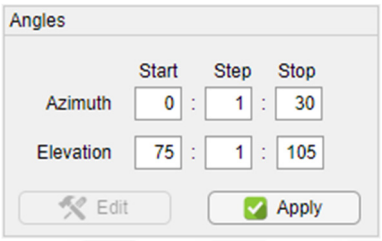

Figure 3.7 Angular inputs

The frequency and the ray density are used together to define the distance between two adjacent rays. The other primary condition for the analyses is the maximum bounce limit. All these values are entered in the Conditions block of the Inputs tab of the GUI, as shown in Figure 3.8.

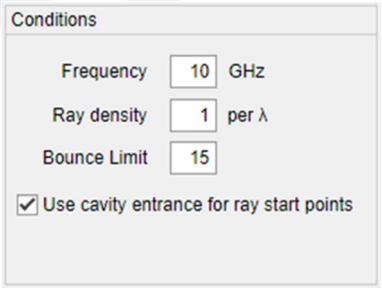

Figure 3.8 Inputs related to the analysis' conditions

Two boolean-type input parameters in Table 1 can be arranged by using the checkboxes in the Conditions block. The checked box means true, and the unchecked box means false in the algorithm running back-end.

3.2.2 Outputs Tab

The second tab, Outputs, is shown in Figure 3.9. The files on the top are automatically taken after analyses. These files can be chosen by the user for the analyses performed in the past. The Plot Type block, located on the left, has five different plot options. The chosen type is illustrated in the Plot block on the right side of the Outputs tab.

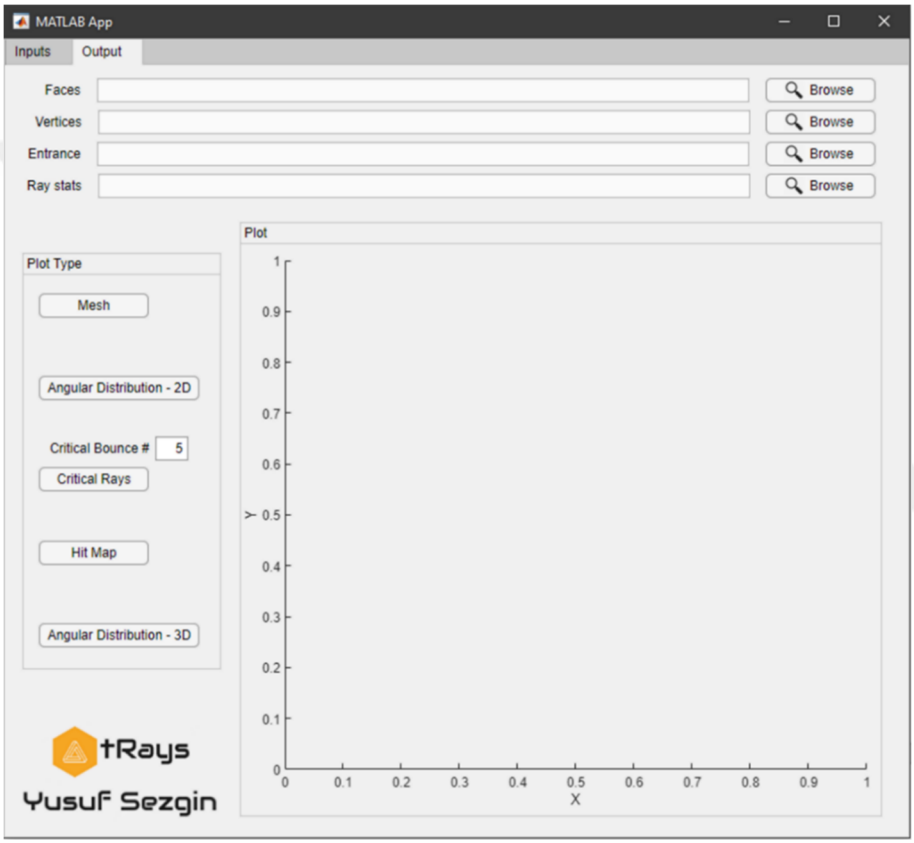

Figure 3.9 Outputs Tab of ray tracing tool's GUI

The mesh of the model can be visualized by clicking "Mesh" button on the Plot Type block. An example is shown in Figure 3.10. Mesh visualization can be played by using MATLAB's plotting abilities.

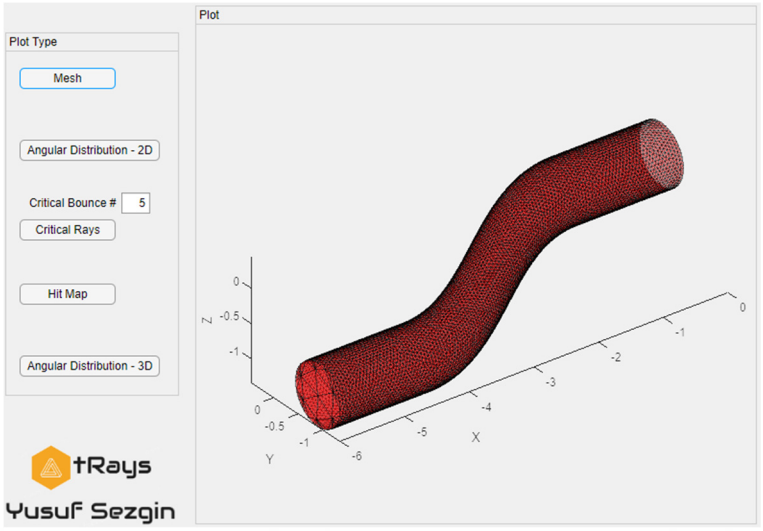

Figure 3.10 Plotting the mesh

The 2D angular distribution example is seen in Figure 3.11. In this graph, the distribution of the reflection angles at all reflections is summarized. The horizontal axis shows the reflection angle in degree. The vertical axis gives the number of reflections at the reflection angles from 0° to 90° for all of the rays that are traced.

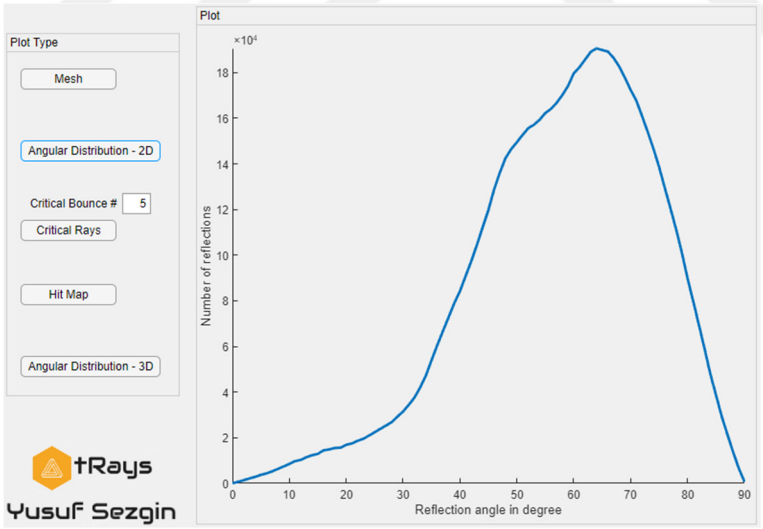

Figure 3.11 2D Angular Distribution

The next button, Critical Rays, has a pre-condition called critical bounce number. The rays which are reflected less than or equal to the critical bounce number are

visualized as shown in Figure 3.12. The green lines show the outgoing rays, whereas the blue ones show the incoming and reflected rays.

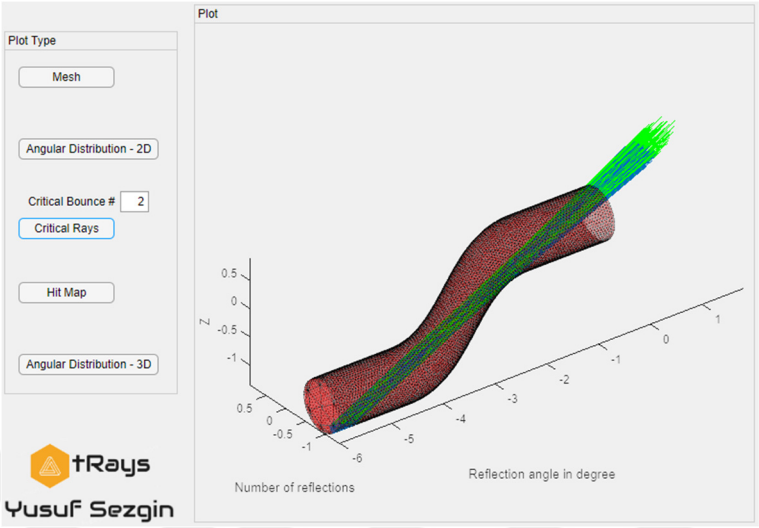

Figure 3.12 Critical Rays

Hit Map button is used to visualize the mesh where the triangles are colored with respect to the number of reflections that occurred at each triangle. An illustration is shown in Figure 3.13.

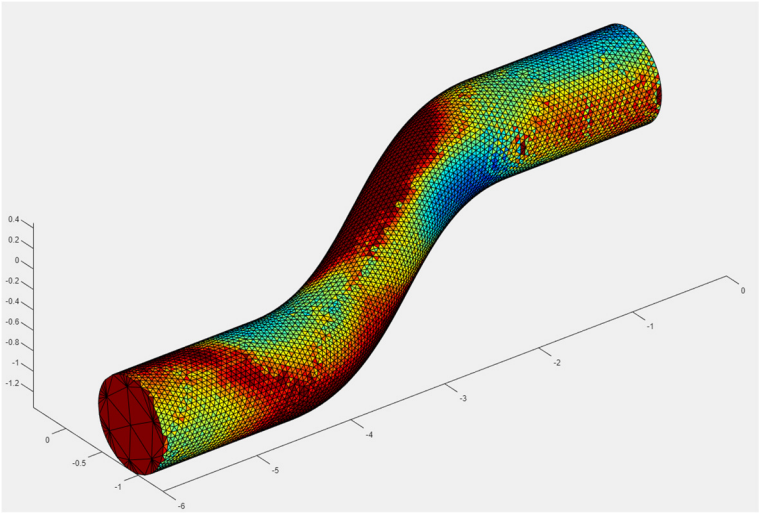

Figure 3.13 Hit Map

The 3D angular distribution example is seen in Figure 3.14. In this case, the triangles are colored according to their reflection statistics. The most observed reflection angle for each triangle is found, and the triangle is colored with respect to that angle.

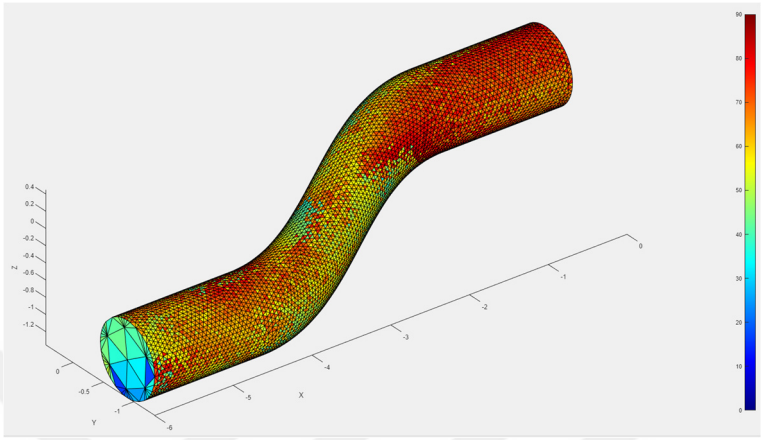

Figure 3.14 3D Angular Distribution

The visualizations provided in the Outputs tab help improve the cavity's stealthiness. Critical ray illustrations can give ideas about the geometric optimization of the model. With the help of these plots, local changes can be applied to the model to increase the reflection numbers. The material application locations can be modified using the hit map and angular distribution plots. The material optimization can be made by using the 2D angular distribution plot. The further details of these processes are given in the next chapters. Additionally, any type of filter can be applied to these plots by using MATLAB scripts. For this study, these plot options are seen as adequate.

3.3 Field Calculations

The ray-tracing procedure is the first step in the SBR method. Since the ray paths are known and stored, field and RCS calculations can be processed separately. In the scope of this study, a post-process tool is developed to calculate the RCS of a given model and given ray file that stores reflection points, directions, angles, etc. There is no GUI for this part of the study.

Incident electric fields for both horizontal and vertical polarizations are created by using the following formulas in Equations (61) and (62):

$$\vec{k} = [-\sin\theta\cos\varphi\,, \quad -\sin\theta\sin\varphi\,, \quad -\cos\theta\,] \tag{60}$$

$$\vec{E}_V = [-\cos\theta\cos\varphi\,, \quad -\cos\theta\sin\varphi\,, \quad \sin\theta\,] \tag{61}$$

$$\vec{E}_H = [\sin\varphi\,, \quad -\cos\varphi\,, \quad 0\,] \tag{62}$$

where $\vec{k}$ is the propagation vector (unit vector in the direction of propagation) as shown in Figure 3.15.

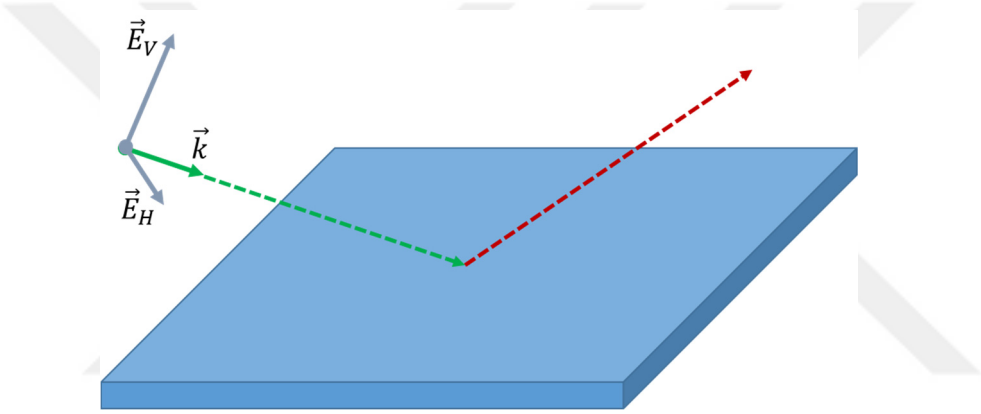

Figure 3.15 Horizontal and vertical polarized electric field vectors and propagation vector

In the post-process, the material information of the triangular meshes is one of the main inputs. According to the material information, the reflection coefficient values for each reflection angle are calculated by using the formulation given in section 2.4.1 above, in Equations (38) to (47). The direction and the amplitude of the fields are calculated by the given formula in section 2.4.2 above, in Equations (48) to (52), for all reflections inside the cavity. Aperture fields are computed by using the field information given in section 2.4.3 above, for each azimuth and elevation angular pair. As a final step, RCS is calculated with the aperture field data for each azimuth and elevation angular pair.

Finally, the RCS results are stored in a 2-D array where the rows correspond to elevation angles, and the columns correspond to the azimuth angles. At that point, visualizing the RCS graphs is straightforward and effortless. In this study, *imagesc* function of MATLAB is used to illustrate the RCS values over 2-D graphs with scaled colors.

CHAPTER 4

CONVERGENCE TESTS

Some parameters, such as mesh size, ray density, maximum bounce number limit, etc., must be determined appropriately to optimize the sources required by the algorithm (memory, time, CPU, etc.). For example, if a fine mesh and a coarse mesh have identical angular distributions, there is no need to use fine mesh since it will significantly increase computation time and memory usage. Convergence tests are applied for those parameters to determine the optimum values. Additionally, RCS results for basic geometries are compared with the results taken from commercial tools.

4.1 Mesh Size Tests

In this section, different mesh sizes of FEKO are generated and compared. For the ray-tracing analysis, the solution method should be selected as RL-GO. In this study, frequency is chosen as the center frequency of the X-Band, 10 GHz. Coarse, standard, and fine meshes are shown in the following figures, Figure 4.1. They have around 1000, 15000, and 35000 triangles, respectively.

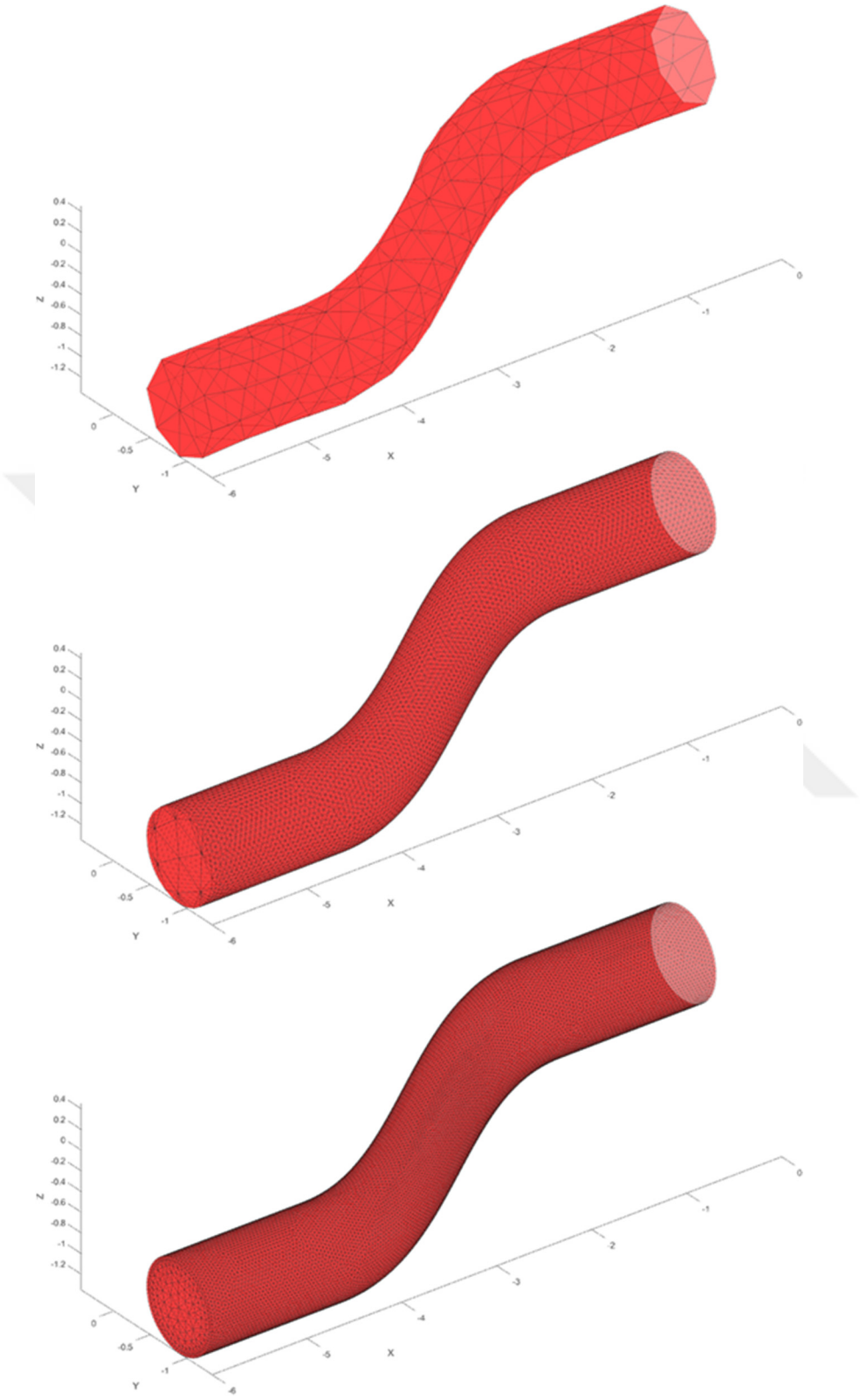

Figure 4.1 Coarse (top), standard (middle) and fine (bottom) meshes

The 2D and 3D angular distributions are illustrated in the figures from Figure 4.2 to Figure 4.4. 2D angular distributions are gathered in one plot to compare in Figure 4.5.

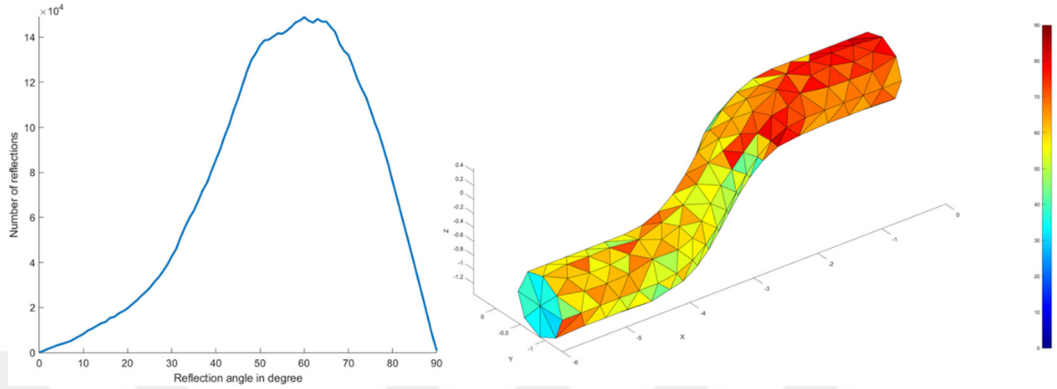

Figure 4.2 2D and 3D angular distributions for coarse mesh case

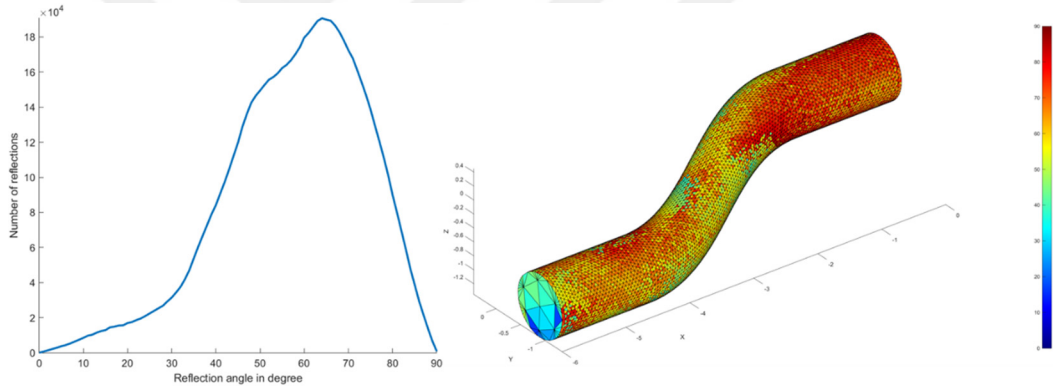

Figure 4.3 2D and 3D angular distributions for standard mesh case

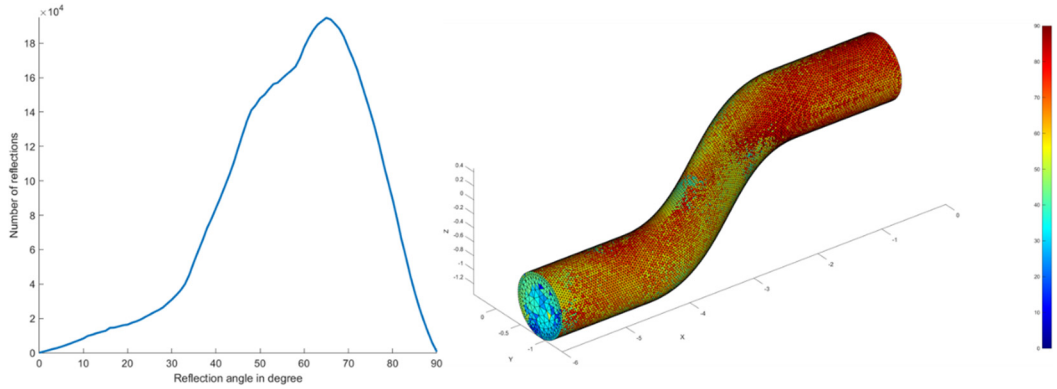

Figure 4.4 2D and 3D angular distributions for fine mesh case

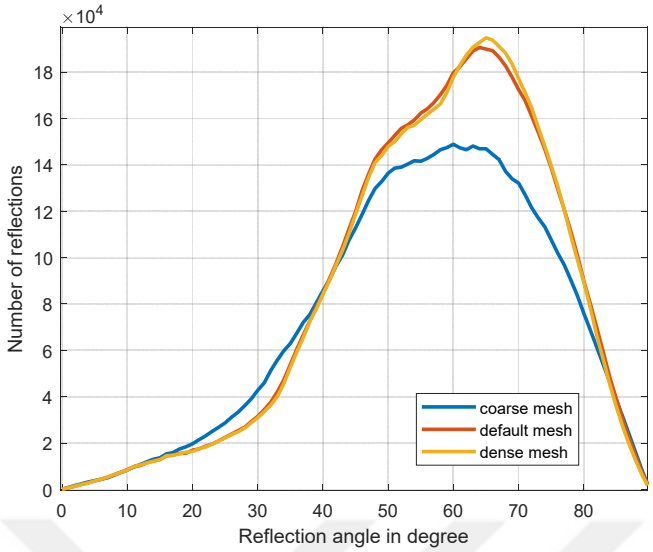

Figure 4.5 2D angular distribution comparison for different mesh cases

It is observed that in the coarse case, both 2D and 3D angular distributions are affected. Especially the 3D angular distribution might mislead the optimization process. Even with the considerable reduction in computation time given in Table 2, the coarse mesh is not appropriate for this optimization study. However, the results are almost identical for the standard and fine mesh cases. Due to the remarkable reduction in computation time, the standard mesh size is selected for this study.

Table 2 Computation times for different mesh sizes

Mesh Case	Computation Time
Coarse	5 minutes
Standard	1 hour 30 minutes
Fine	4 hours 50 minutes

4.2 Ray Density Tests

The next critical parameter which affects the source usage is the ray density. Standard mesh is used to compare the ray density cases. "One ray per wavelength" is selected as the default case. In this case, for the model shown in the middle of

Figure 4.1, around 900 rays are launched (30×30). "One ray per two times wavelength" is selected as the sparse case. "Two rays per wavelength" is determined as the dense case. The 2D and 3D angular distributions are illustrated in the figures from Figure 4.6 to Figure 4.8. The difference in the total reflection numbers can be observed from the y-axis of 2D angular distribution plots. In Figure 4.9, the normalized 2D angular distribution plots are shown in one plot.

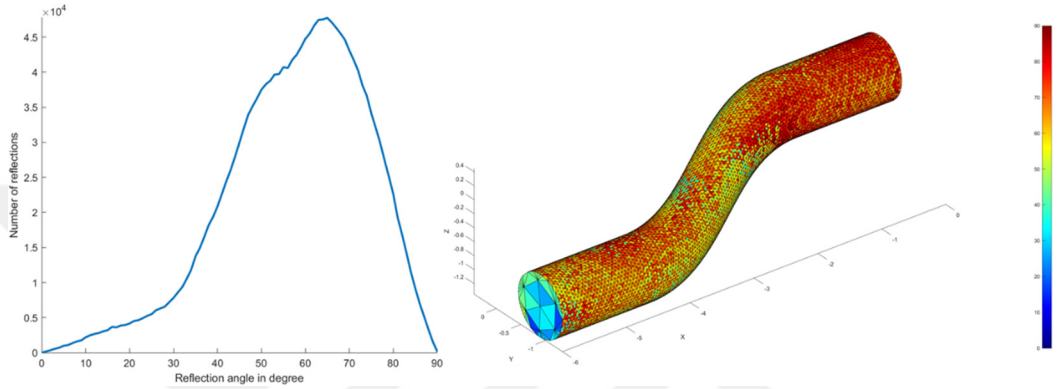

Figure 4.6 2D and 3D angular distributions for sparse ray density case

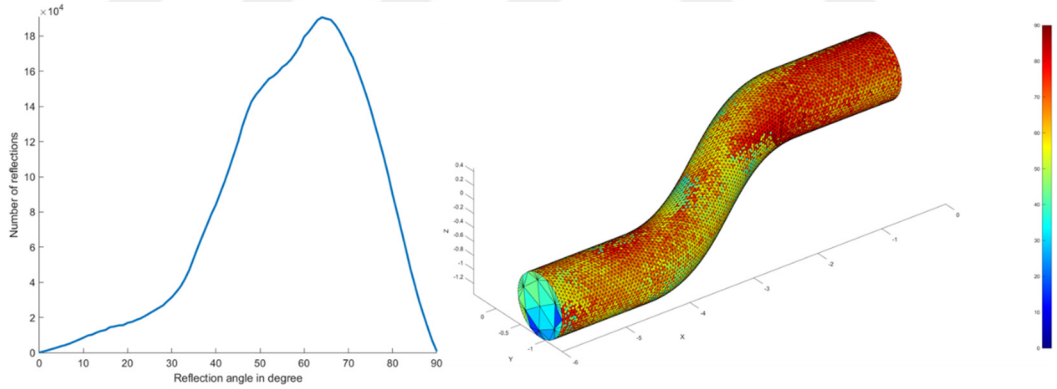

Figure 4.7 2D and 3D angular distributions for default ray density case

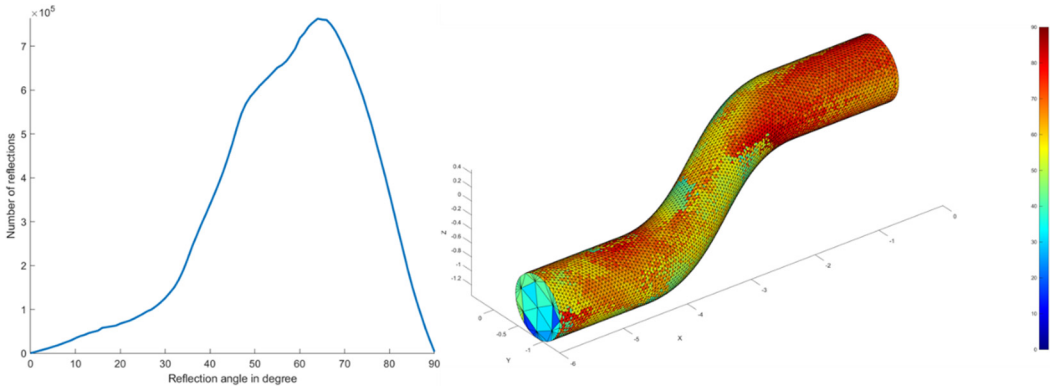

Figure 4.8 2D and 3D angular distributions for dense ray density case

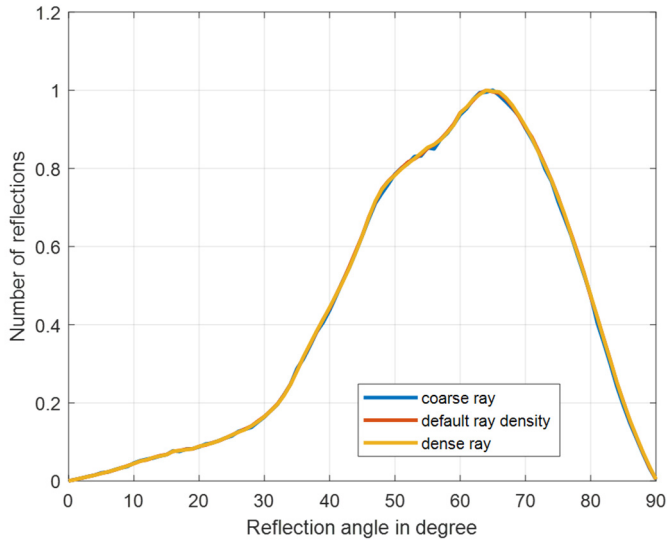

Figure 4.9 Normalized 2D angular distributions for different ray density cases

It is observed that in the coarse case, the 2D angular distribution plot is not smooth as in the other two cases, but still, they are almost the same. It can still be used for optimization, but the other cases seem preferable due to the smoothness of the 2D angular distribution graphs and the differences in 3D angular distribution plots. The bend region of the sparse ray density case has different colors compared to the other cases. On the other hand, both plots are quite similar for default and dense ray density cases. The main difference for these cases is the computation times shown in Table 3. The default case is five times faster than the dense case, which is a huge difference.

The default ray density case, "one ray per wavelength", is used for the ray-tracing analysis in this study.

Table 3 Computation times for different ray densities

Ray density	Computation Time
Sparse	25 minutes
Default	1 hour 30 minutes
Dense	7 hours 30 minutes

4.3 Maximum Bounce Numbers Tests

The maximum bounce number limit can also affect the computation time. In the figure below, Figure 4.10, 2D angular distribution plots for maximum bounce numbers 30, 25, 20, 15, 10, and 5 are illustrated. The same graphs are plotted in one figure, Figure 4.11.

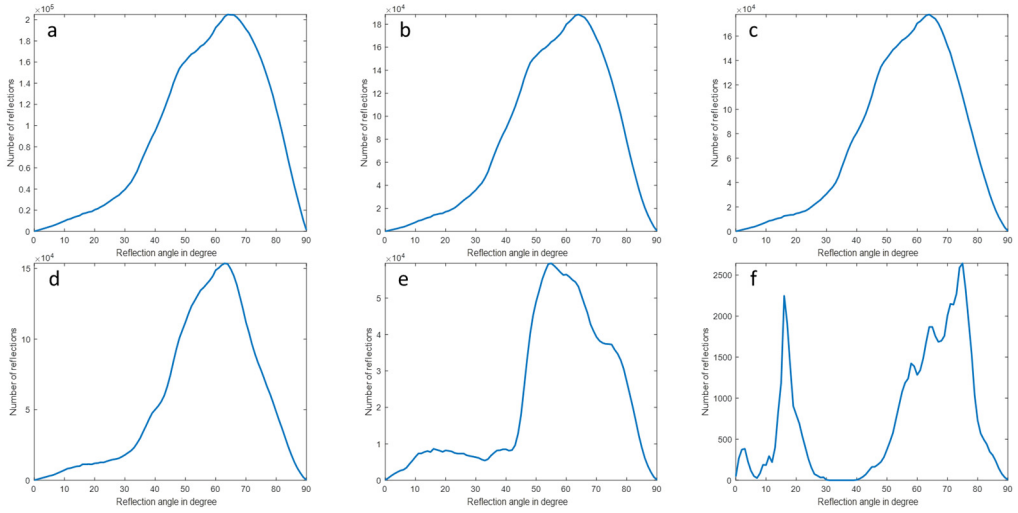

Figure 4.10 2D angular distributions for maximum bounce numbers: (a) 30, (b) 25, (c) 20, (d) 15, (e) 10, and (f) 5

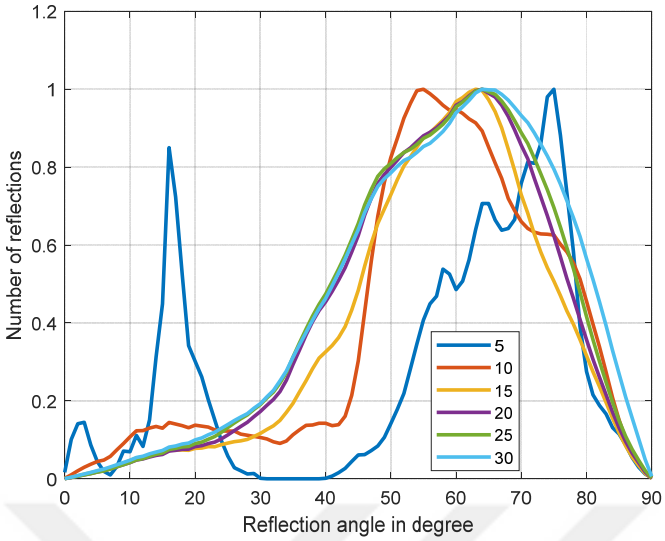

Figure 4.11 Normalized 2D angular distributions for maximum bounce numbers

The computation times for the limits at 15 and 30 bounces are shown in Table 4.

Table 4 Computation times for different bounce limits

Bounce limit	Computation Time
15 bounces	1 hour 30 minutes
30 bounces	2 hours 30 minutes

The plots show that the angular distribution is subject to change especially for the lower number of bounces. After 15 bounces, the graphs are almost the same. 3D angular distributions for 30 and 15 bounces are shown in Figure 4.12, and they are almost identical. Under these circumstances, it is unnecessary to put a limit at 30 bounces. It should also be noted that even with an inefficient absorbing material, with only 4 dBsm absorption, the total absorption makes the field down to one billionth with 15 bounces.

There is an addition regarding the critical rays with the smallest number of reflections. The plot (f) of Figure 4.10 might provide a clue about the material optimization for only the critical rays. The RCS value at azimuth and elevation pair at which the critical rays occur could be reduced by using this plot. It shows that the

peak at around 15° is as important as the peak at around 70° for critical rays in this example. In the end, for the average RCS, not only the critical rays but also the other rays should be considered for absorption.

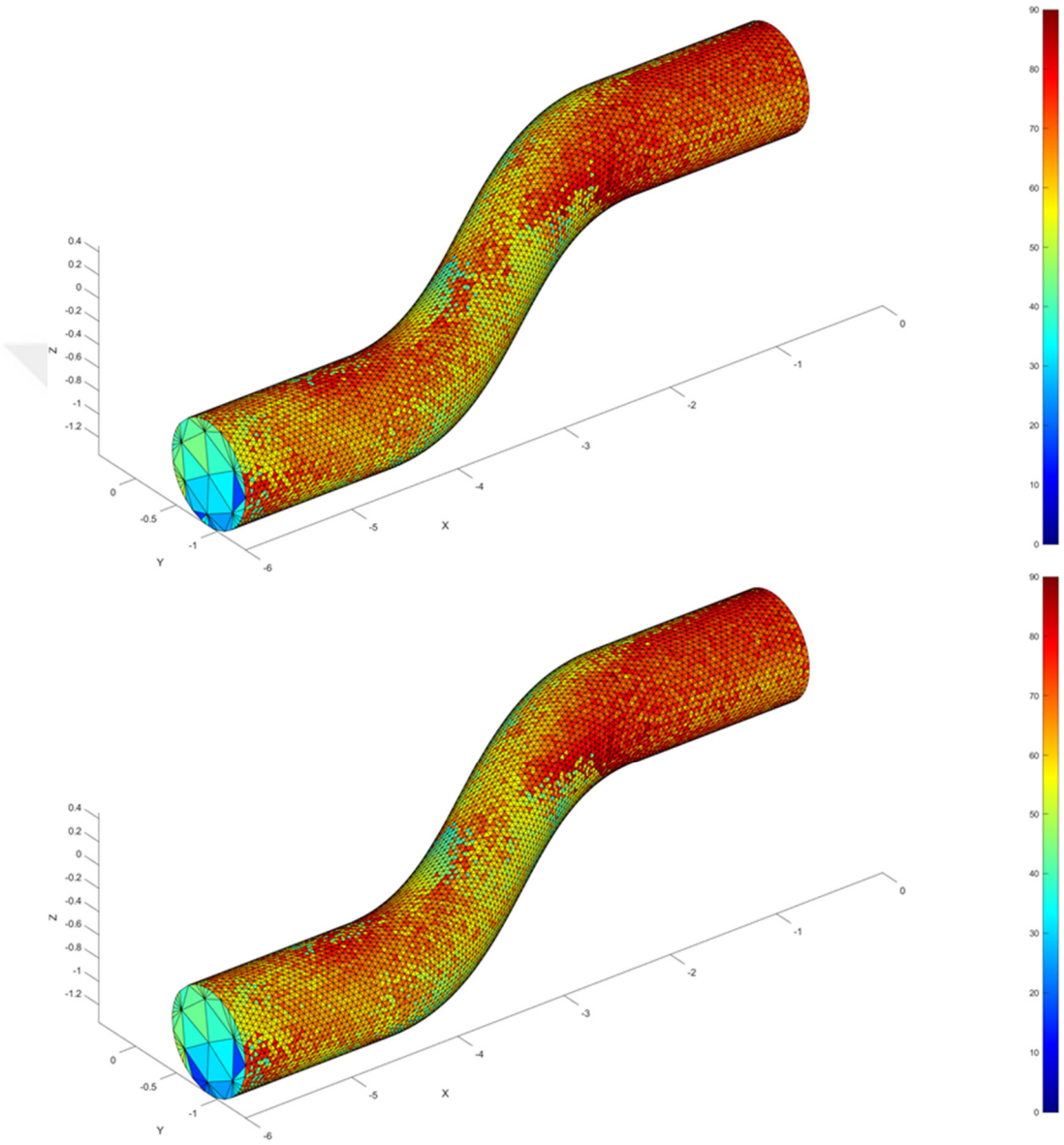

Figure 4.12 3D angular distributions for maximum bounce limits 30 (top) and 15 (bottom)

4.4 RCS of basic geometries

In this section, RCS values for given basic geometries are compared with the results taken from a commercial CEM solver (HFSS SBR) for PEC and coated cases. In the coated cases, the material is chosen as the material shown in previous sections for the planar reflection coefficient.

4.4.1 Square Plate

The first model is a square plate with 1-meter width and height. In this case, the results show the performance of the PO part of the SBR code since there exists only one reflection from the target. The test model is illustrated in Figure 4.13. The analyses are performed on angular scans from -60° to +60° elevation, as in Figure 4.14.

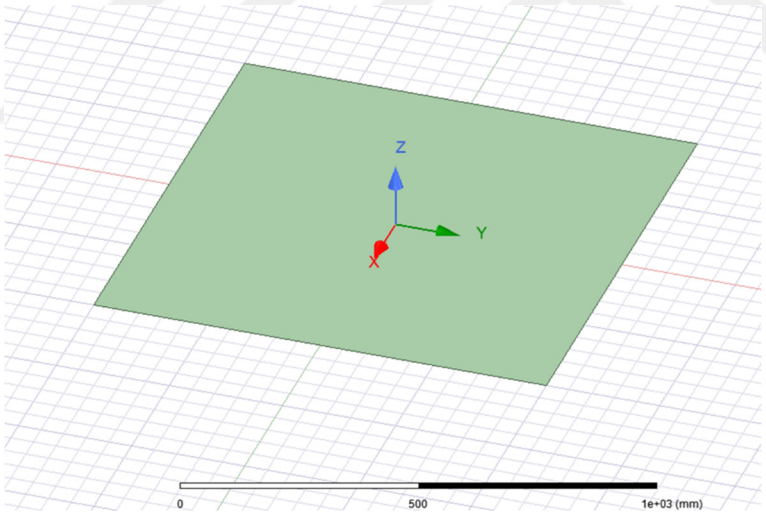

Figure 4.13 Square Plate

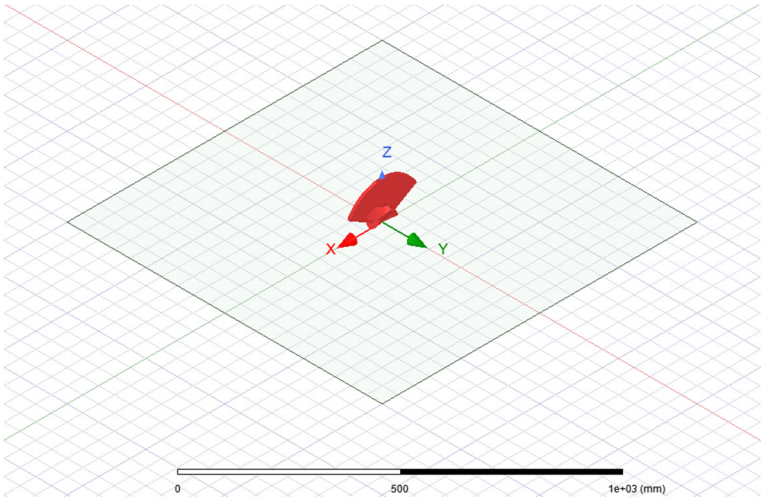

Figure 4.14 Angular scan on square plate

4.4.1.1 PEC Case

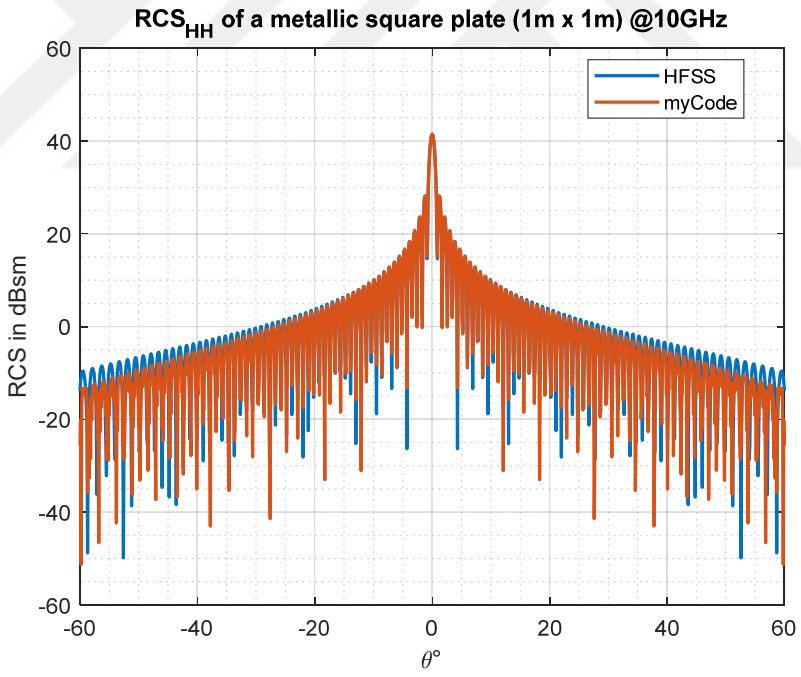

Figure 4.15 RCS of a metallic square plate for HH polarization

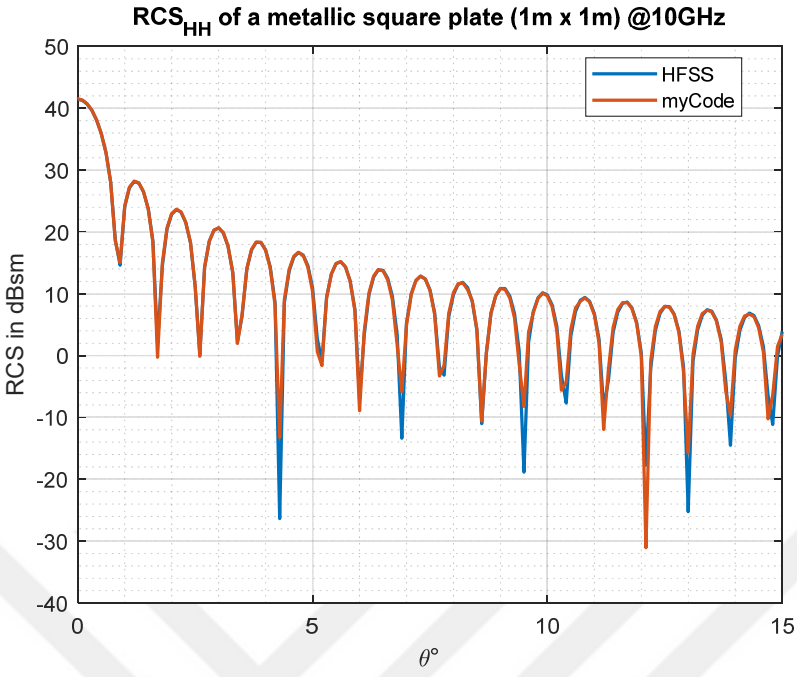

Figure 4.16 RCS of a metallic square plate for HH polarization (zoomed in)

The RCS patterns of the HFSS SBR solver (blue lines) and the developed SBR code (red lines) are almost the same as shown in Figure 4.15 and Figure 4.16. There is a slight shortage of the results of the developed SBR code at oblique incidences. The average RCS results show that this shortage is ignorable. The average RCS value for the HFSS SBR solver is 19.99 dBsm. For the developed SBR code, this value is slightly higher, 20.04 dBsm.

The previous comments for the HH polarization case are valid for the VV polarization case because there is no difference between the results (see Figure 4.17, Figure 4.18) since it is a perfectly symmetric square plate.

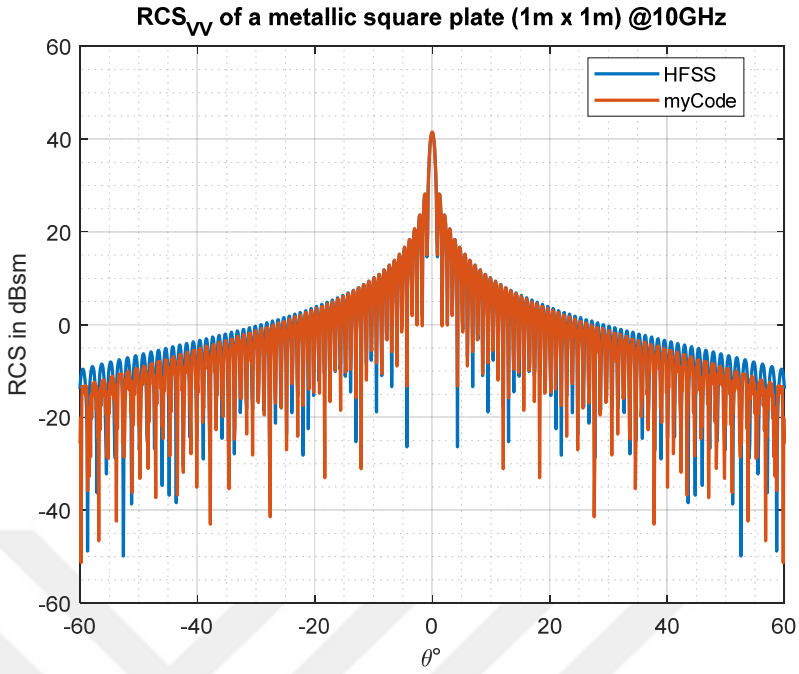

Figure 4.17 RCS of a metallic square plate for VV polarization

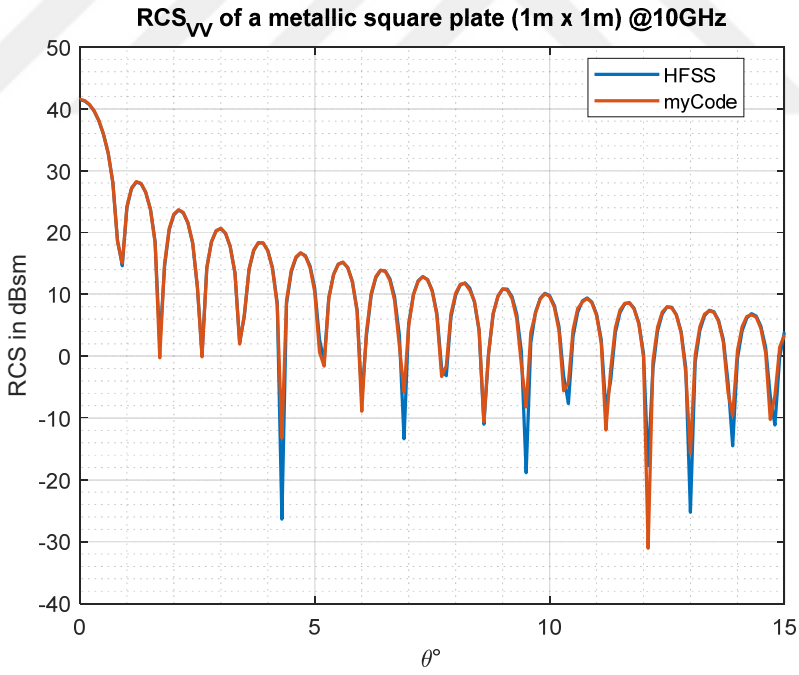

Figure 4.18 RCS of a metallic square plate for VV polarization (zoomed in)

4.4.1.2 Coated Case

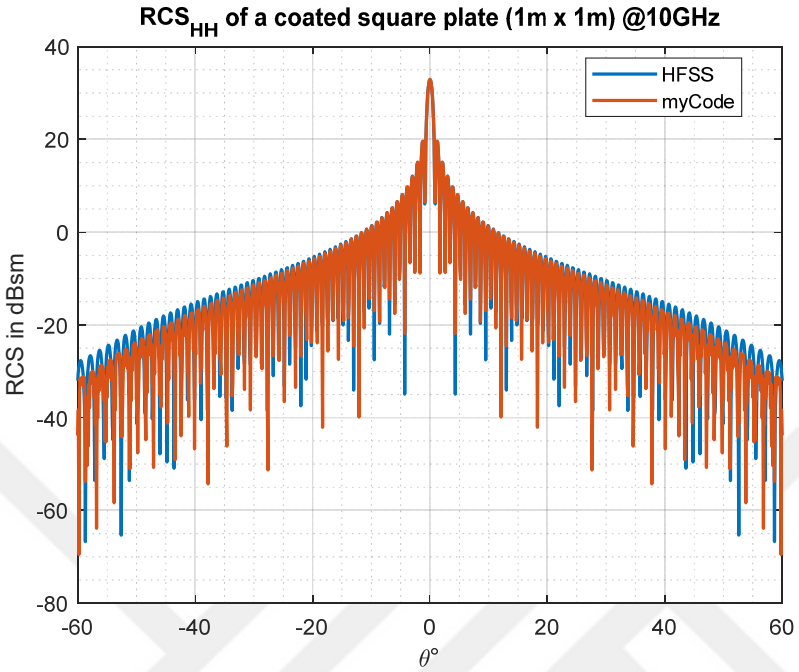

Figure 4.19 RCS of a coated square plate for HH polarization

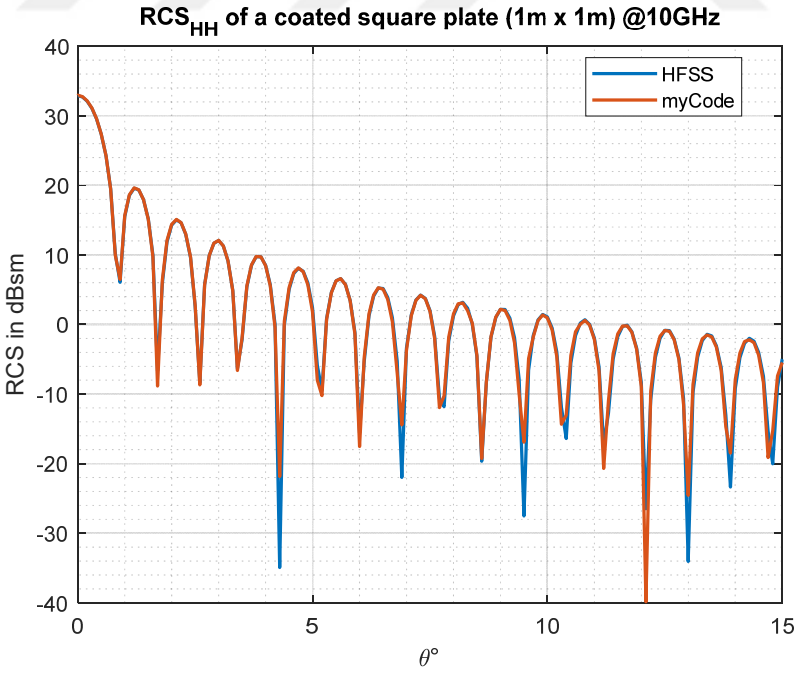

Figure 4.20 RCS of a coated square plate for HH polarization (zoomed in)

The peak level of the main spike is decreased by around 9 dBsm compared to the PEC case, as seen in Figure 4.19 and Figure 4.20. This gap is increased to 20 dBsm levels at oblique incidences since the absorption performance of the coating has a peak around 60° incidence angle for HH polarization, as shown in Figure 2.9 and Figure 2.10. The patterns of the HFSS SBR solver and the developed SBR code have similar characteristics as in the PEC case.

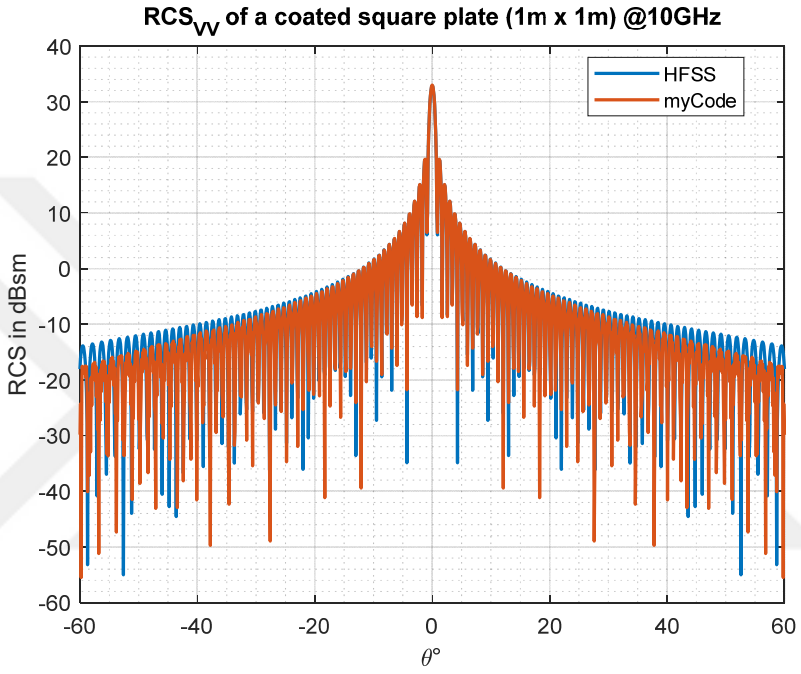

Figure 4.21 RCS of a coated square plate for VV polarization

The peak level of the main spike is decreased by around 9 dBsm compared to the PEC case (see Figure 4.21, Figure 4.22) as in the coated case with HH polarization. The RCS levels at oblique incidences are higher than in the case of HH polarization as expected since the coating material has a better performance at HH polarization. The patterns of the HFSS SBR solver and the developed SBR code have similar characteristics as in the previous PEC and coated square plate cases.

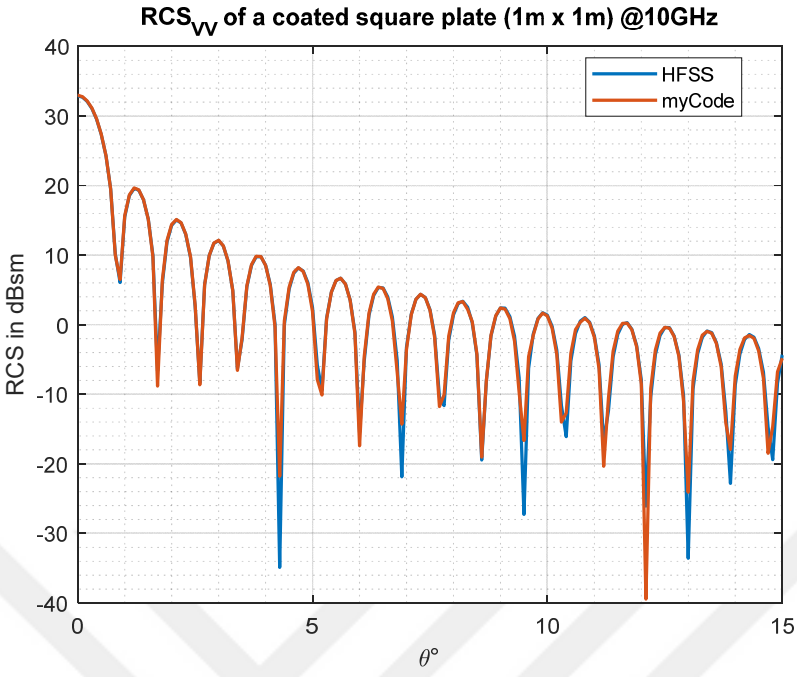

Figure 4.22 RCS of a coated square plate for VV polarization (zoomed in)

Table 5 Average RCS values in dBsm of different cases for a square plate

	VV		HH	
Case	**HFSS**	**Developed SBR Code**	**HFSS**	**Developed SBR Code**
PEC	**20.46**	**20.52**	**20.46**	**20.52**
Coated	**11.91**	**11.97**	**11.90**	**11.94**

The average RCS results given in Table 5 show that the differences between two solvers, HFSS SBR solver and developed SBR solver, are around 1% level which is considered ignorable. The results prove that the PO implementation of the developed SBR solver works well in terms of accuracy.

The main difference between SBR from the PO is the multi-reflections. In the PO method, only the directly illuminated faces of the targets are considered scatterers. On the other hand, the primary advantage of the SBR method is that SBR takes into account the RCS contribution of shadowed faces by including multi-reflection effects. This main difference cannot be understood by comparing the results of the

square plate model, which has only one reflection from its surface. In the next section, the dihedral corner reflector model is used to validate the SBR accuracy performance of the developed SBR solver.

4.4.2 Dihedral Corner Reflector

The second model is a dihedral corner reflector which consists of two perpendicular square plates with 1-meter width and height. In this case, the results show the performance of the SBR code for multi-reflection since there exists more than one reflection from the target. The test model is illustrated in Figure 4.23. The analyses are performed on angular scans from 0° to 90° azimuth as in Figure 4.24.

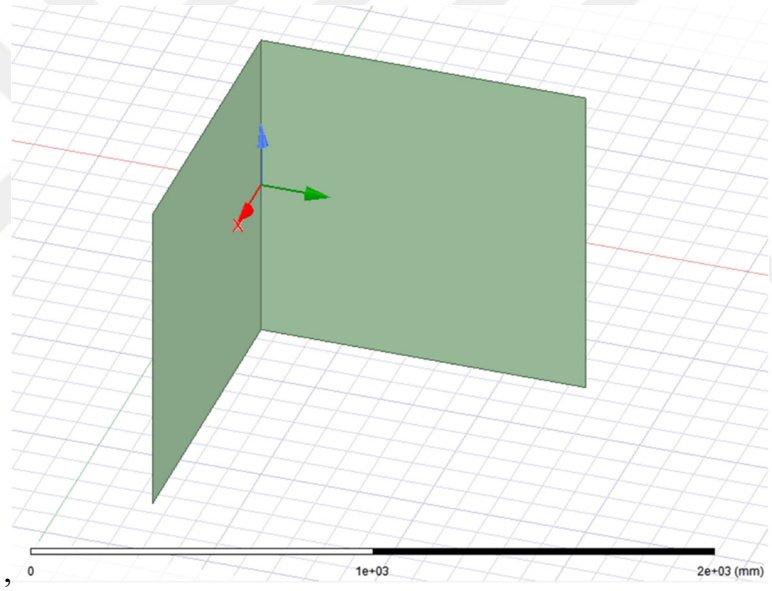

Figure 4.23 Dihedral Corner Reflector

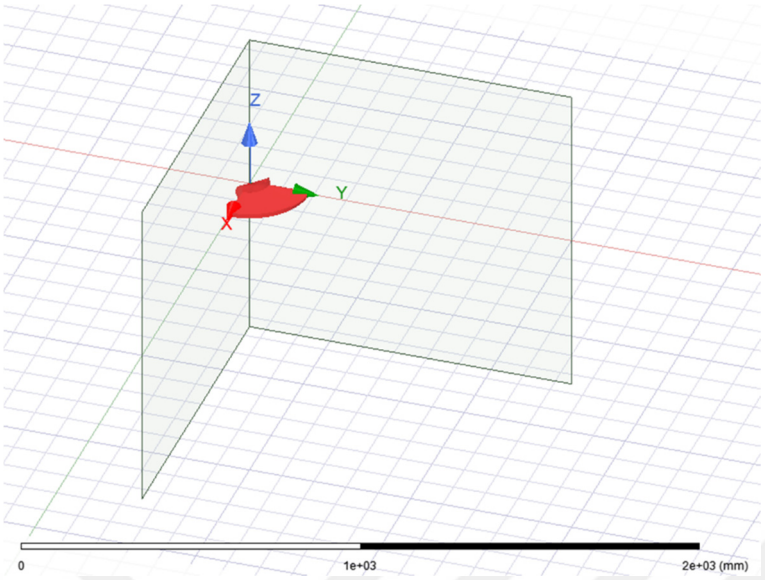

Figure 4.24 Angular scan on dihedral corner reflector

4.4.2.1 PEC Case

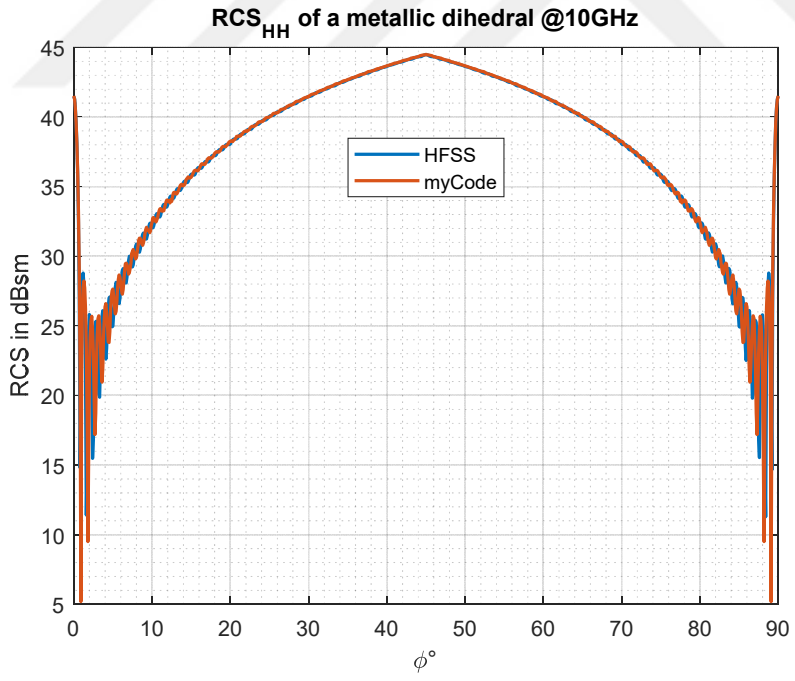

Figure 4.25 RCS of a metallic dihedral corner reflector for HH polarization

In Figure 4.25, the pattern characteristics are pretty similar for HFSS and developed solvers. The values of 0° and 90° are the same value of the square plate from the specular view since only one dihedral surface is illuminated at that angles. The average RCS values are 40.13 dBsm and 40.16 dBsm for HFSS and developed SBR cases, respectively. The ignorable difference in these average RCS values is observed in the zoomed version of RCS patterns; the developed SBR plot is slightly above the HFSS SBR plot. The possible reasons could be the numbers or sizes of the meshes, the refinements in the SBR algorithm that is used by the HFSS SBR solver, etc.

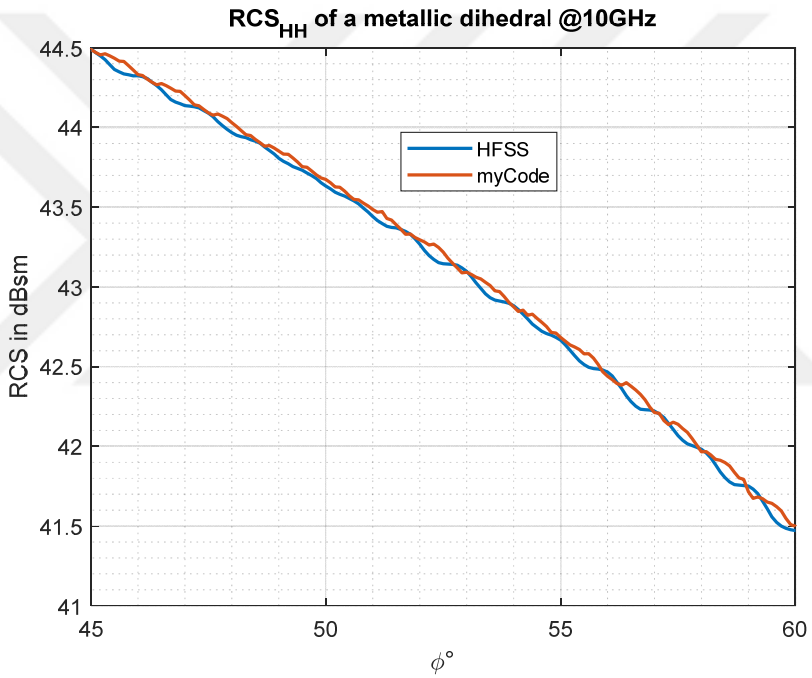

Figure 4.26 RCS of a metallic dihedral corner reflector for HH polarization (zoomed in)

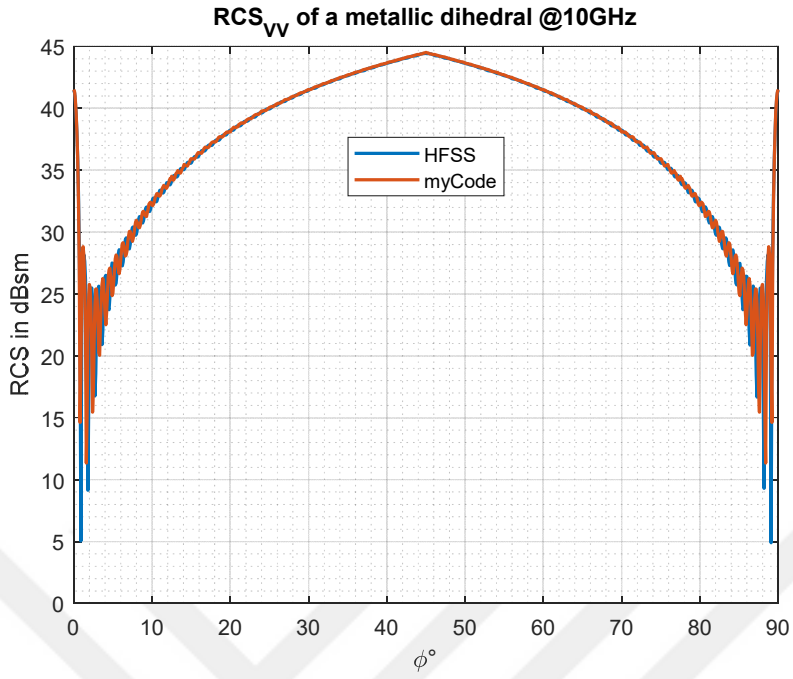

Figure 4.27 RCS of a metallic dihedral corner reflector for VV polarization

In the vertical polarization case, given in Figure 4.27, the average RCS values for the PEC case are almost equal to the values found in the horizontal polarization case: 40.13 dBsm and 40.17 dBsm for HFSS and developed SBR solvers, respectively. This difference is also seen in Figure 4.28, zoomed version of the previous figure. The plots are almost overlapped, and the possible reasons behind the differences are the same as in the previous case of VV polarization.

For PEC cases, the patterns are quite similar for both polarizations and for both solvers (HFSS SBR solver and the developed SBR code), as shown in Figure 4.25, Figure 4.26, Figure 4.27, and Figure 4.28.

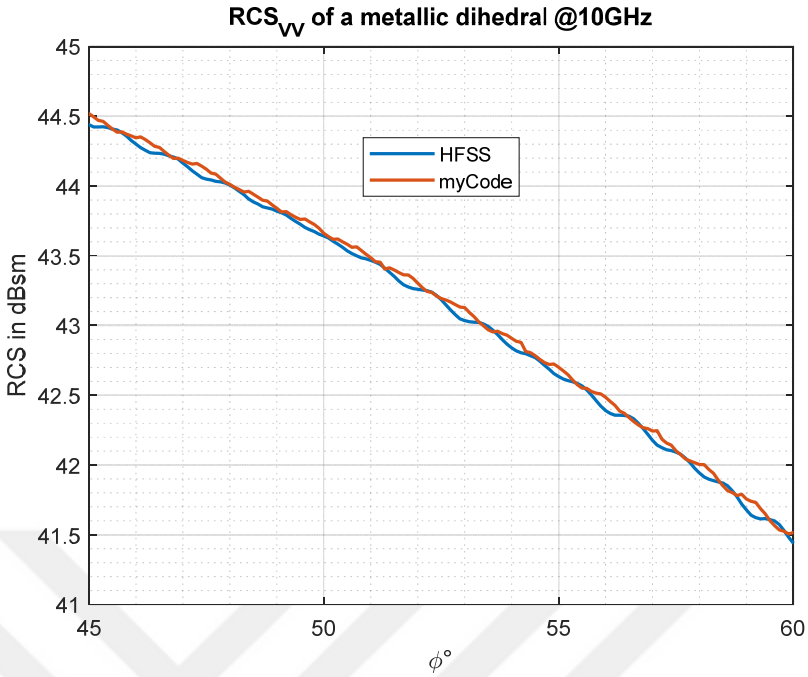

Figure 4.28 RCS of a metallic dihedral corner reflector for VV polarization (zoomed in)

4.4.2.2 Coated Case

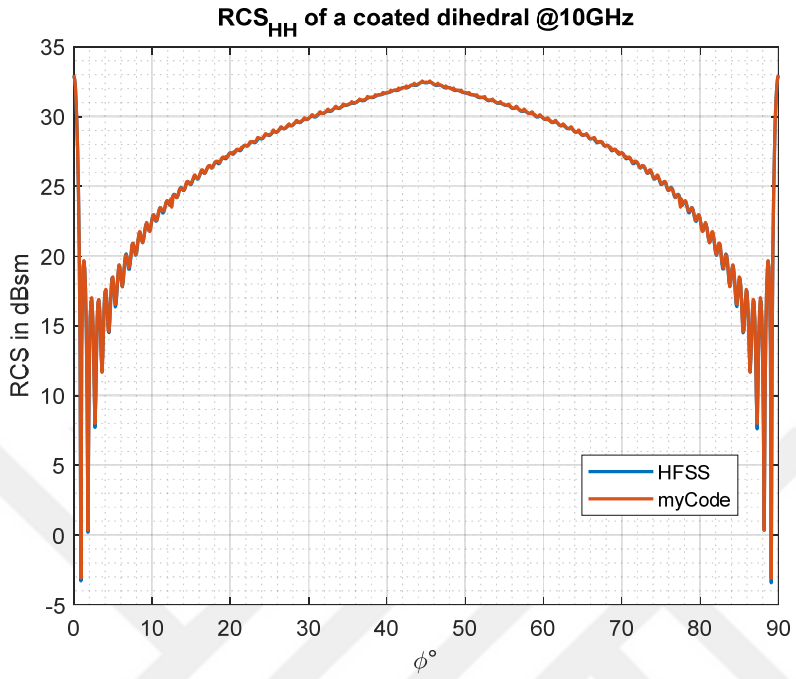

Figure 4.29 RCS of a coated dihedral corner reflector for HH polarization

The patterns of HFSS SBR solver and developed SBR code for HH polarization of coated case, shown in Figure 4.29, are overlapping as in the PEC cases given in the previous section. The average RCS values for HH polarization are 28.62 dBsm and 28.65 dBsm for HFSS and developed SBR solvers, respectively.

The slight surplus in the average RCS value of the developed SBR code for HH polarization is at an ignorable level. Even in the detailed plot, Figure 4.30, the graphs are similar, with 0.1 dBsm notches at half degrees.

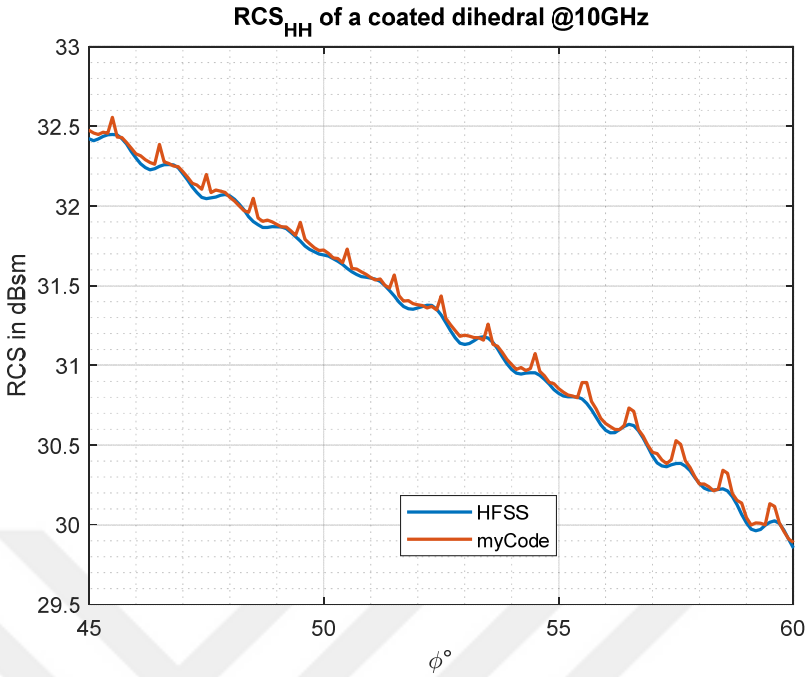

Figure 4.30 RCS of a coated dihedral corner reflector for HH polarization (zoomed in)

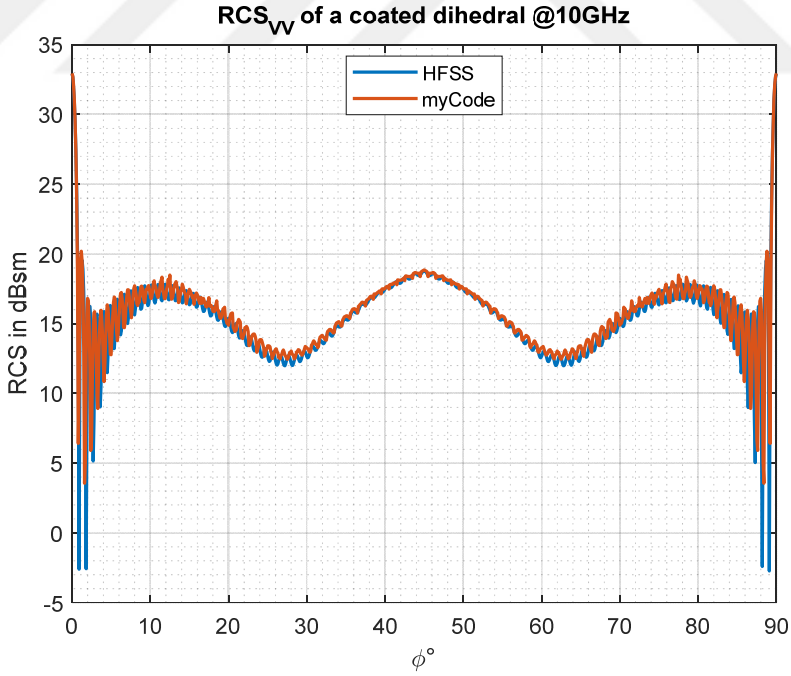

Figure 4.31 RCS of a coated dihedral corner reflector for VV polarization

The difference between HFSS SBR solver and developed SBR solver results are more distinguishable in the vertical polarization plot, in Figure 4.31, than in the previous cases. This situation is also observed in the average RCS values. The average RCS values for HFSS and developed SBR code cases are 17.51 dBsm and 17.66 dBsm, respectively. This difference is observed in the zoomed-in plot given in Figure 4.32.

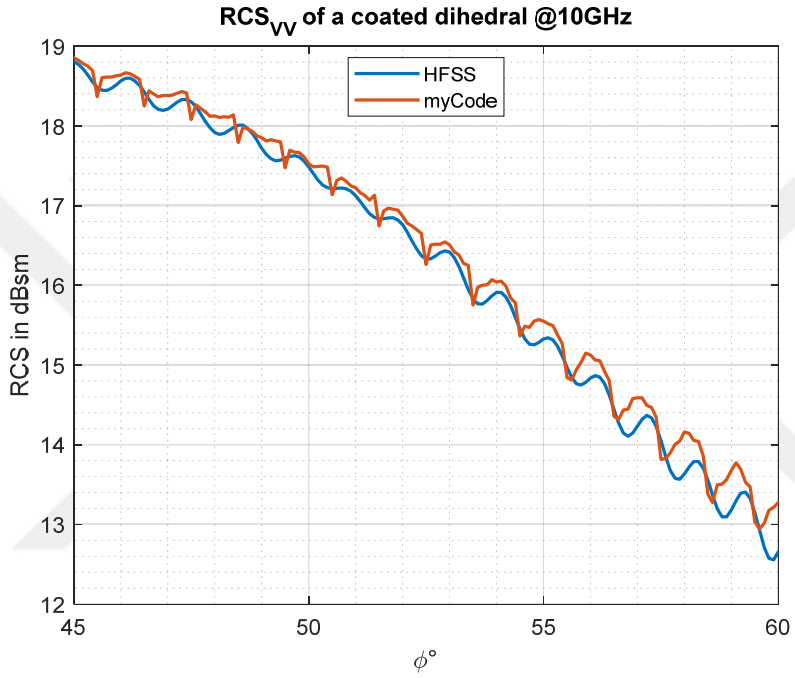

Figure 4.32 RCS of a coated dihedral corner reflector for VV polarization (zoomed in)

Table 6 Average RCS values in dBsm of different cases for dihedral corner reflector

	VV		HH	
Case	**HFSS SBR**	**Developed SBR Code**	**HFSS SBR**	**Developed SBR Code**
PEC	**40.13**	**40.17**	**40.13**	**40.16**
Coated	**17.51**	**17.66**	**28.62**	**28.65**

The overall results are given in Table 6 to compare the average RCS values for HFSS SBR solver and developed SBR solver. According to the given values in the table,

the values are close to each other for both solvers. Almost in all cases, the differences are less than 1%. In the coated cases, the difference for VV polarization is around 3.4%. These levels are ignorable, and they show that the developed SBR solver provides acceptable performance in terms of the accuracy of the RCS values.

CHAPTER 5

COMPARATIVE ANALYSIS OF DIFFERENT CYLINDRICAL CAVITY MODELS

In this chapter, cylindrical cavities are investigated and compared in terms of low RCS properties. Cavity models are generated parametrically with the help of a CAD tool called CATIA. These models are analyzed by using the ray-tracing tool developed for this work. The statistical outputs of the ray-tracing analysis are used to optimize the cavity geometries for maximizing the minimum reflection number and optimize the RAM for the most observed reflection angle. In addition, RCS analyses of those models are performed by the developed SBR tool. For each iteration, results are shared and investigated.

The frequency for this study is selected as the center frequency of X-Band, 10 GHz, since it is one of the most critical frequency bands in the military, especially for electronic warfare. Missile guidance and short-range tracking are operated at that frequency band. Low observability at X-Band is very crucial from an operational point of view.

The length and diameter of the cavities are determined as electrically 200λ and 30λ at 10 GHz, respectively. These values, physically 600 cm and 90 cm, are typical values for fighter aircraft duct length and the diameter of the engine belonging to those aircraft, respectively.

The engine interface is shown in Figure 5.1. There are stators and rotating blades of the engine at the end of the duct. In this study, these details are not included. The duct-engine interface is modeled with a representative planar circular plate as in Figure 5.2. With the help of this plate, the rays bounce back and contribute to the monostatic RCS of the cavity models used in the study, similar to the real case for the aircraft.

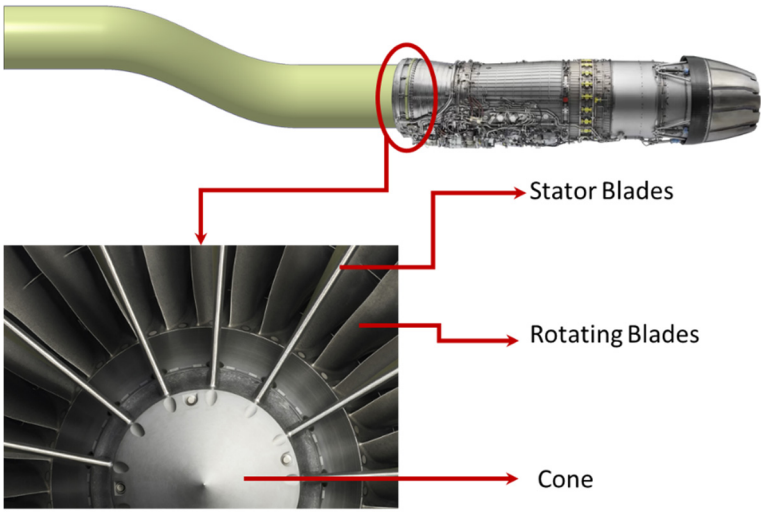

Figure 5.1 Engine Interface with details of blades



Figure 5.2 Representative planar circular plate

The ray approximation is valid for high frequencies where the objects have electrically large sizes. The electrical lengths of the cavities are around 20λ-40λ for L-Band. However, in this specific cavity case, the dimension of the cavity entrance is also important as the length of the cavity. In this manner, the statistics for these models cannot be used for the frequencies from L-Band, 1-2 GHz values, since the cavity entrance becomes 3λ-6λ at those frequencies, which are not considered electrically large sizes. The results of X-Band analyses are meaningful for frequencies at C-Band, 4-8 GHz values because, at that interval, even the electrical size of the entrance of the cavities is approximately 12λ - 24λ, which can be considered electrically large. For the upper limit of frequency, the convergence tests

can be taken as references. If the results provided in the previous chapter are satisfying, then these results can also be used for Ku-Band, up to 18 GHz, or higher bands.

The azimuth range is determined as from 0° to 30°; the elevation range is selected as from 75° to 105° (in Figure 5.3) with an angular resolution of 1° for both. These angles define a generic forward sector for fighter (A-A) or bomber (A-S) aircraft.

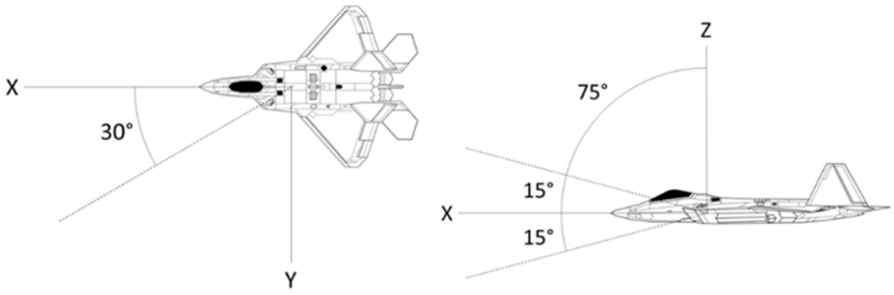

Figure 5.3 Angular intervals on azimuth (left) and elevation (right)

In the analysis, only one duct is analyzed. The LHS duct is selected as the reference (in Figure 5.4). As a result of this situation, the interval on the azimuth plane is selected from 0° (head-on) to 30°, not from -30° to 30°.

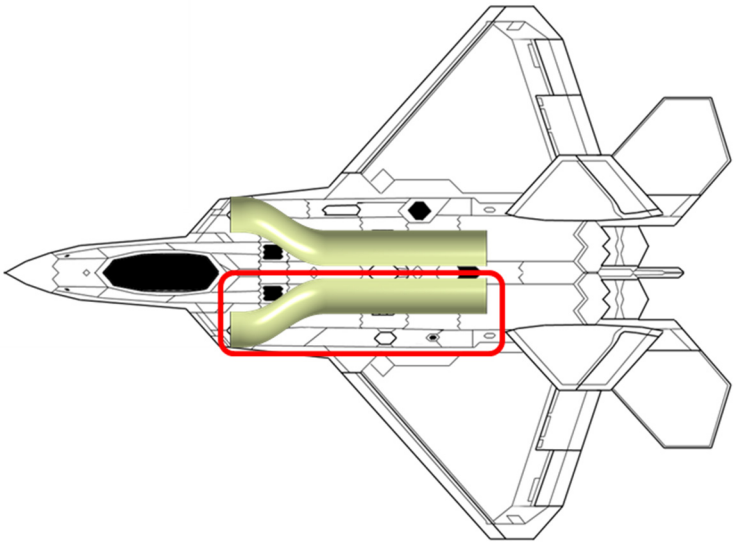

,

Figure 5.4 The representation of the LHS duct on an aircraft model (in red borders)

5.1 Straight Cylindrical Cavity

The first cavity model used in the analyses is chosen as a straight cylindrical cavity and named Model_01. In the first step, Model_01 is drawn in CATIA. The mesh and CAD models are shown in Figure 5.5 and Figure 5.6, respectively.

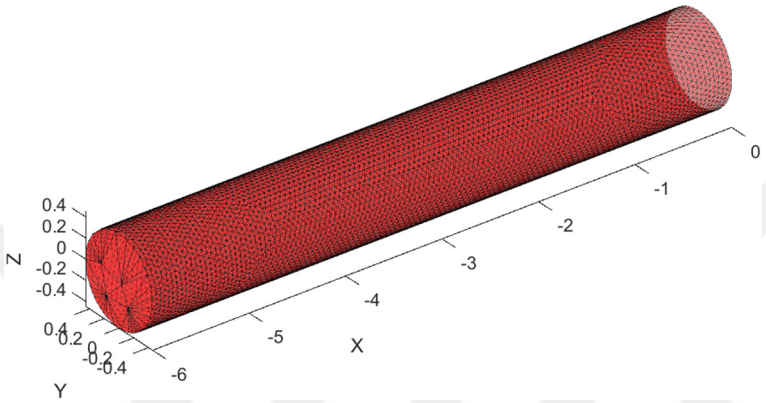

Figure 5.5 Mesh of Model_01

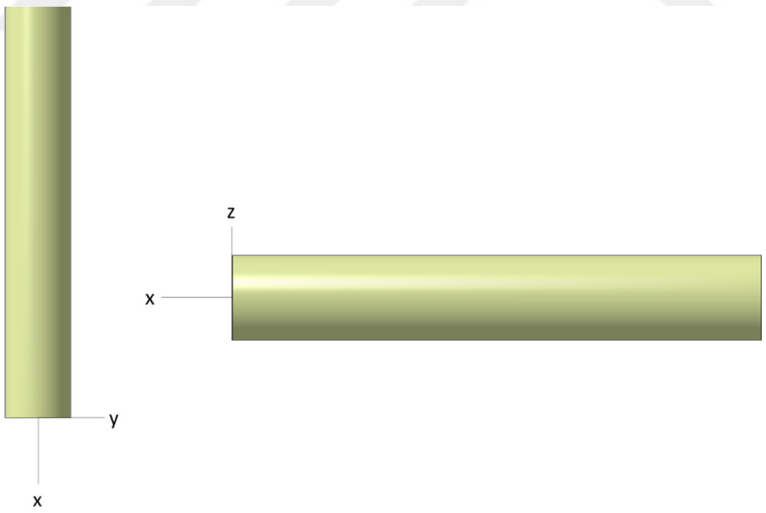

Figure 5.6 CAD model of Model_01 from the top (left) and right (right) views

First, ray-tracing analysis is performed to determine the angular distribution of the rays on the model. 2D and 3D angular distributions of the rays for Model_01 are illustrated in Figure 5.7 and Figure 5.8, respectively. The x-axis of Figure 5.7 is the

reflection angle from 0° to 90°. All the reflections from all the rays are taken into account to generate this plot. The numbers of reflections at given angles are shown on the y-axis. There are two maxima points in the graph of 2D angular distributions. One of them, which is at 15°, belongs to the rear face of the cavity. The second maxima at 75° belongs to the duct surfaces. These results show that the engine face shall be coated with RAM optimized for 15° incident angle, and the duct surfaces shall be coated with RAM optimized at 75° incident angle.

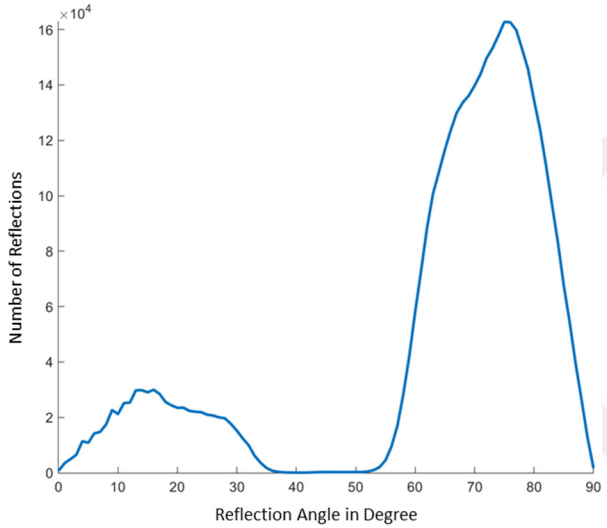

Figure 5.7 2D angular distribution of the rays on Model_01

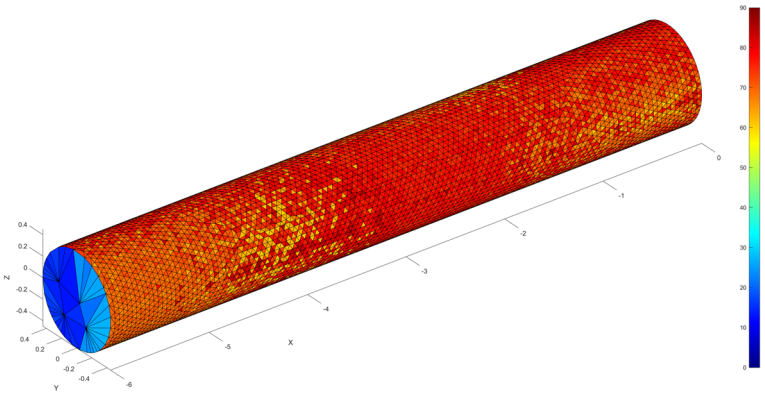

Figure 5.8 3D angular distribution of rays on Model_01

The RCS graphs of Model_01 are shown in Figure 5.9. The RCS results are presented in the logarithmic (dB) scale. The peak RCS value is 37.52 dB at (0°, 90°) azimuth

and elevation angular pair. This value makes 5600 m^2 in linear scale, which is not acceptable for a stealth aircraft. A generic stealth aircraft have a 0.005 m^2 average RCS, which is around -23 dB, as shown in Figure 5.10 [19]. This level of RCS cannot be reduced to a reasonable level by using RAM coating. The model should be redesigned. However, the RCS analyses of coated Model_01 are undertaken, and the results are shown in the following sections.

One of the critical issues about the RCS graphs is the difference in the scales of PEC and coated cases. The limits are shown in all graphs. Briefly, the limits are from -10 dBsm minimum to 30 dBsm maximum for straight cylinder PEC cases; the limits are from -10 dBsm minimum to 20 dBsm maximum for other PEC cases. In the situations of the coated cases, the minimum limit is selected as -40 dBsm, the maximum limit is chosen as 10 dBsm for straight cylinder, and the minimum limit is selected as -40 dBsm, the maximum limit is chosen as -10 dBsm for other cavities.

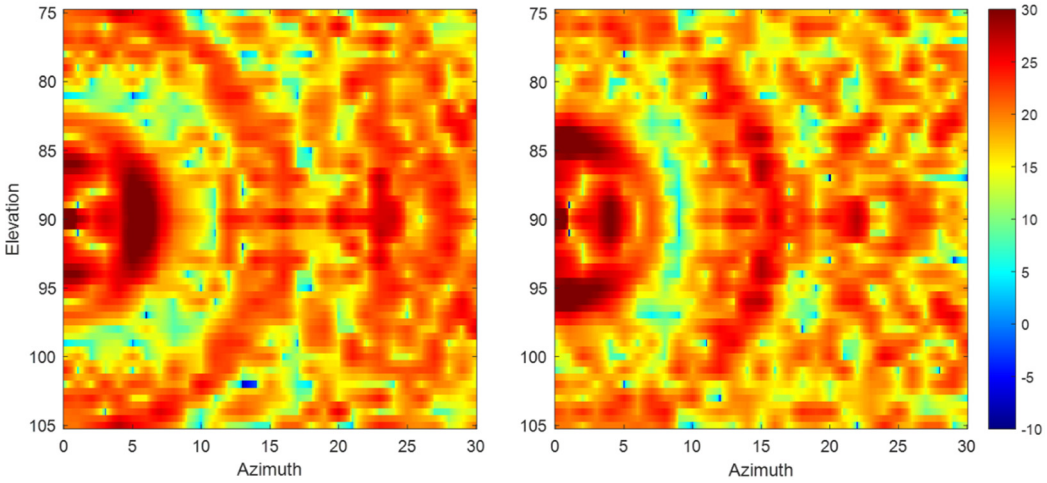

Figure 5.9 RCS graphs of Model_01 for VV (left) and HH (right) polarizations

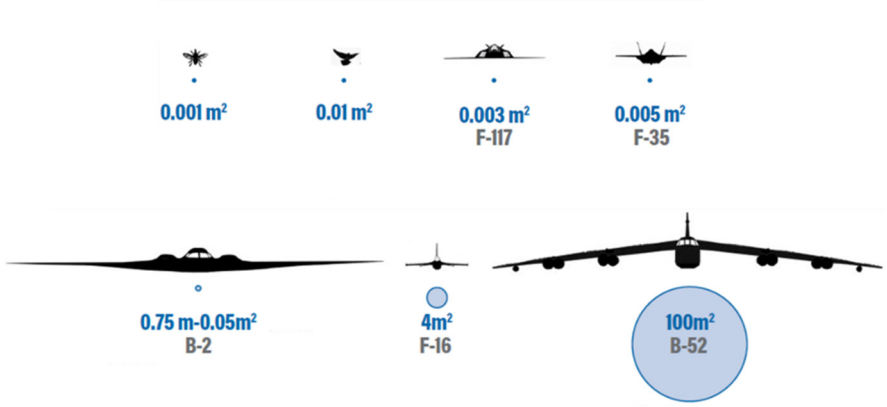

Figure 5.10 RCS comparison of insect, bird, and air platforms

The peak point is the point in which the back face is directly illuminated. The RCS value at that point is almost at the same level of the RCS of a flat plate. The key point to reducing the RCS is to hide the back face. In Model_01, the minimum bounce number is only 1. The minimum bounce number shall be increased by hiding the rear face.

5.2 Bended Cavity

Model_02 is a cylindrical cavity with a bent in the middle position. An offset in y-direction results in a bent on the model. The top and right side views are shown in Figure 5.11.

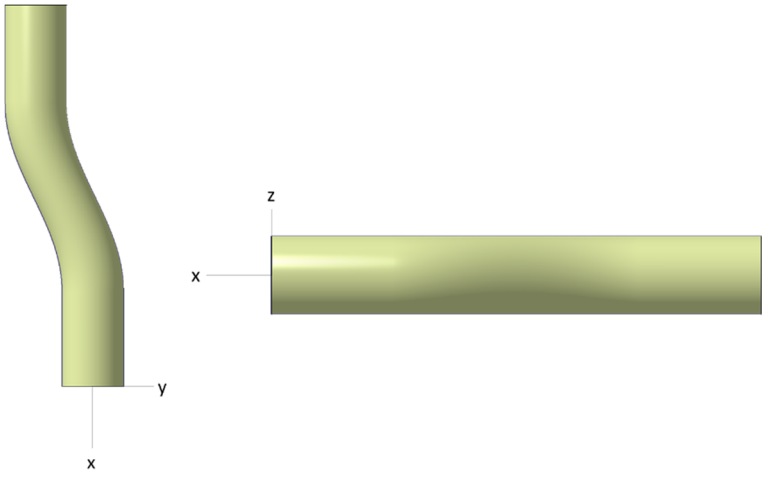

Figure 5.11 Top (left) and right side (right) views of Model_02

The bent slope could be defined as the ratio of offset in the y-direction and the length of the bent region. In this case, the slope is 0.3 as the ratio of 30λ to 100λ for Model_02. The rear face is not seen from the head-on angle, as in Figure 5.12. However, with a slight turn, the back face is seen, as in Figure 5.13.

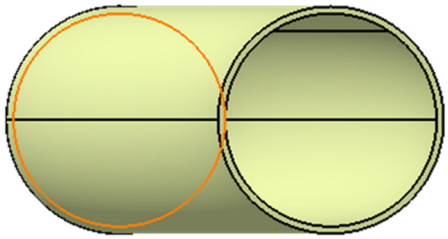

Figure 5.12 Shadowed rear face of Model_02 at the head-on angle (0° azimuth and 90° elevation)

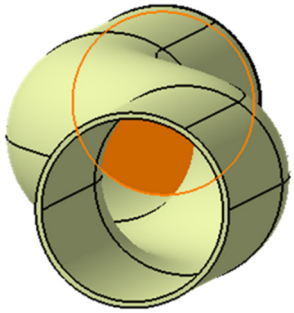

Figure 5.13 Rear face of Model_02 is seen at 10° azimuth and 85° elevation

The ray-tracing analysis is performed as the first step. Unlike the Model_01, Model_02 has a single maxima point in the 2D angular distribution plot in Figure 5.14. The first maxima point of Model_01 is almost lost, and the second maxima point is slightly shifted to a lower angle. The minimum bounce number is increased to 2, but it is still deficient. Hiding the rear face from head-on illumination is the critical point in increasing the minimum bounce number.

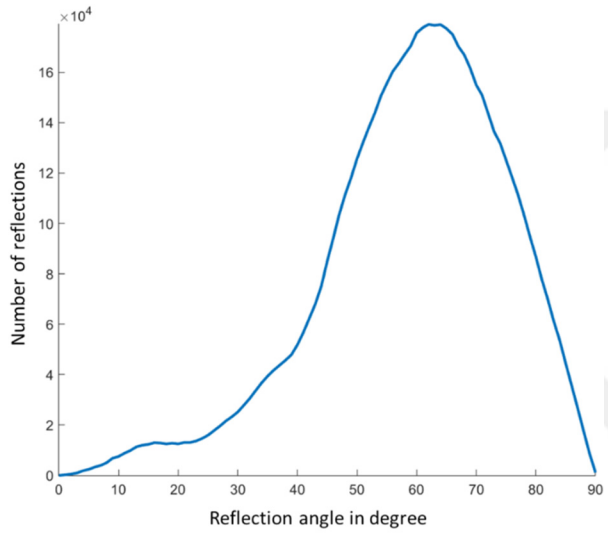

Figure 5.14 2D angular distribution of rays on Model_02

3D angular distribution of Model_02 is shown in Figure 5.15. As in Model_01, the rays reflected from the back face are almost perpendicular to the surface, and the rays reflected from the duct surfaces have an average reflection angle around 65°. The ray statistics show that the absorbing materials coated on those surfaces shall be optimized for the reflections at 15° and 65°, respectively.

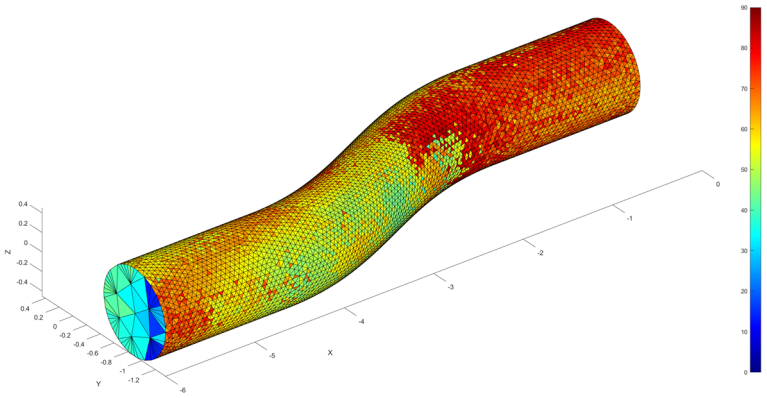

Figure 5.15 3D angular distribution of rays on Model_02

The RCS graphs of Model_02 are shown in Figure 5.16. The maxima point is shifted to the higher azimuth with respect to Model_01's maxima point. When it is compared with Figure 5.9, the average RCS of Model_02 is drastically reduced from 21.19 dB to 10.52 dB for VV polarization and from 21.25 dB to 10.69 dB for HH polarization. The RCS value at the peak point also dropped to 24.17 dB for VV and 23.65 dB for HH polarization. These values are still very high for a stealth air platform. However, two different cases are analyzed to see the effect of absorbing materials: Model_02_RAM and Model_02_optRAM. In the former case, an absorbing material optimized for perpendicular reflections is used. In the latter case, materials optimized for the 3D angular distribution of rays are used.

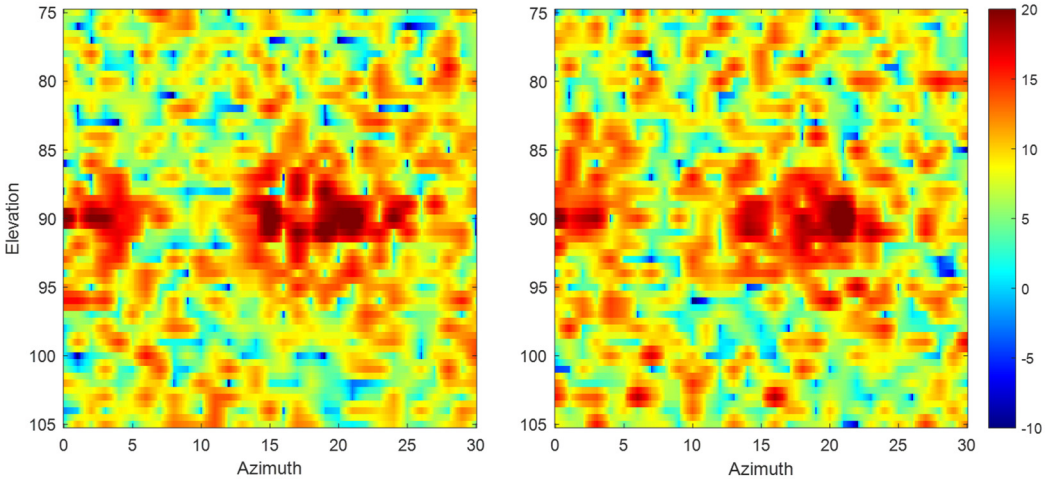

Figure 5.16 RCS graphs of Model_02 for VV (left) and HH (right) polarizations

5.3 Material Optimization Procedure

In this study, Altair FEKO 2020 electromagnetic solver is used to optimize absorbing materials for specific incidence angles [15]. As a beginning, electromagnetic properties (complex permittivity and permeability values) are required. ARC Technologies provides these values for their commercial products. Technical Data Sheets [20] of the materials used in this study are given in the Appendix section. Since the frequency has been selected as the center frequency of X-Band, 10 GHz, complex permittivity and permeability values only at 10 GHz are adequate in the optimization process.

In the CADFEKO module of FEKO, a new model is created. On the "Construction" tab, under the "Structures" section, "Planar multilayer substrate" should be constructed by clicking "Plane/Ground", as in Figure 5.17. The dielectric medium should be created by clicking the plus-shaped button on the rightmost position of "Layer 1" row. In the opening box (Figure 5.18), the values taken from ARC Technologies' Technical Data Sheets are entered.

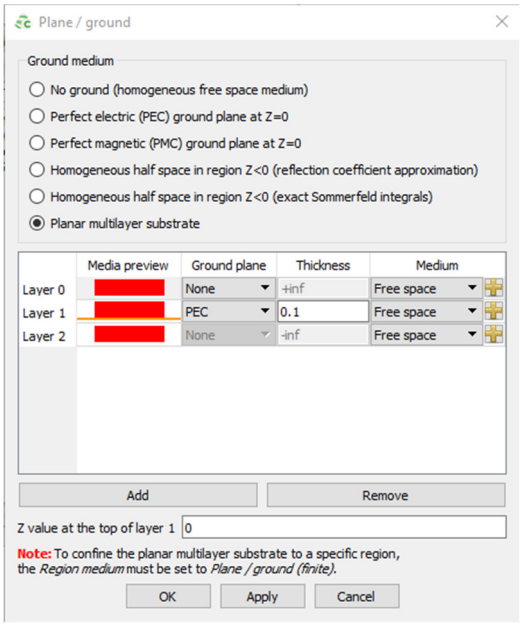

Figure 5.17 FEKO Planar multilayer substrate construction

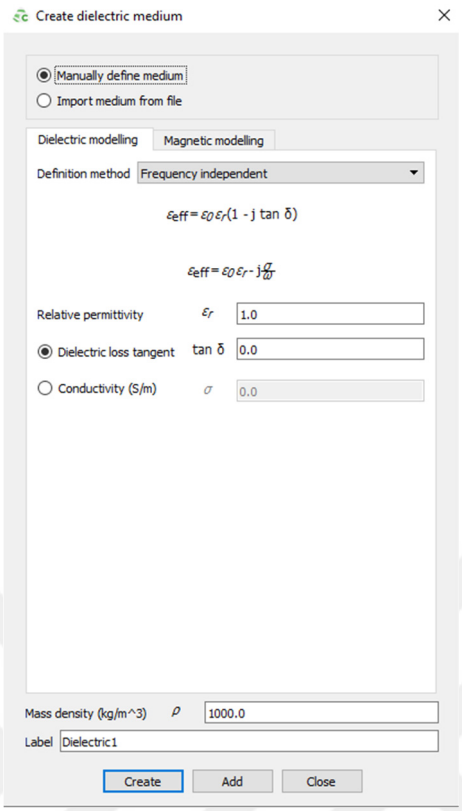

Figure 5.18 FEKO dielectric medium creation

A variable called "t_layer1" is assigned to the thickness value of "Layer 1", with a default value of 1 mm. "Plane wave" from the optimization angle/angles (selected from 0° to 90° elevation angles) is the source for "Transmission/reflection" type of solution request.

In the "Request" tab, "Optimisation" section is used for the material optimization process. The reflection coefficient goal is created as in Figure 5.19. The operations in the figure should be applied to get the results on the dB scale. In the final step, the thickness of the material is defined as a parameter for the optimization process.

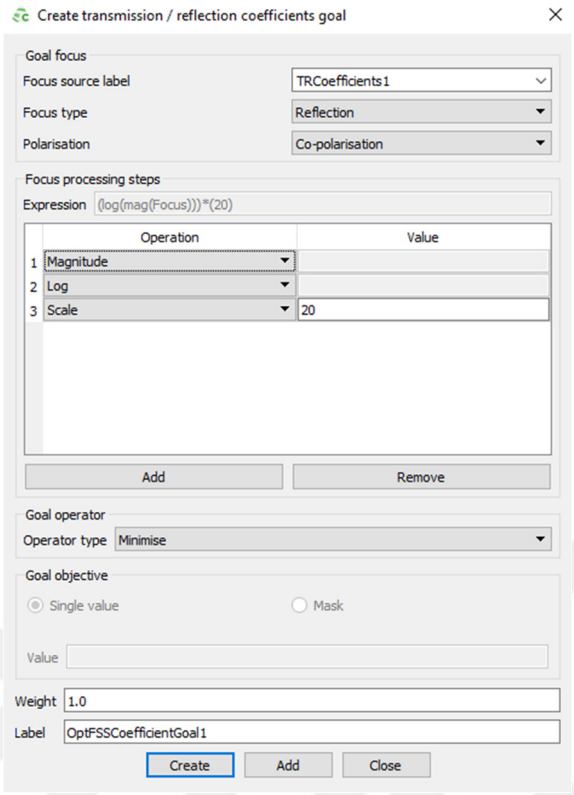

Figure 5.19 FEKO Reflection coefficient goal

In the final step, material thickness is defined as a parameter for the optimization process, shown in Figure 5.20. The minimum and maximum values are selected as 0.5 mm and 2 mm, respectively. The start value is assigned as a default value of the thickness variable, 1 mm.

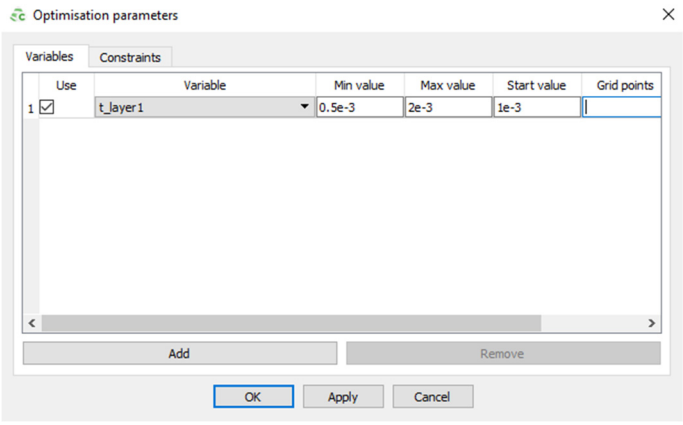

Figure 5.20 FEKO Optimization parameters

During the optimization process, the thickness of the layer is varried to find the minimum reflection coefficient at specified angles. In the case of Model_02, optimization angles are selected from 55° to 70° with 5° resolution. The optimum thickness is found as 0.7 mm (in Figure 5.21). For optimization angles from 55° to 70° with 1° resolution, the process takes longer, but thickness is found at 0.7 mm, again (in Figure 5.22). The change in the thickness during the optimization process can be seen in Figure 5.23.

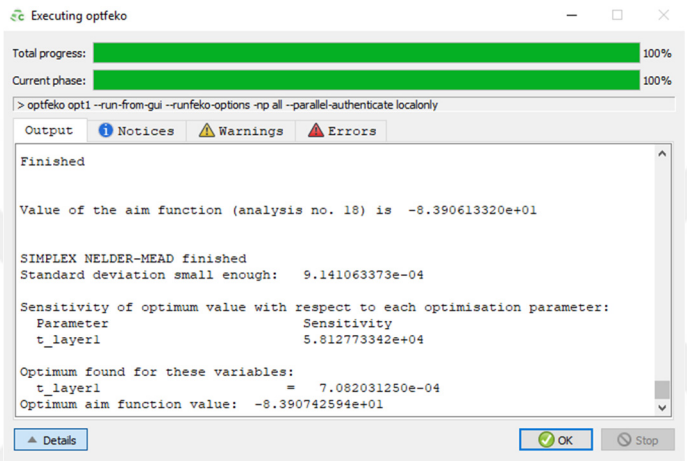

Figure 5.21 FEKO Optimization for Model_02

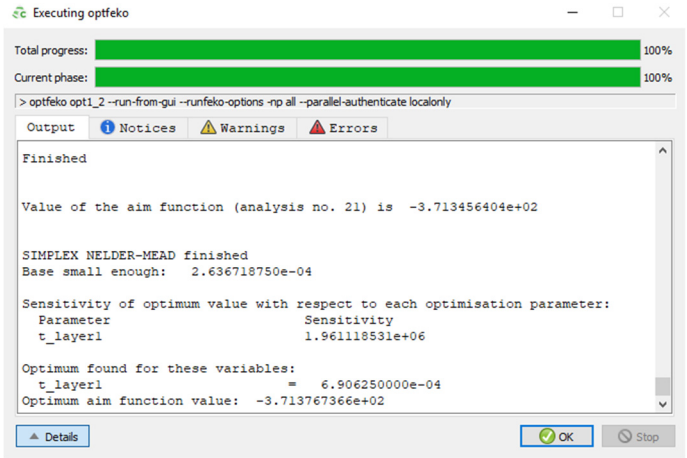

Figure 5.22 FEKO Optimization with higher resolution of optimization angles

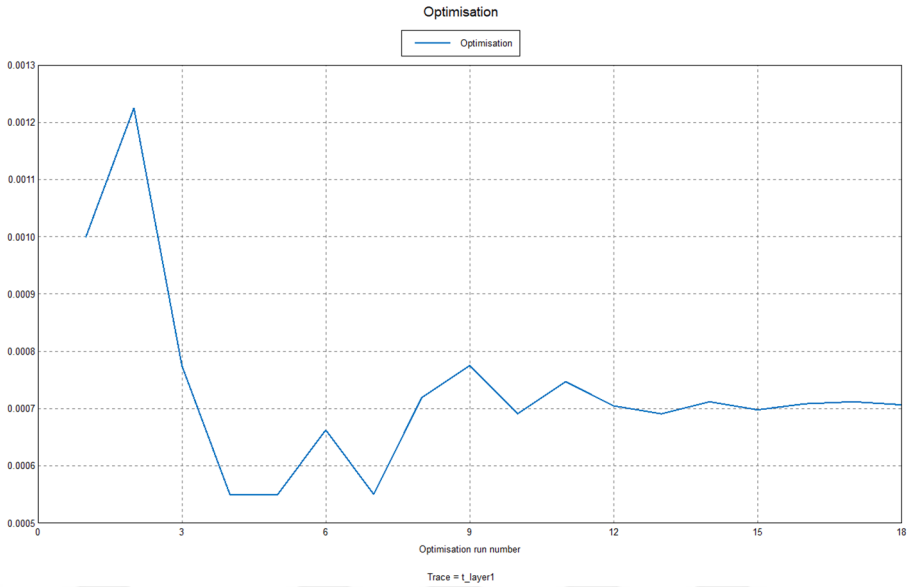

Figure 5.23 Change of "t_layer1" parameter during optimization

5.4 Analysis with Optimized Material

Materials for Model_01_RAM, Model_01_optRAM, Model_02_RAM, and Model_02_optRAM are created using the process defined in Section 5.3. For the Model_01_RAM and Model_02_RAM cases, a material optimized at 0° incidence is used (Figure 5.24). In the other cases, two different materials are developed for 15° and 65° incidences (Figure 5.25 and Figure 5.26, respectively).

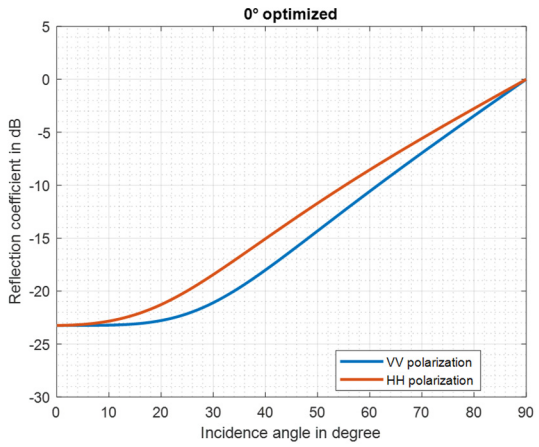

Figure 5.24 Material optimized for 0° incidence (2.05 mm UD-11738)

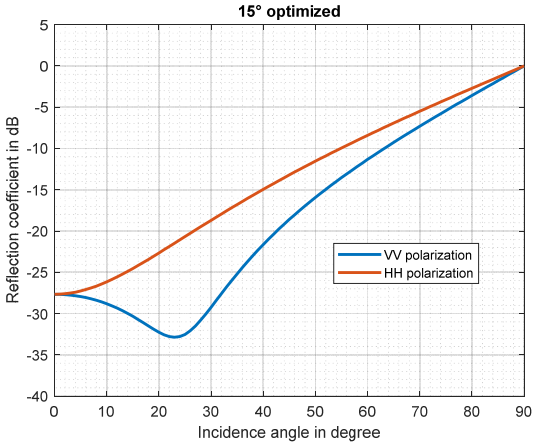

Figure 5.25 Material optimized for 15° incidence (1.9 mm UD-14502)

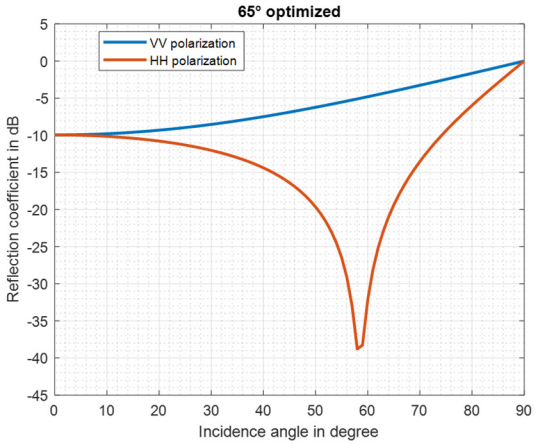

Figure 5.26 Material optimized for 65° incidence (1.52 mm FD-12331)

The exact geometry of Model_01 is used for Model_01_RAM and Model_01_optRAM cases. In the former case, all inner surfaces are coated with a standard absorber optimized for 0° incidence. In the second case, the back face is coated with a material optimized for 15°, and the rest of the inner faces are coated with a material optimized for 65°.

The exact same material application is applied for Model_02 cases. The material applications are shown in Figure 5.27. The material optimized for 15° is illustrated with turquoise, and the material optimized for 65° is illustrated with green colors, as in the right side of the figure.

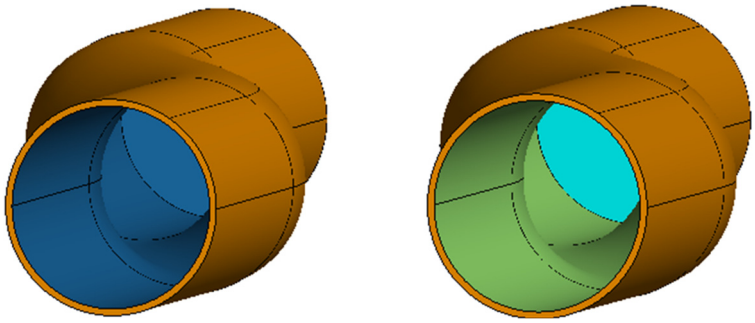

Figure 5.27 Material application for Model_02_RAM (left) and Model_02_optRAM (right)

In the following figures, in Figure 5.28 and Figure 5.29, the 2D RCS graphs are shown for Model_01_RAM and Model_01_optRAM cases. The highest RCS points are located at the head-on position since the plate at the end of the cavity has the highest RCS impact. The peak values drop from 37.52 dB to 14.85 dB even for non-optimized coating cases shown in Figure 5.28. The average RCS values are around -6 dB for both VV and HH polarization.

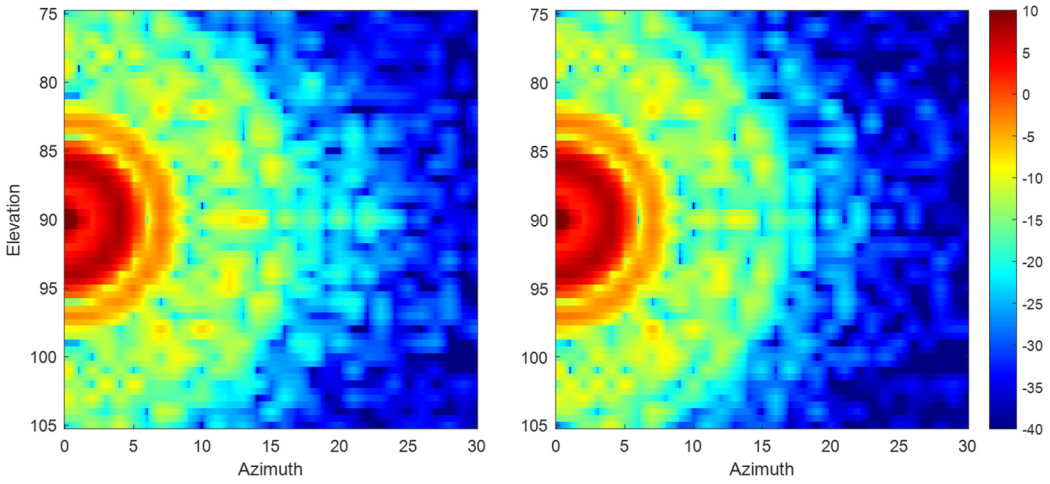

Figure 5.28 RCS graph of Model_01_RAM for VV (left) and HH (right) polarizations

In the optimized coating cases, in Figure 5.29, the peak values are 10.67 dB at the same coordinates in terms of azimuth and elevation pair. The average RCS values are around -10.5 dB for both VV and HH polarization.

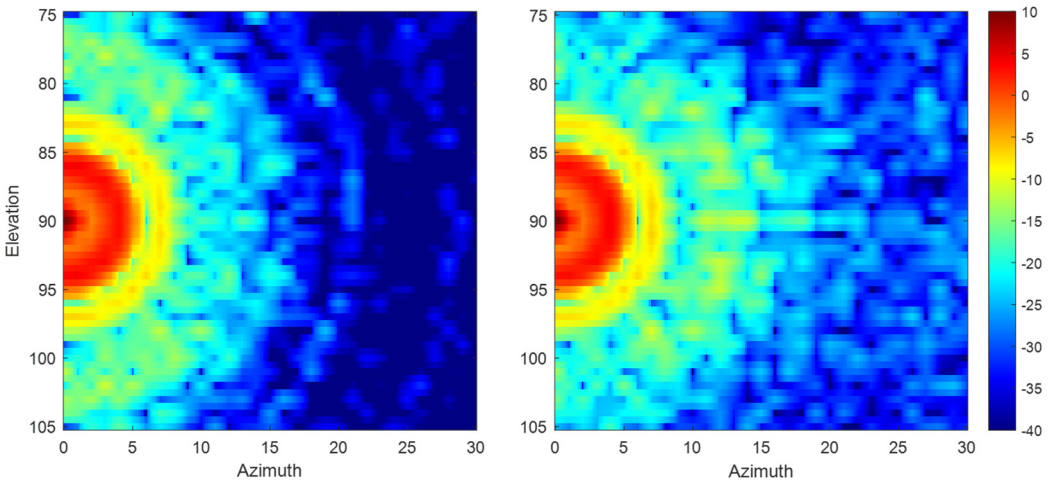

Figure 5.29 RCS graph of Model_01_optRAM for VV (left) and HH (right) polarizations

The RCS graphs of both Model_02_RAM and Model_02_optRAM are illustrated in Figure 5.30 and Figure 5.31. The peak RCS values of the non-optimized coating case are -2.64 dB and -2.43 dB for VV and HH polarization, respectively. In the optimized coating case, these values are -7.40 dB and -5.61 dB for the related polarizations. There is more than 30 dB difference between the peak RCS values of PEC and optimized coating cases, which is a huge difference, around 1000 times in linear scale.

The average RCS values for the non-optimized cases are -21.11 dB and -21.59 dB for VV and HH polarization, respectively. These values drop to -25.76 dB and -24.67 dB for the optimized case of VV and HH polarization, respectively. These values agree with the hypothesis of this study since the RCS values drop with optimized material applications.

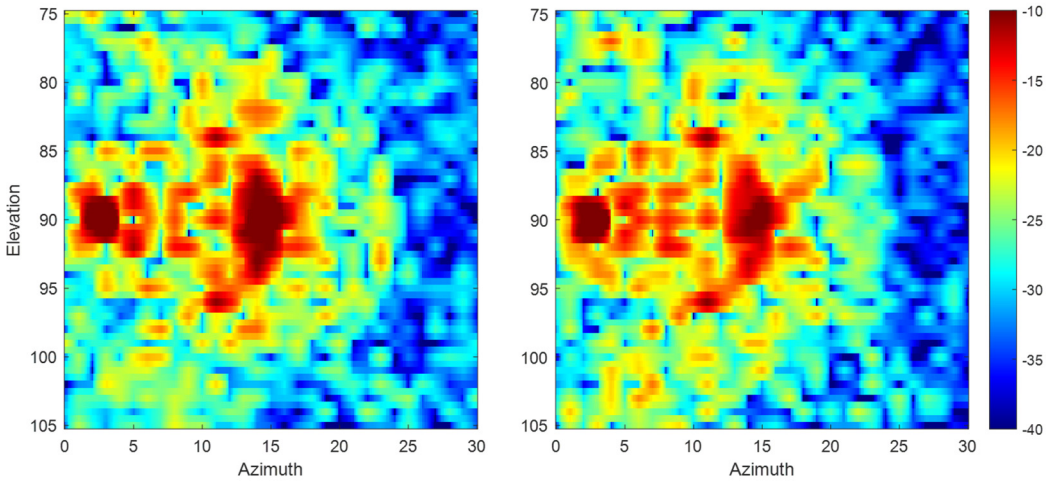

Figure 5.30 RCS graph of Model_02_RAM for VV (left) and HH (right) polarizations

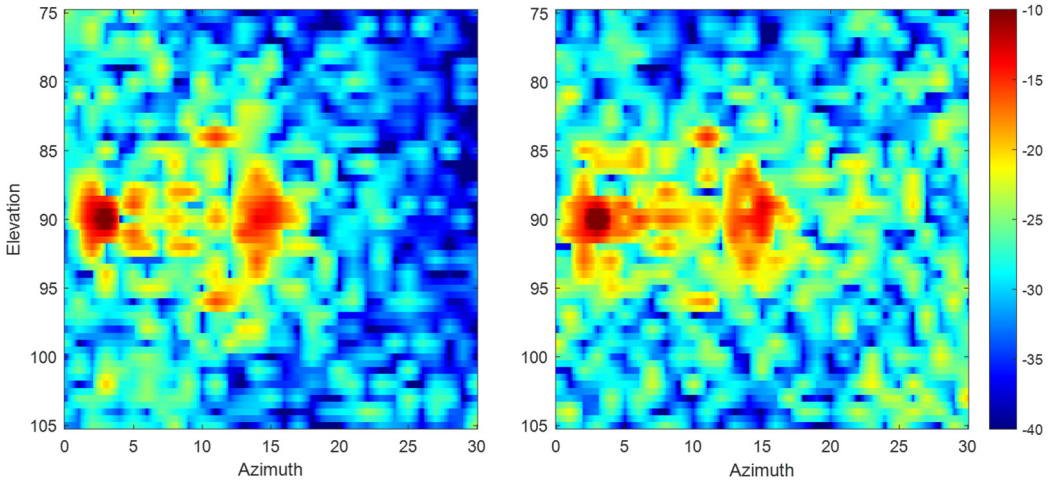

Figure 5.31 RCS graph of Model_02_optRAM for VV (left) and HH (right) polarizations

The first iteration is completed. In the next step, the cavity model will be modified to increase the reflection number. Ray-statistics will be used to find optimum material.

5.5 Bend in z-direction

Model_03 is a modified version of Model_02 with a new bent in the middle position. An additional offset in the z-direction is the difference from Model_02. The top and right side views are shown in Figure 5.32.

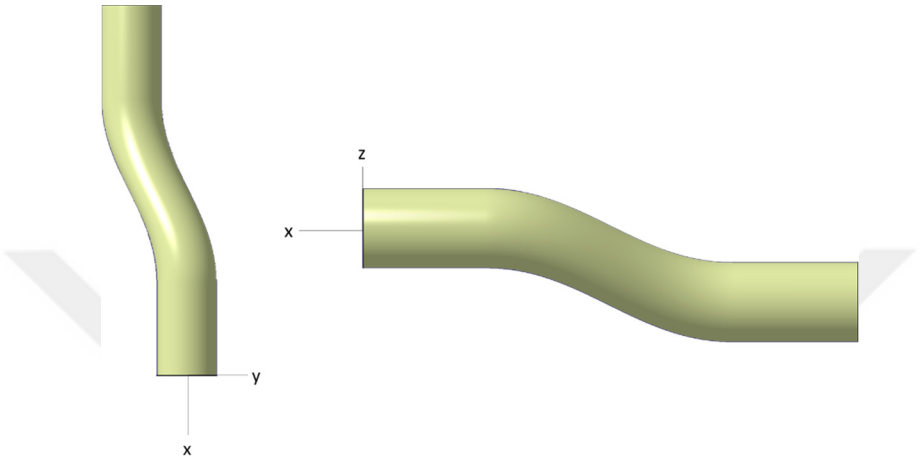

Figure 5.32 Top (left) and right side (right) views of Model_03

The bent slope in the z-direction is also 0.3 (the ratio of 30λ to 100λ). The rear face is not seen from the head-on angle, but with 10° deviation in elevation and a 15° deviation in azimuth makes the rear face visible, as in Figure 5.33.

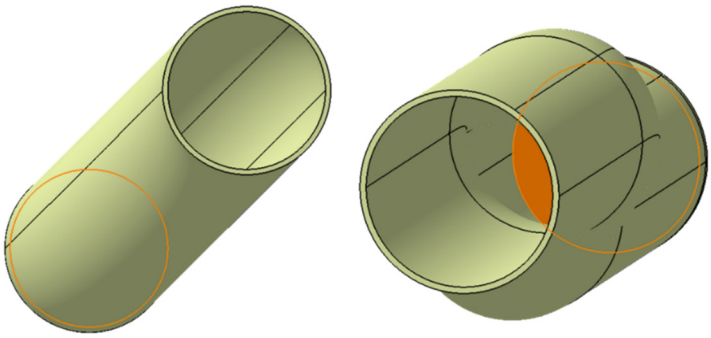

Figure 5.33 Mode_03 from x-direction (left) and 80° elevation 15° azimuth (right)

The RCS graph of the metallic case is shown in Figure 5.34. Even for the PEC case, the large red zones are reduced, and the graph becomes sparser as compared to the one in Figure 5.16 because of the higher obscuration of the rear face.

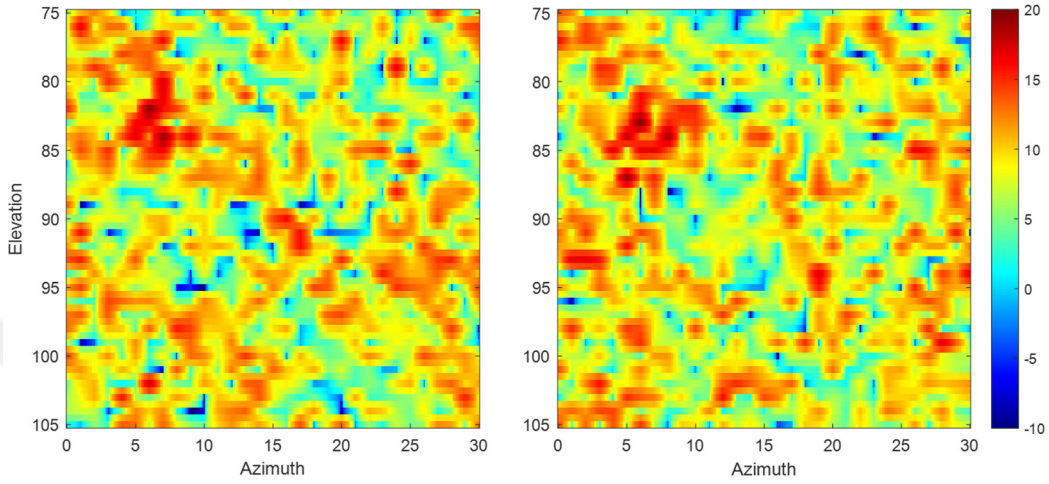

Figure 5.34 RCS graphs of Model_03 for VV (left) and HH (right) polarizations

Ray tracing analysis is performed for Model_03. The 2D angular distribution graph in Figure 5.35 is very similar to Model_02 in Figure 5.14. The same material systems are used for the optimized case of Model_03, according to the 3D angular distribution of rays on Model_03 shown in Figure 5.36.

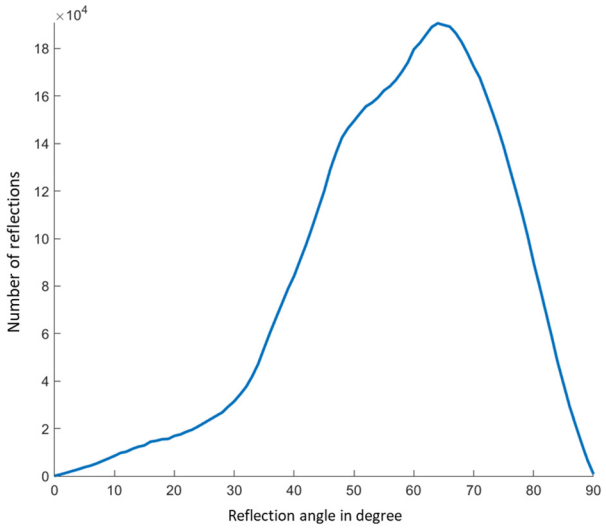

Figure 5.35 2D angular distribution of rays on Model_03

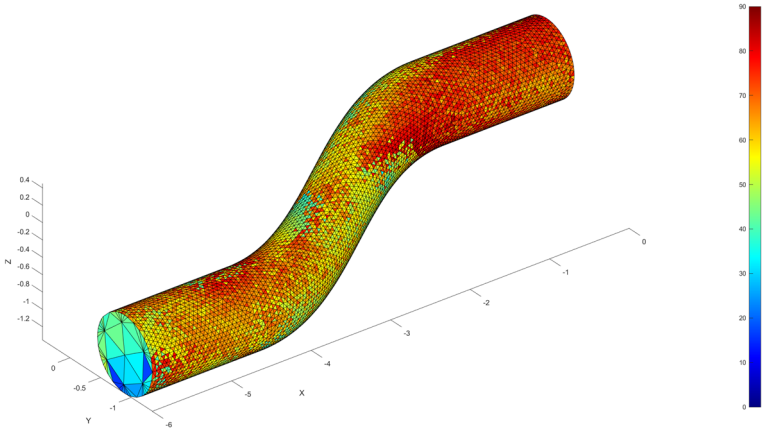

Figure 5.36 3D angular distribution of rays on Model_03

The RCS graphs of Model_03_RAM and Model_03_optRAM are illustrated in Figure 5.37 and Figure 5.38, respectively.

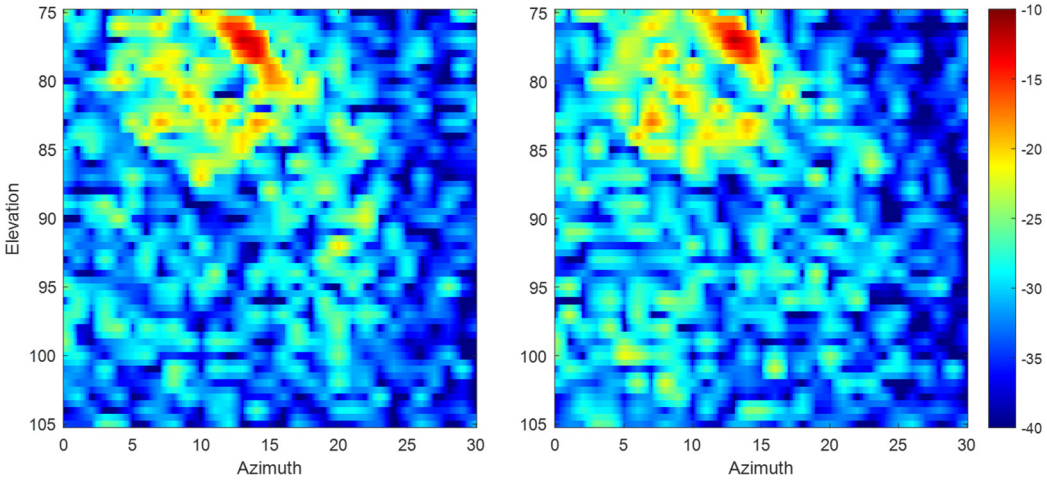

Figure 5.37 RCS graph of Model_03_RAM for VV (left) and HH (right) polarizations

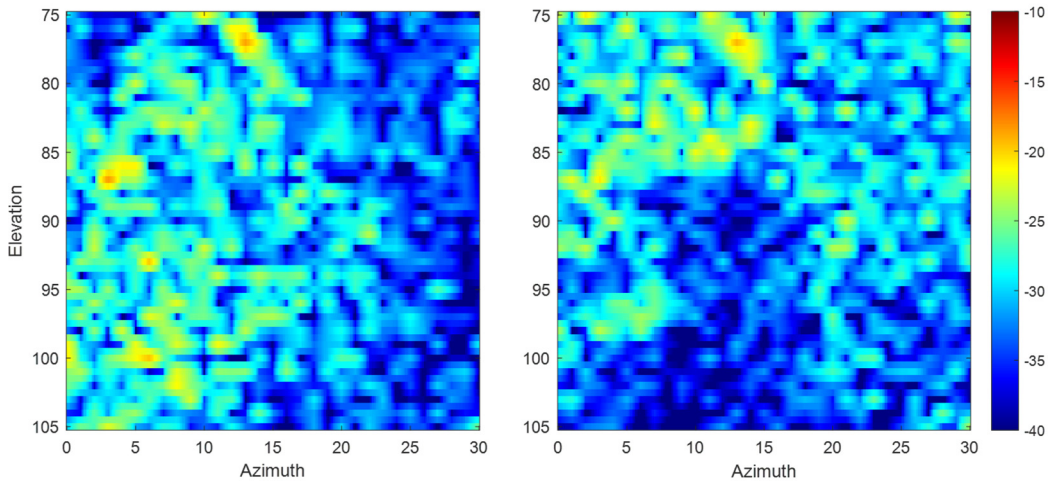

Figure 5.38 RCS graph of Model_03_optRAM for VV (left) and HH (right) polarizations

Figures show that the material optimization process improves the RCS performance, especially at the highest RCS points. The orange regions in Figure 5.37, around 13° azimuth and 77° elevation, have been eliminated in Figure 5.38. The second point seen in these figures is that the materials which are optimized for oblique incidences have absorption performance in only one of the co-polar polarizations, as in Figure 5.26. The polarization sensitivity could be seen in Figure 5.38, in which the bottom region of the graph is cleaner in HH polarization than the VV polarization. In some cases, it might be required to sacrifice one of the polarization.

The hypotheses are consistent so far:

- The average RCS is reduced when the minimum bounce number is increased. The minimum bounce numbers are 1 and 2 for Model_02 and Model_03, respectively. The average RCS values are reduced from -21.11 dBsm to -28.13 dBsm and from -21.59 dBsm to -28.15 dBsm for VV and HH polarization, respectively.
- The average RCS is reduced when the material absorption performance is optimized for the angle, which is observed primarily in the ray-tracing analysis. The average RCS values are given in Table 7. There are up to 4.65

dBsm differences in the average RCS values between the non-optimized and optimized material performances.

Table 7 Average RCS values in dBsm for different cases of Model_02 and Model_03

		VV				HH			
Model #	min. Refl. #	PEC	RAM	opt RAM	Δ	PEC	RAM	opt RAM	Δ
02	1	10.69	-21.11	-25.76	-4.65	10.52	-21.59	-24.67	-3.08
03	2	9.54	-28.13	-29.21	-1.09	9.59	-28.15	-29.76	-1.61

In the next step, the location of the bent is changed. The effect of bend location is observed and summarized in the next section.

5.6 Bend Location

Two new cavity models are designed to observe the effect of bend location. In Model_04, the bend is shifted forward, whereas the shift in Model_05 is towards the backward direction, as seen in Figure 5.39 and Figure 5.40. The rear face is not entirely obscured as in the previous models.

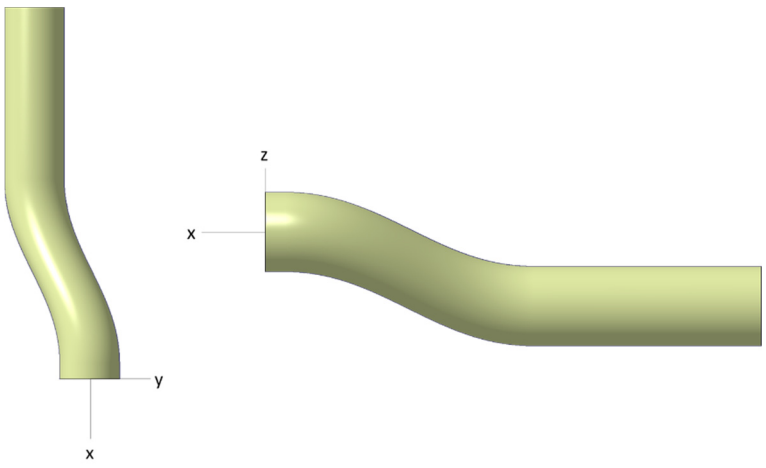

Figure 5.39 Top (left) and right side (right) views of Model_04

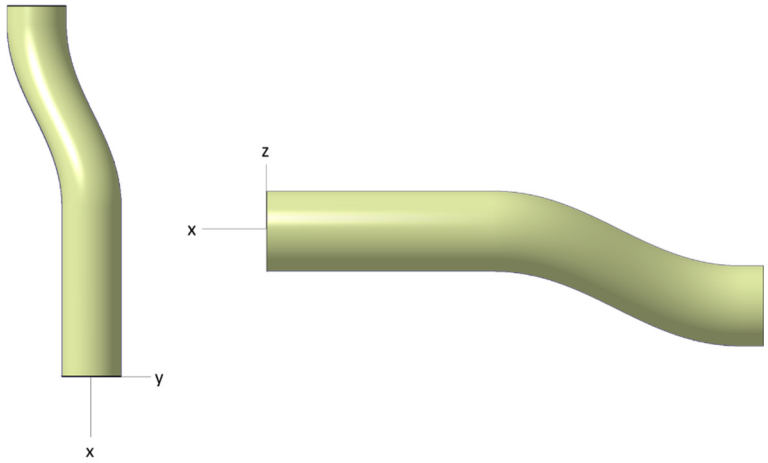

Figure 5.40 Top (left) and right side (right) views of Model_05

The same procedure is applied to Model_04 and Model_05:

- Ray-tracing analyses to determine the most observed reflection angle,
- Material optimization for the reflection angle determined in the previous step,
- RCS computation and comparison of PEC, coated and coated with optimized material cases.

The minimum bounce numbers are 2 and 3 for Model_04 and Model_05, respectively. The 2D angular distributions are pretty similar to the previous cases. The outputs of ray-tracing analyses and RCS simulations are illustrated in the following figures, Figure 5.41 and Figure 5.42.

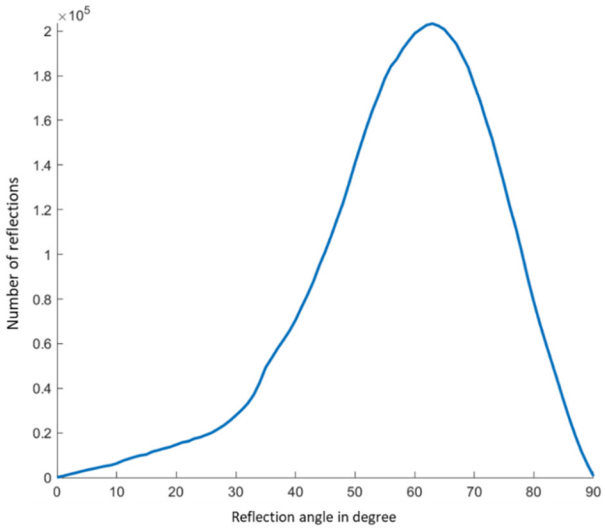

Figure 5.41 2D angular distribution of rays on Model_04

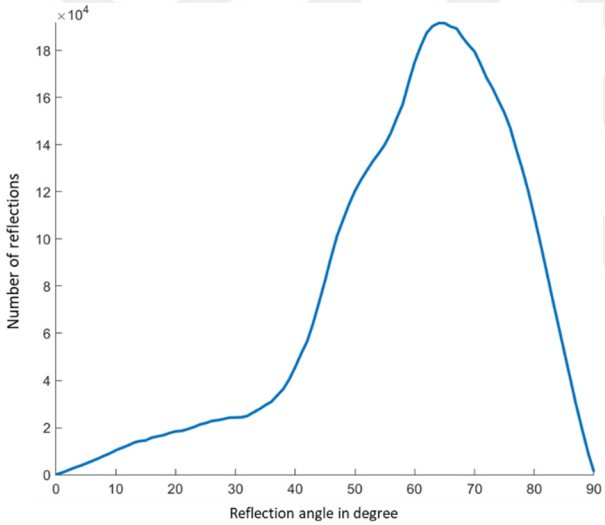

Figure 5.42 2D angular distribution of rays on Model_05

The most commonly observed reflection angles for Model_04 and Model_05 are the same, 65°. As seen in Figure 5.43 and Figure 5.44, the side surfaces of the straight sections have reflections around 65° or more mostly. The reflections from rear faces are more specular; material that is optimized for 15° reflection is used for both models' rear faces. For Model_05, the bend section is coated with a material that is optimized for 45° reflections. The 3D angular distributions and material application

zones are illustrated in Figure 5.43 and Figure 5.44 for Model_04 and Model_05, respectively.

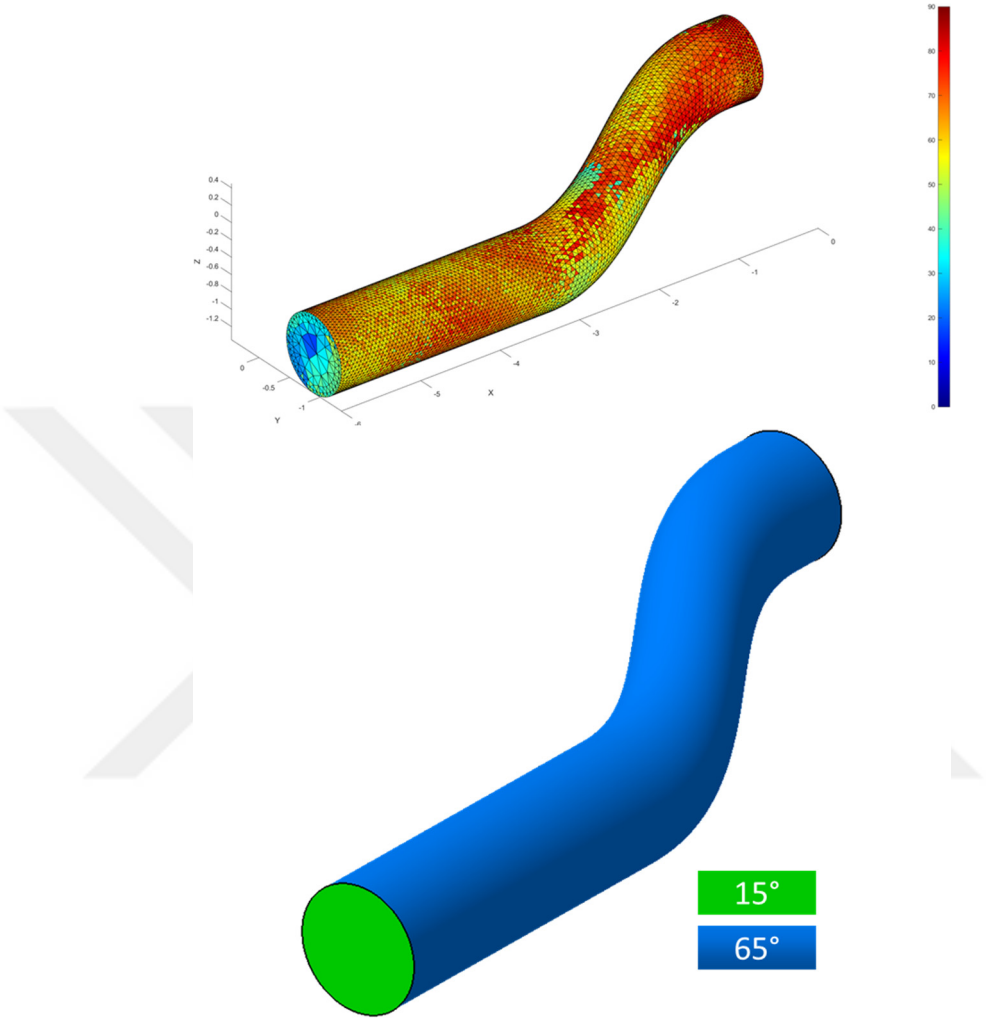

Figure 5.43 3D angular distribution (top) and material application zones (bottom) for Model_04

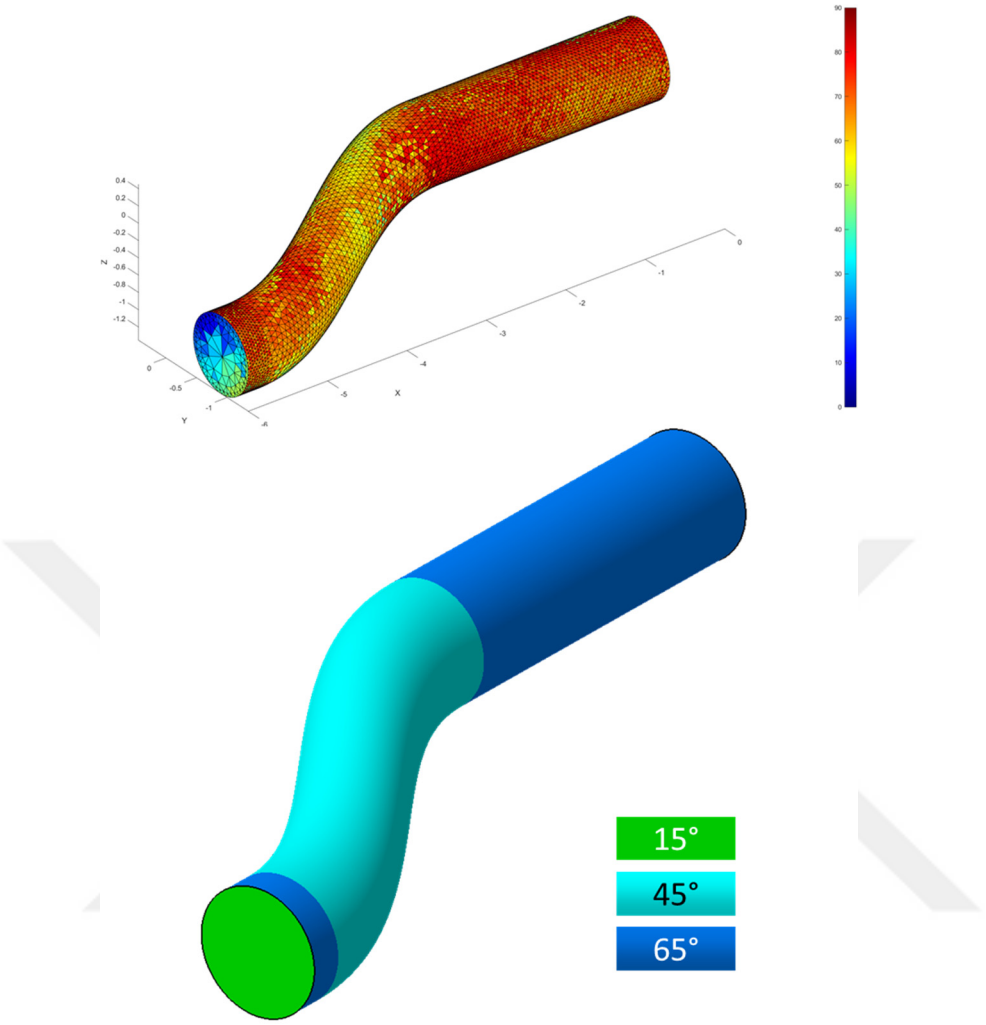

Figure 5.44 3D angular distribution (top) and material application zones (bottom) for Model_05

RCS analyses for Model_04 and Model_05 are run for the following cases: PEC, coated with specular reflection absorber and coated according to the material application zones defined above. The RCS graphs and the results table are shown on the next pages.

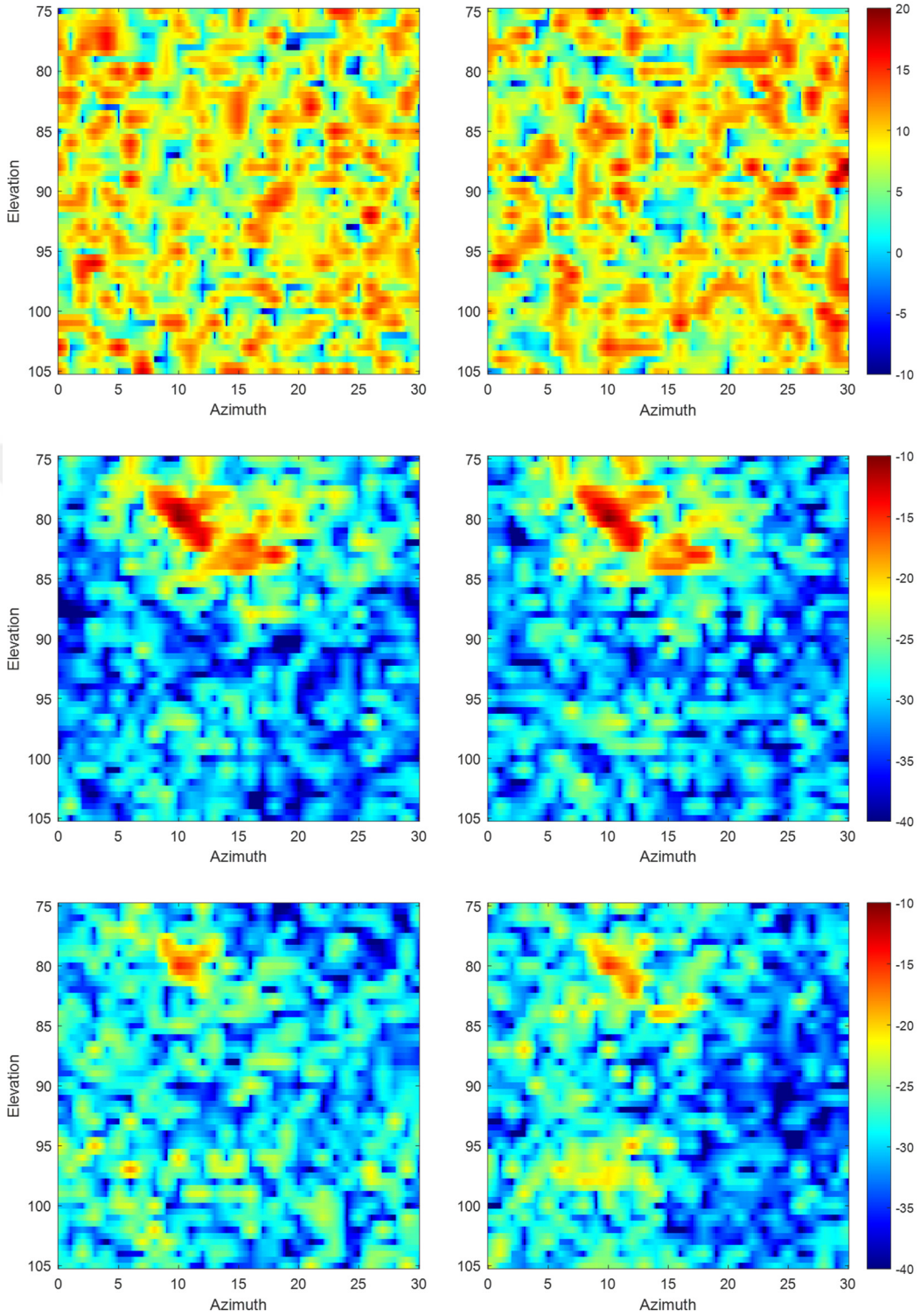

Figure 5.45 RCS graph of Model_04 (top), Model_04_RAM (middle), and Model_04_optRAM (bottom) for VV (left) and HH (right) polarizations

RCS graph of PEC Model_04 shows the high RCS values are not concentrated on a specific region but distributed over the angular interval like a high level of noise. In the Model_04_RAM case, there is a high RCS (~-10 dBsm) region around 10° azimuth and 80° elevation for both polarizations. The lower elevations are clear. In the Model_04_optRAM case, the RCS level of the high RCS region is reduced. As opposite, lower elevations are less clear than in the Model_04_RAM case.

The high RCS values are gathered around 10° azimuth and 82° elevation, as seen in the RCS graph of PEC Model_05. In the Model_05_RAM case, the highest RCS values (~-17 dBsm) are observed at 7° azimuth and 84° elevation for both polarizations. These regions have almost completely vanished in the Model_05_optRAM case.

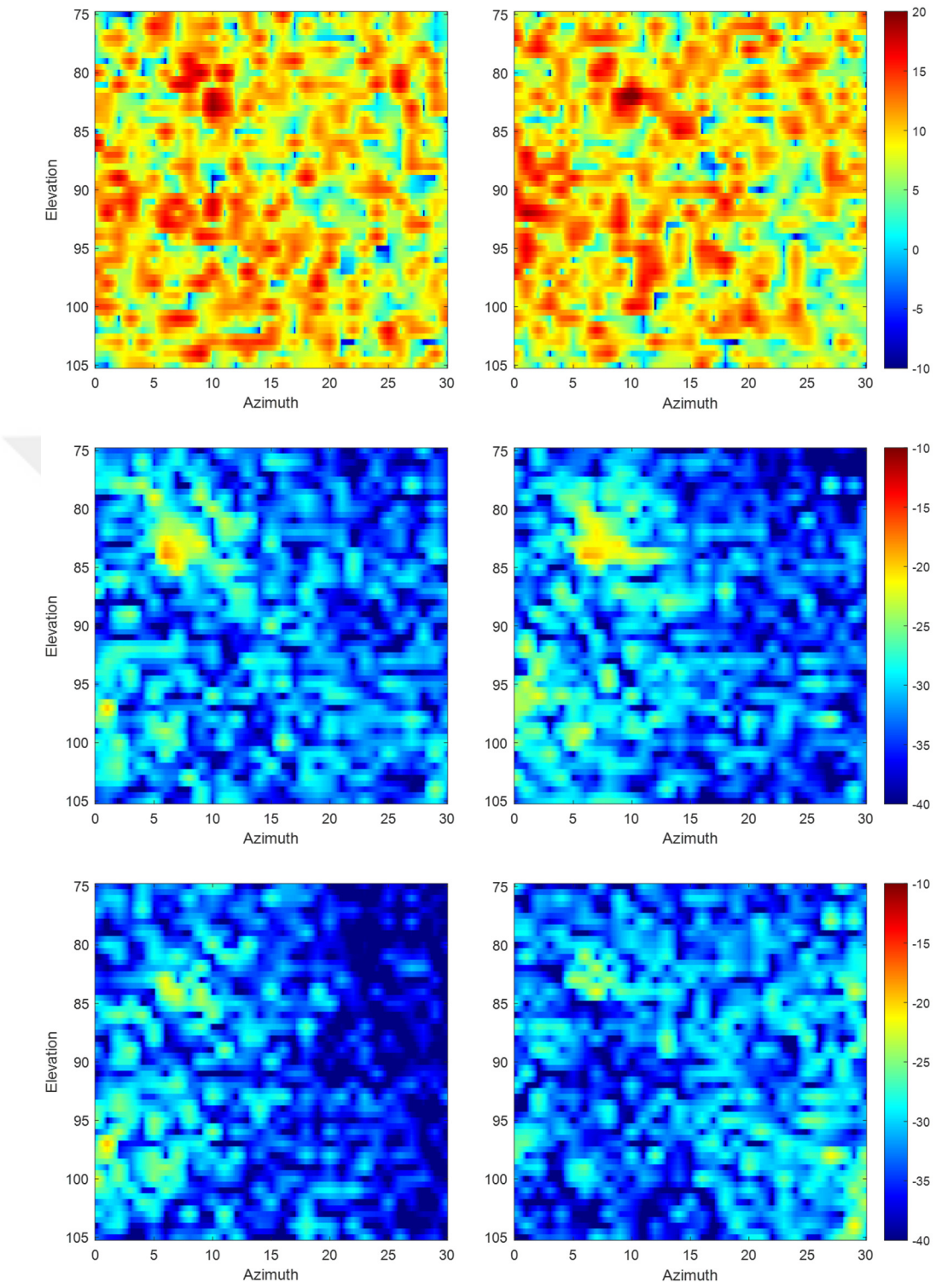

Figure 5.46 RCS graph of Model_05 (top), Model_05_RAM (middle), and Model_05_optRAM (bottom) for VV (left) and HH (right) polarizations

Table 8 Average RCS values in dBsm for different cases of Model_03, Model_04, and Model_05

		VV				HH			
Model #	min. Refl. #	PEC	RAM	opt RAM	Δ	PEC	RAM	opt RAM	Δ
03	2	9.54	-28.13	-29.21	-1.09	9.59	-28.15	-29.76	-1.61
04	2	8.96	-26.09	-27.67	-1.58	9.27	-26.28	-27.84	-1.56
05	3	10.05	-30.73	-32.33	-1.60	10.18	-30.62	-31.28	-0.67

For the models which have the same physical area, the average RCS values are around -26 or -28 dBsm when the models have two minimum bounces, whereas the average RCS value drops to -30 dBsm when the model has three minimum bounces.

The average RCS values are reduced by more than 1.5 dBsm with optimized materials for some cases. For Model_5, all average RCS values are less than -30 dBsm. The following assumptions show that -30 dBsm is a reasonable level of RCS of the duct of a stealth platform:

- Assumption 1: Assume that the RCS value of two ducts (-30 + 3 = -27 dBsm) is simply twice the RCS value of one duct,
- Assumption 2: The rest of the aircraft geometry has the same RCS contribution with two ducts (-30 + 3 + 3 = -24 dBsm),
- Assumption 3: The RCS contribution of antennae on the aircraft is the same as the RCS contribution of the whole aircraft with two ducts (-30 + 3 + 3 + 3 = -21 dBsm).

These assumptions approximately give a -21 dBsm average RCS value, which is an acceptable value for a 5th generation stealth aircraft.

In the next section, the slope of the bend is investigated. Three new models with higher slopes are analyzed, and the results are discussed with a fair comparison.

5.7 Slope of Bend

In the previous models with a bend in both y and z directions, the slope of the bend is determined as 0.3. This value is calculated from the ratio of offset in y or z directions (900 mm or 30λ) to the length of the slope in the x-direction (3000 mm or 100λ). The slope is increased by changing the length of the slope in the x-direction. The new length of the slope is determined as 2000 mm (200λ/3), which gives a 0.45 slope. Model_06 (Figure 5.47), Model_07 (Figure 5.48), and Model_08 (Figure 5.49) are the modified version of Model_03, Model_04, and Model_05, respectively.

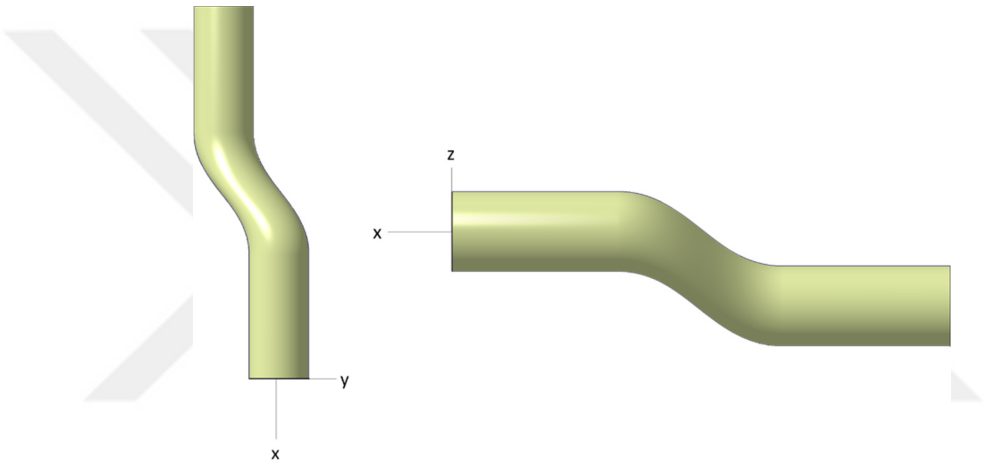

Figure 5.47 Top (left) and right side (right) views of Model_06

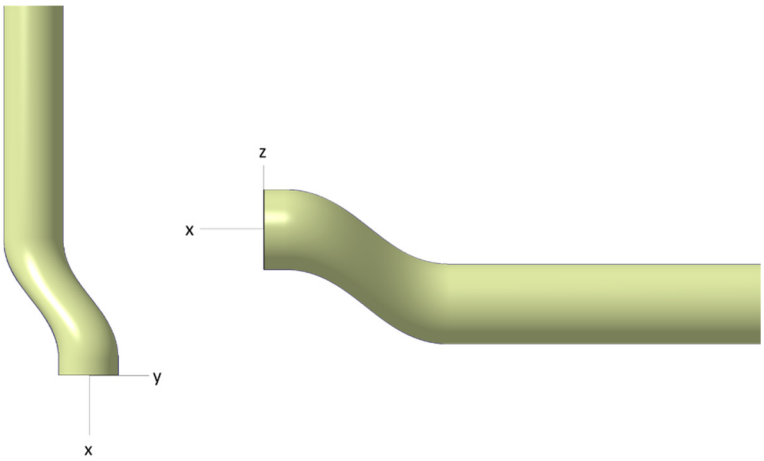

Figure 5.48 Top (left) and right side (right) views of Model_07

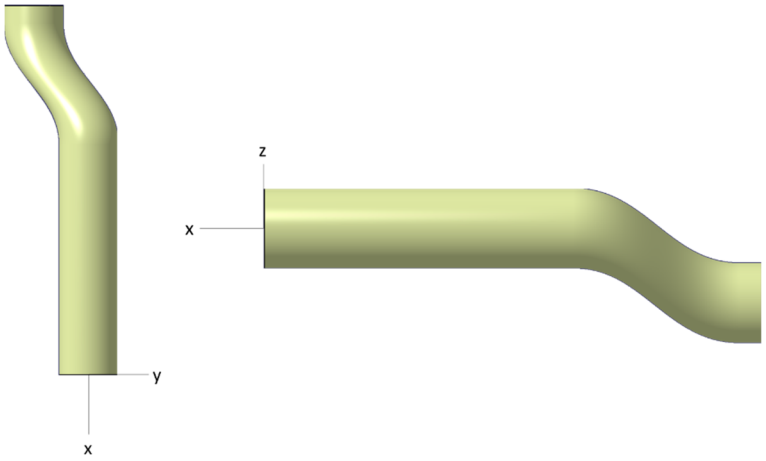

Figure 5.49 Top (left) and right side (right) views of Model_08

The process applied in the previous cases is repeated for these three new models. The optimum angles are determined by the ray-tracing algorithm to develop an optimized absorbing material. Models are analyzed in the developed SBR solver with PEC and coated with non-optimized and optimized materials options. At the end of the section, results are shared, and a brief comparison is made for different cases.

The 2D and 3D angular distributions for Model_06, Model_07, and Model_8 are shown in the following figures. The first thing that can be inferred from these 2D angular distribution plots (Figure 5.50, Figure 5.51, and Figure 5.52), there are two maxima points for all models, which are at 45° and 65°. The 3D angular distribution graphs (Figure 5.53, Figure 5.54, and Figure 5.55) show that 45° reflections occur around the bend section, whereas the 65° reflections are mainly observed at the surfaces of the straight sections of the cavity. Since the bends of these three models have a higher slope, the reflections become steeper, and as a result, new peak points have emerged at 45°.

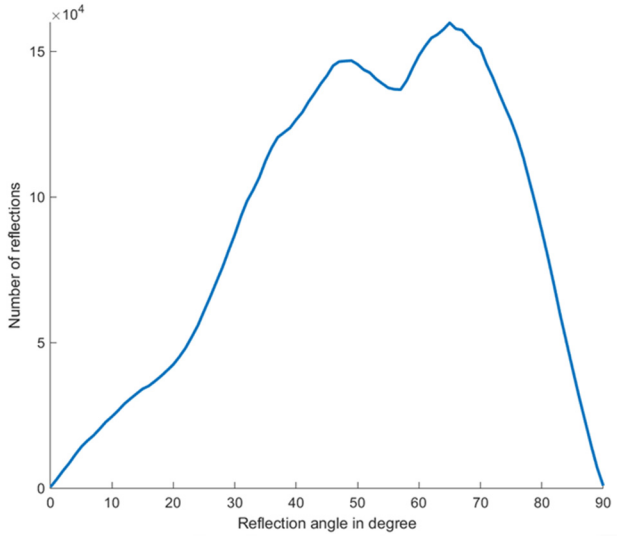

Figure 5.50 2D angular distribution of rays on Model_06

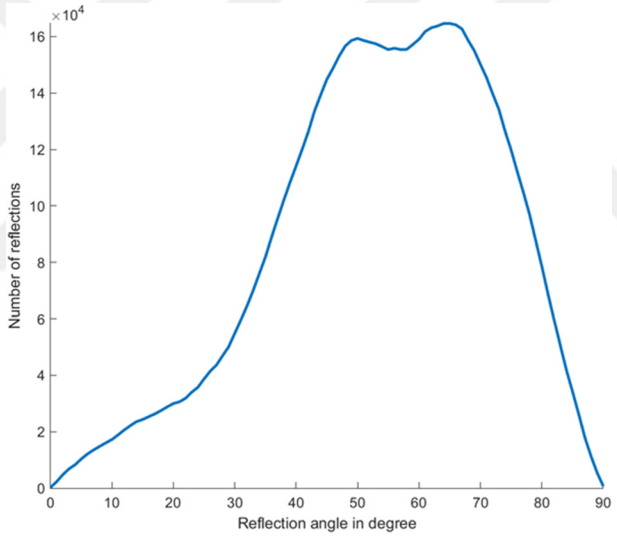

Figure 5.51 2D angular distribution of rays on Model_07

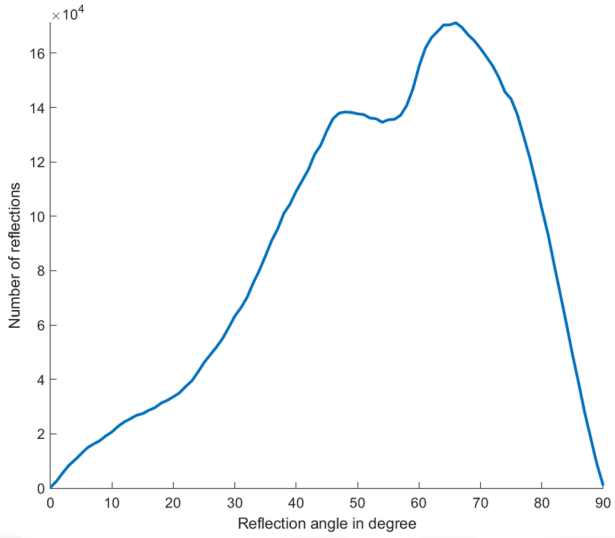

Figure 5.52 2D angular distribution of rays on Model_08

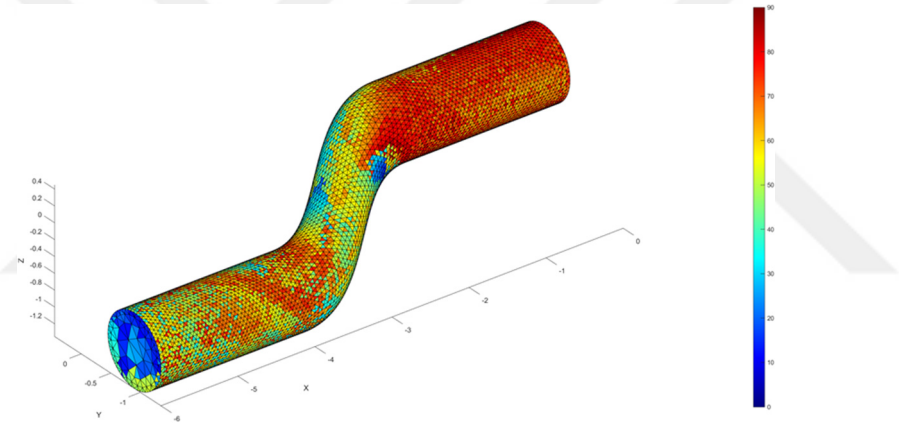

Figure 5.53 3D angular distribution of rays on Model_06

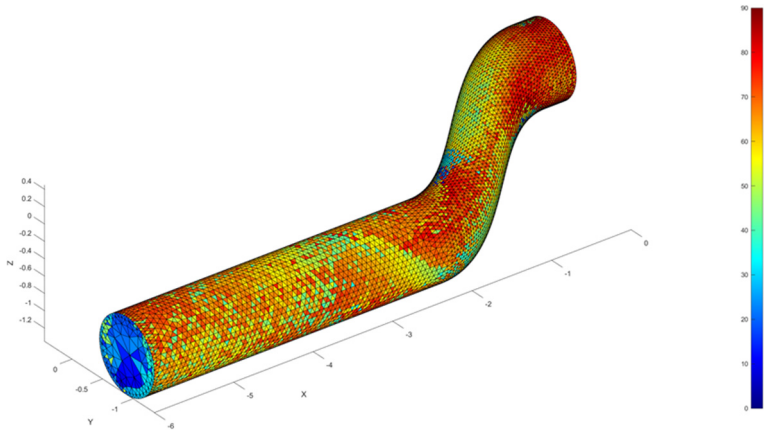

Figure 5.54 3D angular distribution of rays on Model_07

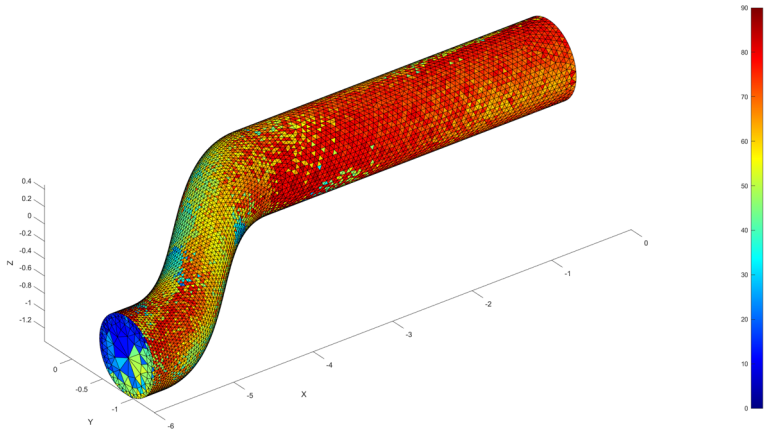

Figure 5.55 3D angular distribution of rays on Model_08

The minimum reflection numbers are two, two, and four for Model_06, Model_07, and Model_08, respectively. However, when these numbers are investigated, there is only one ray that has two reflections for Model_07, as in Figure 5.56. Practically, it can be said that Model_07 has a minimum of three reflections.

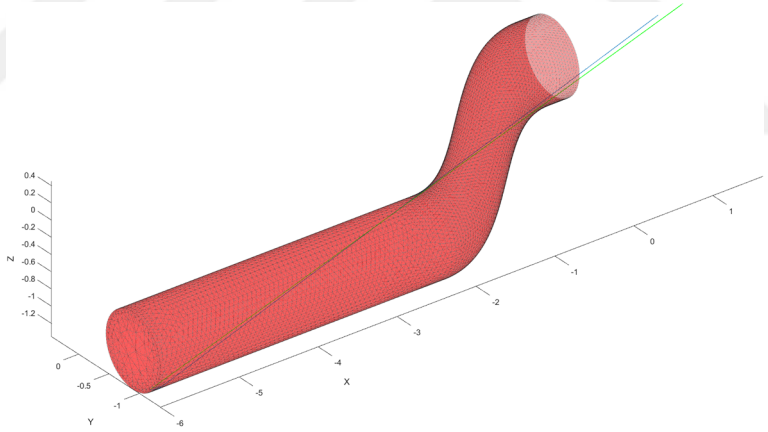

Figure 5.56 Shortest ray path with two reflections for Model_07

The material locations for these models are shown in Figure 5.57, Figure 5.58, and Figure 5.59 for Model_06, Model_07, and Model_08, respectively.

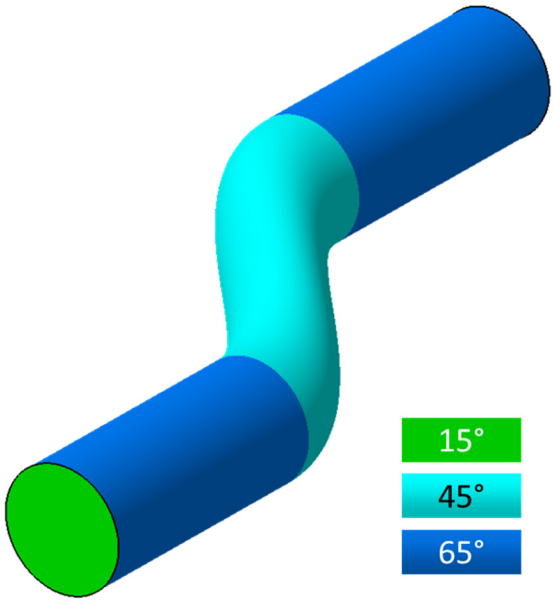

Figure 5.57 The material application zones for Model_06

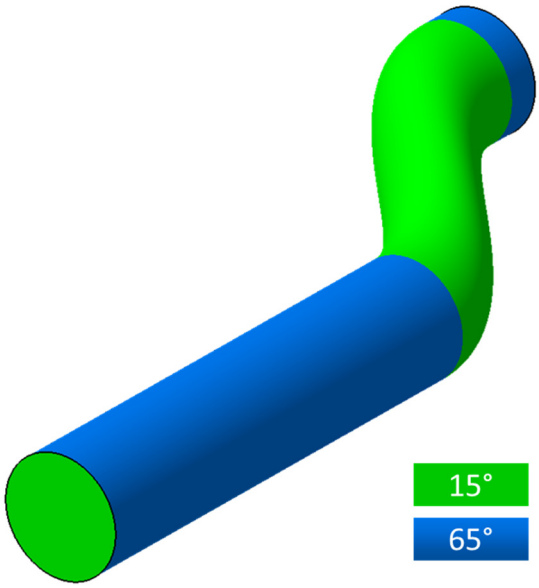

Figure 5.58 The material application zones for Model_07

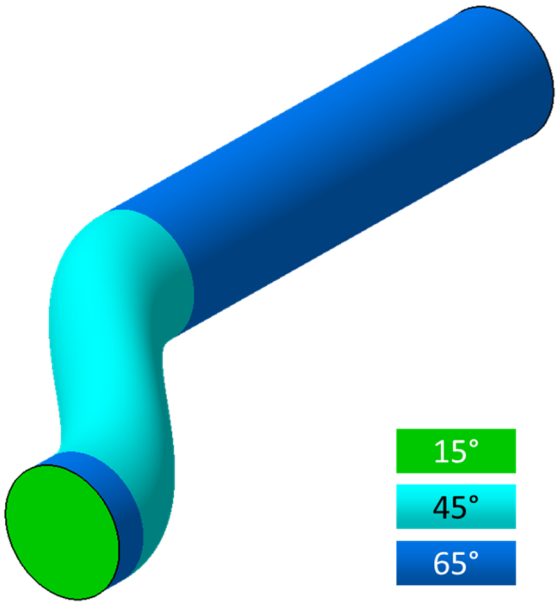

Figure 5.59 The material application zones for Model_08

The RCS graphs belonging to PEC, coated with specular absorber and coated with optimized absorber cases of these three models are given in Figure 5.60, Figure 5.61, and Figure 5.62. Then, the average RCS values are given in Table 9.

In the case of Model_06, the highest RCS points of VV and HH polarization of the PEC case are seen from the head-on angle. The RCS graphs are clean, even for the non-optimized material case. The same situation is observed in the PEC case for Model_07. The slightly higher RCS region at higher elevation angles for the non-optimized material case has vanished at the optimized material case. A similar high RCS region at the head-on angle is observed in Model_08. The material application provides a clean RCS graph. However, the material optimization study makes the RCS graph of HH polarization worse, especially at higher azimuth angles.

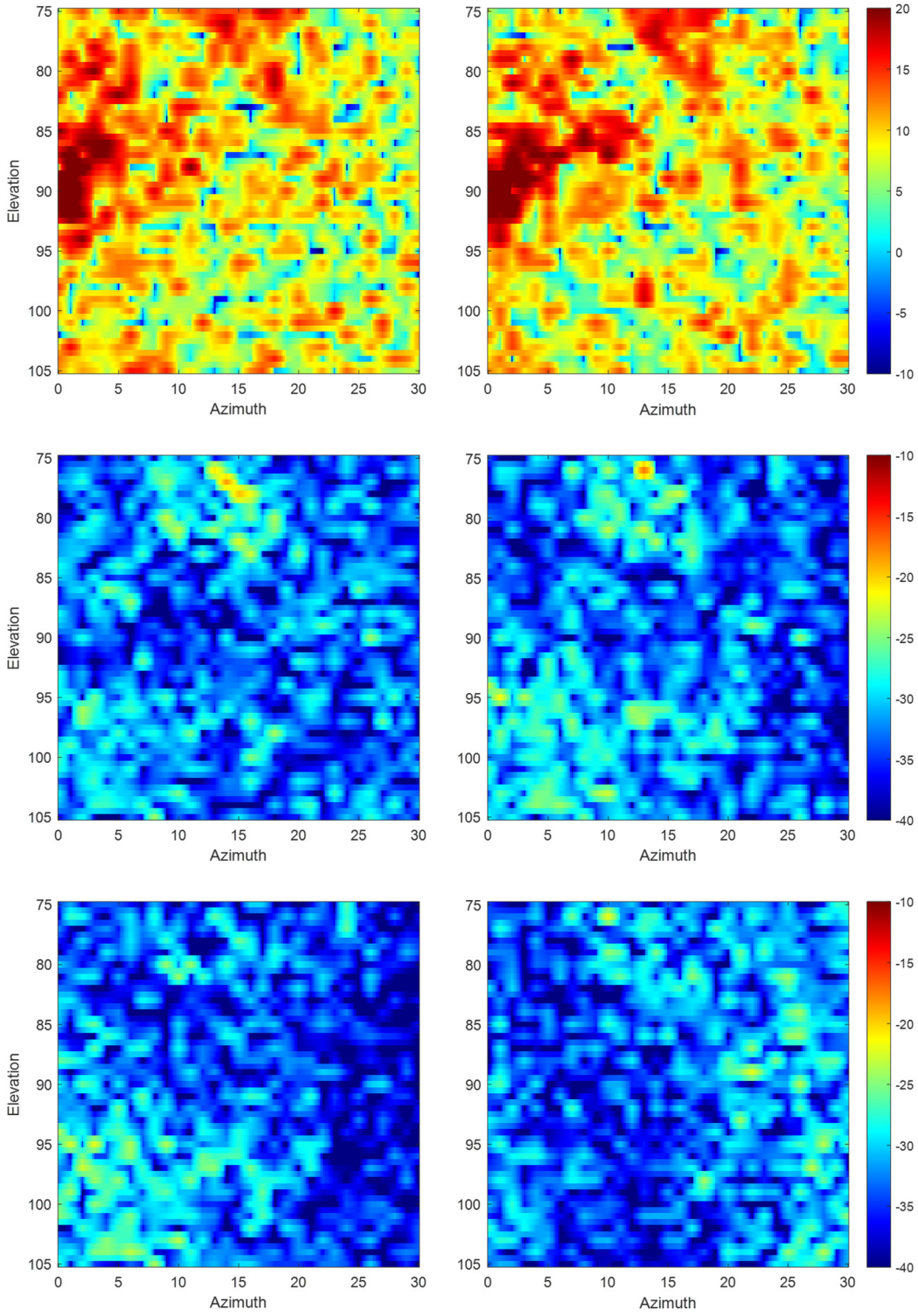

Figure 5.60 RCS graph of Model_06 (top), Model_06_RAM (middle), and Model_06_optRAM (bottom) for VV (left) and HH (right) polarizations

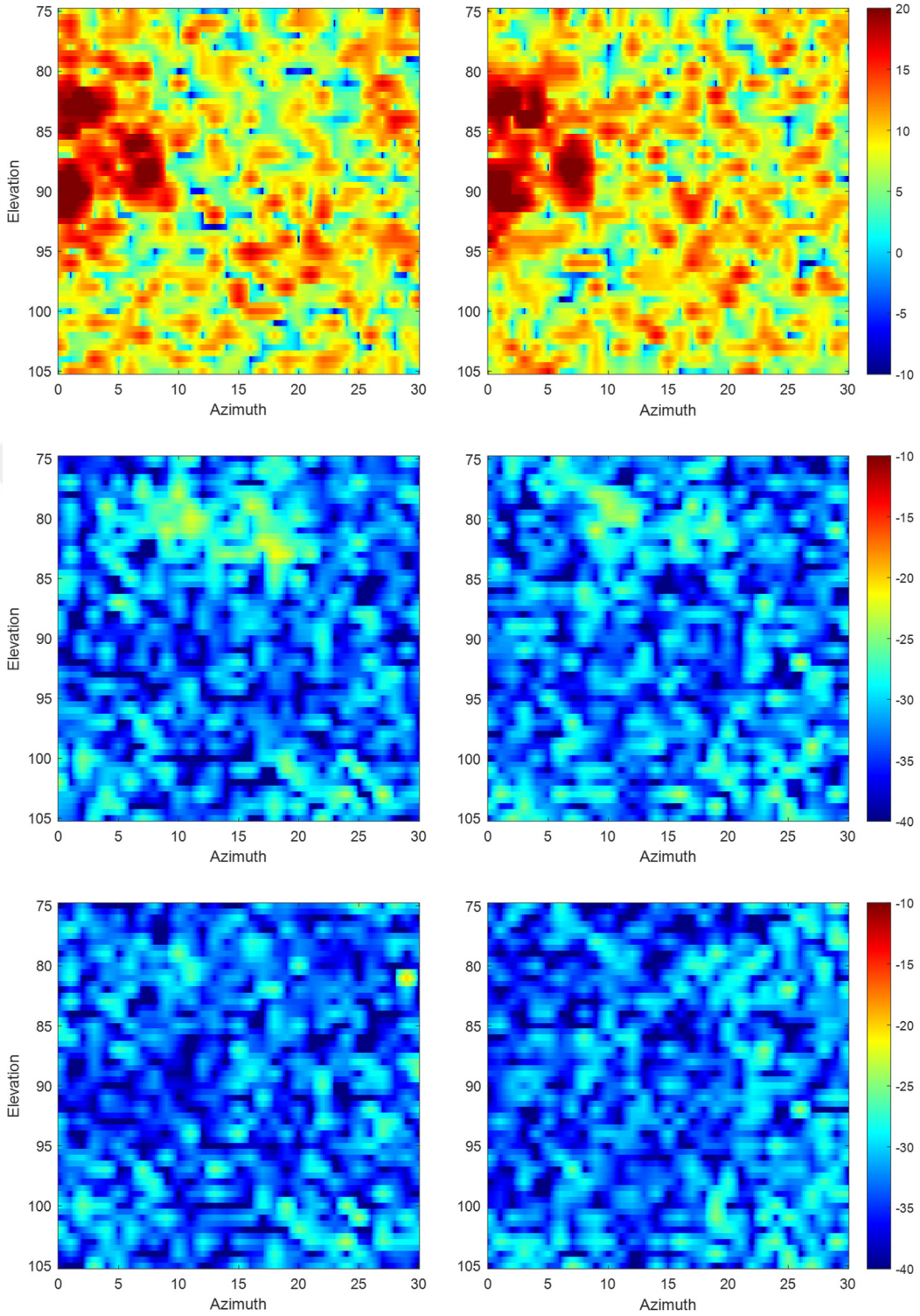

Figure 5.61 RCS graph of Model_07 (top), Model_07_RAM (middle), and Model_07_optRAM (bottom) for VV (left) and HH (right) polarizations

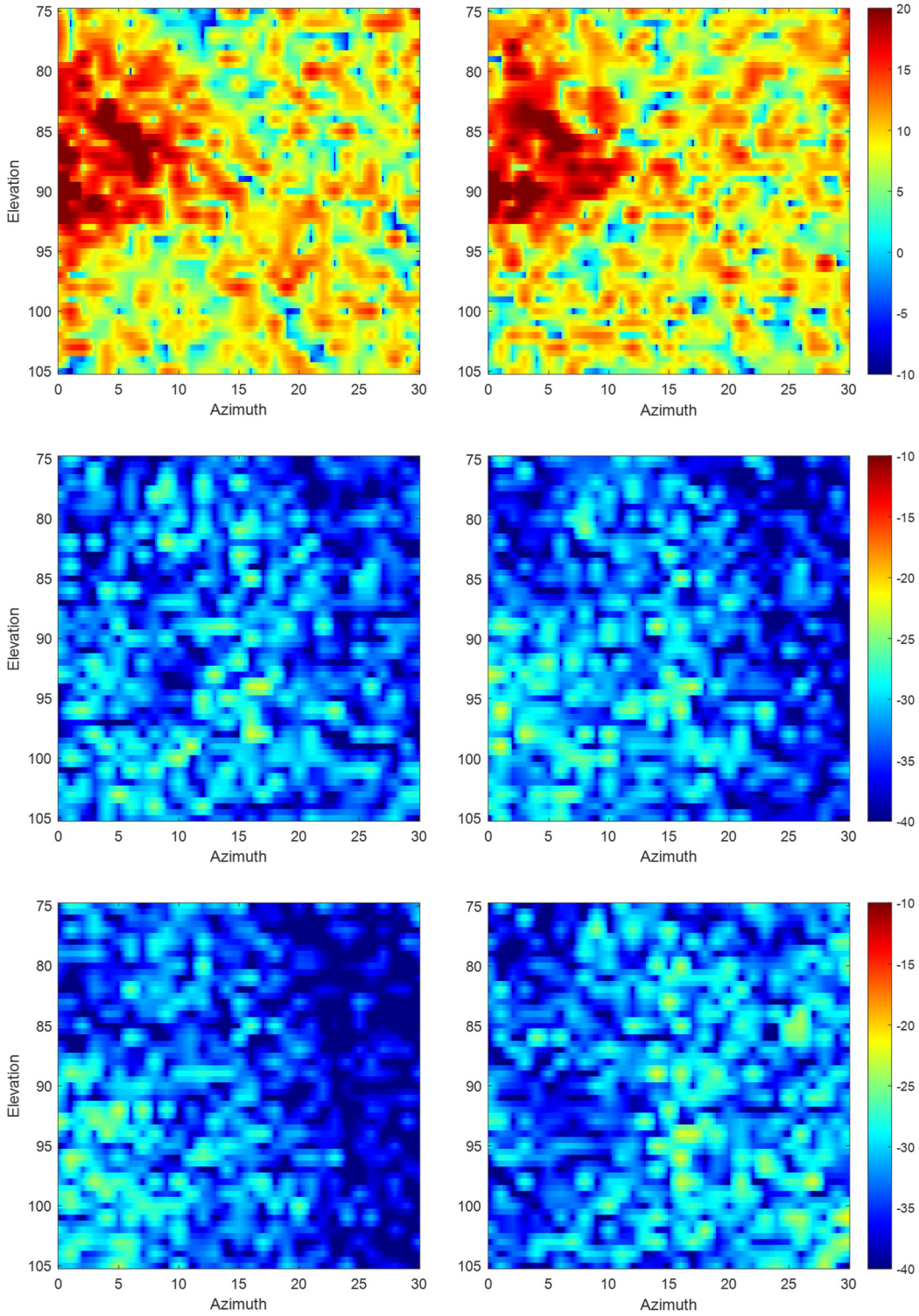

Figure 5.62 RCS graph of Model_08 (top), Model_08_RAM (middle), and Model_08_optRAM (bottom) for VV (left) and HH (right) polarizations

Table 9 Average RCS values in dBsm for different cases of Model_06, Model_07, and Model_08

		VV				HH			
Model #	min. Refl. #	PEC	RAM	opt RAM	Δ	PEC	RAM	opt RAM	Δ
06	2	11.54	-31.43	-32.03	-0.60	11.72	-31.19	-31.85	-0.65
07	2	11.52	-31.03	-32.33	-1.30	11.63	-31.17	-32.04	-0.87
08	4	11.88	-31.88	-32.81	-0.93	11.73	-31.91	-31.04	0.87

Table 9 shows the effect of bend location with a steeper bend. As in the previous case, in Table 8, the minimum bounce number is increased when the bent is located backward, as in Model_08. The smallest average RCS values are also obtained with Model_08, as expected, due to an increase in minimum bounce numbers.

Using optimized material gives better results in five of the six cases given in the table above. However, for Model_08, the average RCS value is increased from -31.91 dBsm to -31.04 dBsm. One possible reason could be the effect of the material performance at different polarizations, as shown in Figure 5.26. There is around 34 dB difference between the reflection coefficients at the optimized incident angle. Another possible reason is using an asymptotic method to calculate the RCS of the models. As mentioned before, high-frequency CEM solution methods are fast, but they have a drawback in terms of accuracy.

The effect of the slope of the bent can be investigated in Table 10. The steeper bend provides additional bounces, which provides better low observability performance. In the comparison of PEC cases, the RCS values are higher for the models that have a steeper bent. One of the possible reasons is the effect of specular reflection from the rear surfaces of the bent area. However, the average RCS values for coated cases are much smaller for the same models. The increase in the minimum reflection number provides more absorption.

Table 10 Average RCS results in dBsm for the effect of bend slope

		VV				HH			
Model #	min. Refl. #	PEC	RAM	opt RAM	Δ	PEC	RAM	opt RAM	Δ
03	2	9.54	-28.13	-29.21	-1.09	9.59	-28.15	-29.76	-1.61
06	2	11.54	-31.43	-32.03	-0.60	11.72	-31.19	-31.85	-0.65
04	2	8.96	-26.09	-27.67	-1.58	9.27	-26.28	-27.84	-1.56
07	2	11.52	-31.03	-32.33	-1.30	11.63	-31.17	-32.04	-0.87
05	3	10.05	-30.73	-32.33	-1.60	10.18	-30.62	-31.28	-0.67
08	4	11.88	-31.88	-32.81	-0.93	11.73	-31.91	-31.04	0.87

The absorption performance of the material optimized for 65° reflection is very limited for the specular reflections where the reflection angle is less than 30°. Additionally, since it is optimized for such an oblique incidence, the performance is not satisfactory for one of the polarizations. As a second iteration, the material application areas for Model_08 are updated as in Figure 5.63, and the new model is analyzed. The RCS graphs and the average RCS values are given on the following pages in Figure 5.64 and Table 11.

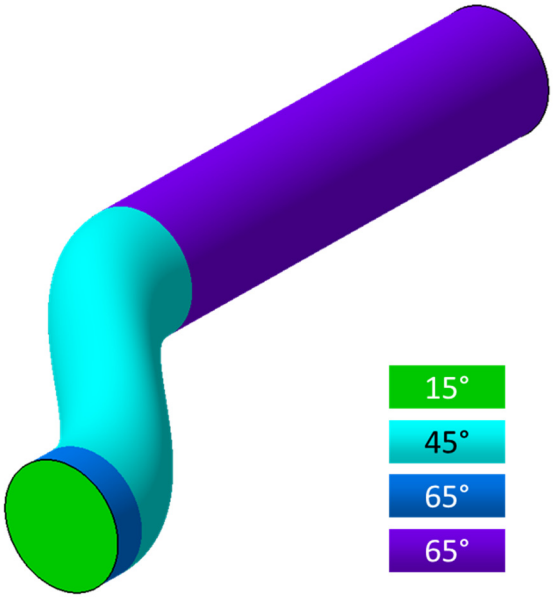

Figure 5.63 The second iteration of material application zones for Model_08

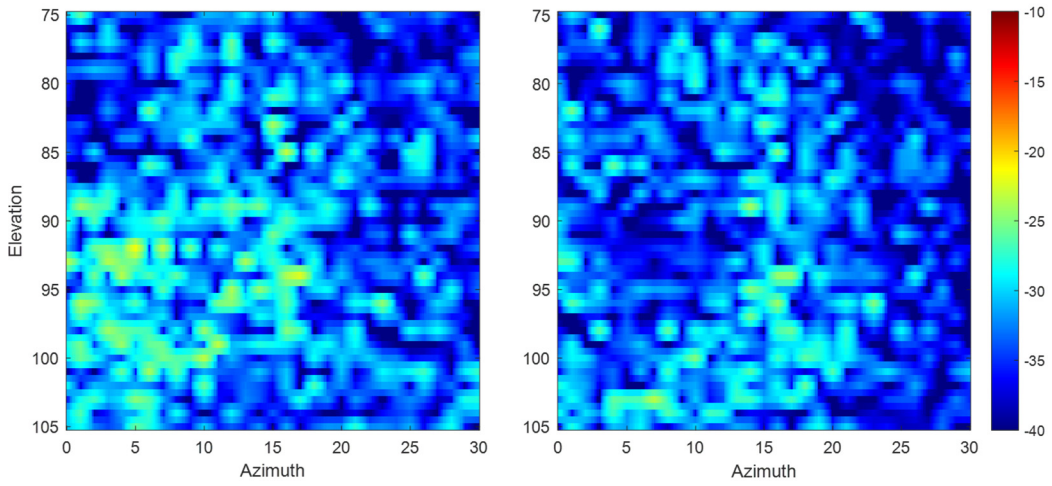

Figure 5.64 RCS graph of the second iteration of Model_08_optRAM for VV (left) and HH (right) polarizations

Table 11 The average RCS values in dBsm for different cases of Model_08

		VV				HH			
Model #	min. Refl. #	PEC	RAM	opt RAM	Δ	PEC	RAM	opt RAM	Δ
08	4	11.88	-31.88	-32.81	-0.93	11.73	-31.91	-31.04	0.87
08_v2	4	11.88	-31.88	-31.38	0.50	11.73	-31.91	-32.81	-0.90

The average RCS value of HH polarization for the second iteration of the Model_08_optRAM case is improved, as seen in Table 11. However, VV polarization becomes worse than in the non-optimized material application case. Within the limited material variation, the average RCS values of both polarizations for Model_08 cannot be reduced at the same time.

In general, RCS values for cross-polarization (VH and HV polarizations) are lower than RCS values for co-polarizations (VV and HH polarization). In this study, only co-polarizations are considered. For this specific case only, cross-polarization results are also calculated. The average RCS values are lower for all material application cases, including PEC cases in the cross-polarization, as given in Table 12. The 2D RCS graphs are given in Figure 5.65. The same situation is observed in the cross-

polarization cases as well. The optimized material works well when the incident field is polarized in the V direction (both VV and HV polarizations). In the updated material application case, Model_08_v2, the opposite polarization (HH and VH) gives better absorbance performance.

Table 12 The average RCS values in dBsm for both co-polarizations and cross polarizations of Model_08 and Model_08_v2

	Model_08				Model_08_v2			
Polarization	PEC	RAM	opt RAM	Δ	PEC	RAM	opt RAM	Δ
VV	11.88	-31.88	-32.81	-0.93	11.88	-31.88	-31.38	0.50
HH	11.73	-31.91	-31.04	0.87	11.73	-31.91	-32.81	-0.90
VH	10.61	-36.37	-35.06	1.31	10.61	-36.37	-36.55	-0.18
HV	10.57	-35.95	-37.60	-1.65	10.57	-35.95	-35.95	0.00

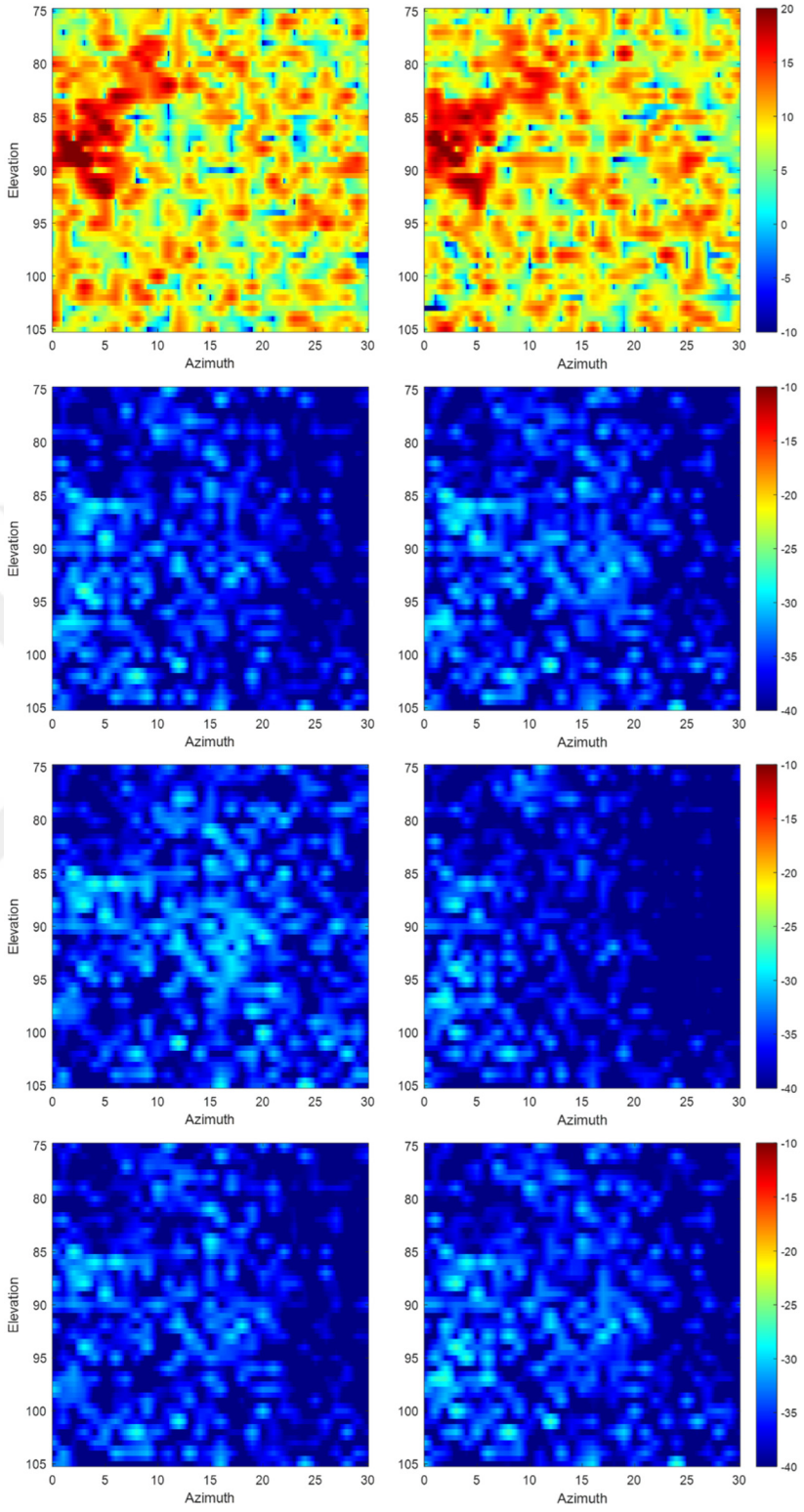

Figure 5.65 2D RCS graphs of VH (left) and HV (right) cross polarizations for Model_8 cases (top to bottom: PEC, RAM, opt_RAM, _v2_opt_RAM,)

CHAPTER 6

CONCLUSION

6.1 Overall Results

In the study, eight different models are analyzed with the developed SBR tool for PEC, coated with non-optimized material and coated with optimized material cases. All the results for average RCS values are listed in Table 13, including the difference in dB scale between the non-optimized and optimized coating cases.

Table 13 Average RCS values in dBsm for all cases

			VV				HH			
	Model #	min. Refl. #	PEC	RAM	opt RAM	Δ	PEC	RAM	opt RAM	Δ
MEAN RCS (dB)	01	1	21.25	-6.07	-10.48	-4.41	21.19	-6.08	-10.47	-4.39
	02	1	10.69	-21.11	-25.76	-4.65	10.52	-21.59	-24.67	-3.08
	03	2	9.54	-28.13	-29.21	-1.09	9.59	-28.15	-29.76	-1.61
	04	2	8.96	-26.09	-27.67	-1.58	9.27	-26.28	-27.84	-1.56
	05	3	10.05	-30.73	-32.33	-1.60	10.18	-30.62	-31.28	-0.67
	06	2	11.54	-31.43	-32.03	-0.60	11.72	-31.19	-31.85	-0.65
	07	2	11.52	-31.03	-32.33	-1.30	11.63	-31.17	-32.04	-0.87
	08	4	11.88	-31.88	-32.81	-0.93	11.73	-31.91	-31.04	0.87
	08_v2	4	11.88	-31.88	-31.38	0.50	11.73	-31.91	-32.81	-0.90

In some cases, the maximum RCS values are also provided in the text. All the results for maximum RCS values are listed in Table 14, including the difference in dB scale between the non-optimized and optimized coating cases.

Table 14 Maximum RCS values in dBsm for all cases

			VV				HH			
	Model #	min. Refl. #	PEC	RAM	opt RAM	Δ	PEC	RAM	opt RAM	Δ
MAX RCS (dB)	01	1	37.52	14.85	10.67	-4.17	37.52	14.85	10.67	-4.18
	02	1	23.65	-2.64	-7.40	-4.76	24.17	-2.43	-5.61	-3.18
	03	2	19.26	-11.77	-18.31	-6.54	19.71	-11.31	-19.18	-7.86
	04	2	17.67	-10.19	-14.74	-4.55	20.66	-9.83	-14.77	-4.94
	05	3	19.51	-17.83	-19.42	-1.59	21.33	-18.78	-21.09	-2.31
	06	2	28.12	-18.34	-21.88	-3.53	28.70	-17.38	-21.86	-4.48
	07	2	28.09	-21.41	-20.17	1.24	28.80	-22.46	-24.04	-1.58
	08	4	26.91	-22.39	-22.82	-0.43	25.80	-21.65	-21.27	0.38
	08_v2	4	26.91	-22.39	-21.62	0.78	25.80	-21.65	-23.44	-1.79

6.2 Discussions and Conclusion

A basic SBR code is written in the scope of this study. The ray-tracing process of the SBR algorithm is also used separately to get the statistical outputs of the traced rays. A C++ code and MATLAB GUI are developed to implement the ray-tracing procedure for cylindrical cavity models. The Möller-Trumbore algorithm is used for the ray-triangle intersection process. Mesh of the cavity model and parameters such as frequency, angular interval, ray density, reflection number limit, etc., are taken as input for the ray-tracing tool. Output is a text file that includes the point and direction information of each reflection. The output file is visualized using GUI. The main outputs are 2D and 3D angular distribution plots and the most critical ray paths. By the help of a post-process script, the RCS values for each azimuth and elevation pairs are computed.

The ray-tracing statistics are used to converge a model with lower RCS. Geometry is modified to increase the minimum number of reflections by inspecting the critical ray paths. In this study, a straight cylindrical cavity model is updated by adding a bend in only one direction. In the next step, an additional bend is required in another direction. As a final step, the slope of the bend is increased to have a higher number

of reflections. The overall absorption performance of the absorbing materials is improved by increasing the minimum reflection number. This first hypothesis is observed in many cases in this study. Average RCS values are reduced significantly from Model_02 to Model_03, Model_03 and Model_04 to Model_05, and Model_05 to Model_08, where the minimum reflection numbers are increased.

Absorbing material optimization for specific angles is the other way to improve the low observability performance of the cavities. 2D angular distribution graphs are used to determine the optimum angle for absorption. Several types of materials are designed to absorb the energy of electromagnetic waves for specific reflection angles and applied to the cavity models with the help of 3D angular distribution plots. The absorption performance of the absorbing materials at each reflection is improved by optimizing the absorbing material to the most commonly observed reflection angle. At the end of the process, the overall absorption performance of the absorbing materials is improved by improving the absorption performance for one reflection. This second hypothesis is observed in all the models used in this study. From Model_01 to Model_07, lower average RCS values are obtained for both linear polarizations, whereas lower RCS value is achieved only for one linear polarization of Model_08. By changing the coating material with better absorbance performance at the other polarization, the situation in average RCS values is also reversed.

Geometry and material optimizations have their own limitations. Geometric optimization of a cavity that is used on an air platform, specifically a fighter jet with high aerodynamic and maneuverability performance requirements, is a multidisciplinary process. The cavity models in this study are designed by ignoring the possible restrictions about these types of requirements. This study shows that the statistical outputs of the ray-tracing process, such as 2D and 3D angular distributions and critical ray paths, provide a chance to diagnose the reason for high RCS regions, and the whole process can be adapted for air vehicle level multidisciplinary cavity design optimizations.

In the material optimization process, the oblique incidences are the hardest cases to control. One of the polarizations should be selected for optimization, and the other one should be sacrificed for oblique incidences. As in the latest case, the application of non-optimized material for some specific region might reduce the average RCS values for one polarization (HH polarization in the second iteration of Model08_optRAM). Another point that needs to be mentioned is the effect of the cavities on the polarization performances. The cavities used in this study are cylindrical cavities. The direction of the E-field is changed as the wave propagates and reflects from the cavity surfaces. This yields an RCS reduction in an unpredicted polarization. For instance, the material has better absorption performance at HH polarization for oblique incidences, but the application of this material on cavity surfaces may reduce the RCS in VV polarization. Even with this uncertainty, the optimization angle can be decided by using the ray-tracing statistics, and two different materials can be optimized for the same reflection angle but with different polarizations to perform a trade-off study.

In the end, both hypotheses are investigated with eight different cavity models, and it is shown that the ray-tracing tool developed in the scope of this study provides a guideline to design a cavity model with a lower RCS average. The optimum duct cavity model for a stealth air platform could be obtained by integrating this method into the duct cavity design process with aerodynamic, structural, and other possible restrictions.

The optimum material application could be achieved with the help of the angular statistics derived by the ray-tracing tool. Weight and environmental effects are the main limitations of the material selections. The best absorption performance can be achieved by selecting the materials for optimum angles within these limitations. The ray-tracing tool developed in the scope of this study provides and visualizes the necessary information for these material performance and application optimization processes.

6.3 Future Works

In this study, the SBR tool with a separate ray-tracing procedure is developed to design a cavity geometry with better low observability performance. The ray-triangle process is the crucial point of the ray-tracing algorithm. The faster process can be implemented for future work by adding an octree structure to the ray-triangle intersection process [21]. Another way to improve the speed of the code is using parallel computation. Parallelization on CPU or GPU can be implemented as future work. These modifications allow using the code for air vehicle level ray-tracing analysis, not only a cavity.

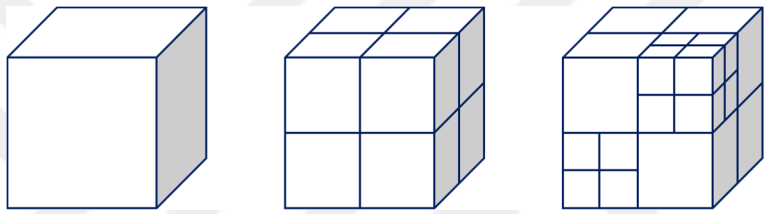

Figure 6.1 Octree structure for two levels

The developed code simulates the fields during the process. In the study, SBR method is used to calculate the RCS of the cavities. However, the effect of diffraction (PTD and UTD) and creeping waves are not included. The implementation of these methods makes the RCS values much more trustable.

In the SBR method, PO and GO are used for the field computation stage with far-field approximations. In the future, near-field interactions between the reflections that are not in the far-field zone can be investigated and implemented. There is a potential to make the SBR results closer to the full-wave results with this modification.

As a final touch, Inverse Synthetic-Aperture Radar (ISAR) images can be derived in the post-process stage. The required field data can be generated by the modified version of the tool developed in this study. ISAR images can be used to inspect the scattering centers by combining with the statistical outputs of ray-tracing procedures such as 3D angular distributions and hit maps. In conventional ISAR applications,

scattering from multi-reflections cannot be distinguished. The distance of the scattering center is calculated by using range profiles, but it is reflected in the ISAR image according to the incidence direction. However, for the cavities, there are components in other directions. A new method needs to be developed to map the scattering centers with multi-reflections to the correct locations.

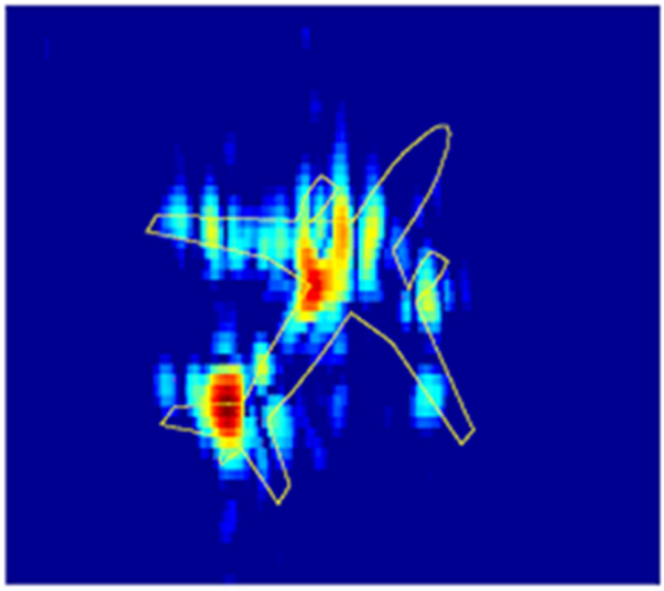

Figure 6.2 2D ISAR image example of an aircraft

REFERENCES

[1] C. A. Balanis, *Advanced Engineering Electromagnetics*, 2nd ed., AZ: John Wiley & Sons, 2012, pp. 22-29.

[2] J. Rautio, *The Long Road to Maxwell's Equations*, IEEE Spectrum, vol. 51, no. 12, 2014, pp. 36–56.

[3] E. F. Knott, J. F. Shaeffer and M. T. Tuley, *Radar Cross Section*, 2nd ed., NC: Scitech Publishing, 2004, pp. 23-360.

[4] I. Nicolaescu and T. Oroian, *Radar Cross Section*, 5th International Conference on Telecommunications in Modern Satellite, Cable and Broadcasting Service (TELSIKS 2001) Proceedings of Papers (Cat. No.01EX517), 2001, pp. 65-68, doi: 10.1109/TELSKS.2001.954850.

[5] IEEE Antennas and Propagation Society, Antennas and Propagation Standards Committee, "*IEEE Standard Definitions of Terms for Radio Wave Propagation*", in *IEEE Std 211-2018 (Revision of IEEE Std 211-1997)*, 2019, pp. 39-44, doi: 10.1109/IEEESTD.2019.8657413.

[6] M. Kuzuoğlu, *EE522 Numerical Methods for Electromagnetics: Computational Electromagnetics (CEM)*, Lecture Notes, Middle East Technical University, 2019, pp. 26-75.

[7] P. Sumithra and D. Thiripurasundari, "*A review on Computational Electromagnetics Methods*", in Advanced Electromagnetics, vol. 6, no. 1, 2017, pp. 42-55.

[8] K. Coburn, *Computational Electromagnetics*, Course Notes, Applied Technology Institute, 2019, pp. 14-36.

[9] H. Ling, R. Chou and S. Lee, *Shooting and Bouncing Rays: Calculating the RCS of an Arbitrarily Shaped Cavity*, IEEE Transactions of Antennas and Propagation, vol. 37, no. 2, 1989, pp. 194-205.

[10] D. Badouel, "*An Efficient Ray-Polygon Intersection*", in *Graphics Gems 1*, edited by A.S. Glassner, LA: Academic Press Professional, 1990, pp. 390-393.

[11] C. Erikson, *Real-Time Collision Detection*, CRC Press, 2005, pp. 46-52.

[12] T. Möller and B. Trumbore, *Fast, Minimum Storage Ray/Triangle Intersection* , Journal of Graphics Tools, vol. 2, no. 1, 1997, pp. 21-28.

[13] R. J. Segura, and F. R. Feito, *Algorithms to Test Ray-Triangle Intersection. Comparative Study*, The 9th International Conference in Central Europe on Computer Graphics, Visualization and Computer Vision (WSCG), 2001, pp. 76-81.

[14] D. Cross, *Fundamentals of Ray Tracing*, 2013, pp. 65-67.

[15] Altair Feko 2020 User Guide, 2020, pp. 655-695.

[16] Sun Studio 11 (Sun Microsystems Inc.), "*What Every Computer Scientist Should Know About Floating-Point Arithmetic*", in Numerical Computation Guide, 2003.

[17] Bruce Dawson, *Compairing floating point numbers*, Random ASCII – tech blog of Bruce Dawson, 2012, Accessed on: May 2021. [Online]. Available: https://randomascii.wordpress.com/2012/02/25/comparing-floating-point-numbers-2012-edition/

[18] M. Gibbs, *Memory Leaks in C++ Programming*, Study.com, 2018, Accessed on: May 2021. [Online]. Available: study.com/academy/lesson/memory-leaks-in-c-programming.html

[19] T. Naegele, D. Parham and M. Tsukamoto, *The B-2 at 30: Improving with Age*, Air Force Magazine (AFM), vol. 102, no. 6, 2019, pp. 31-34.

[20] ARC Technologies Technical Data Sheets, HITEK Electronic Materials Ltd., https://www.hitek-ltd.co.uk/tds-arc-technologies, Last visited on: 15.11.2021.

[21] J. M. Snyder and A. H. Barr, *Ray Tracing Complex Models Containing Surface Tessellations*, Computer Graphics, vol. 21, no. 4, 1987, pp. 119-128.

APPENDICES

A. ARC Technologies Technical Data Sheets

- UD-11738:

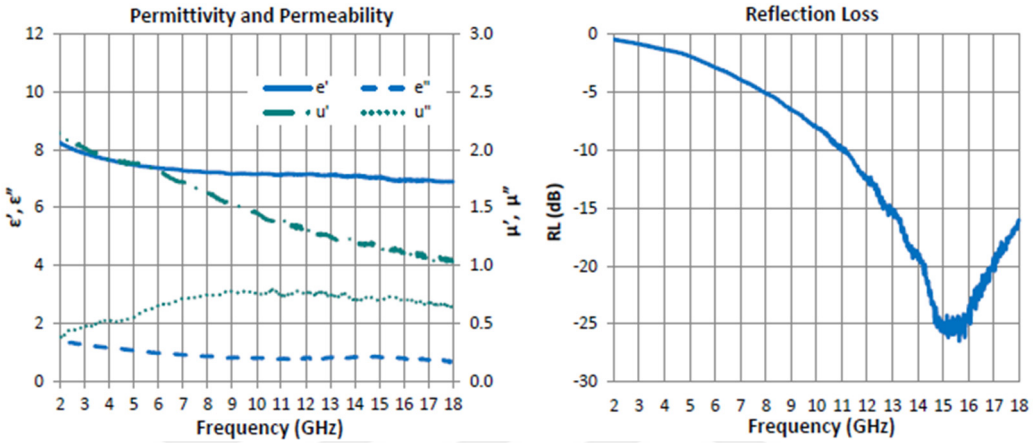

Figure 6.3 EM properties of UD-11738

- UD-14502:

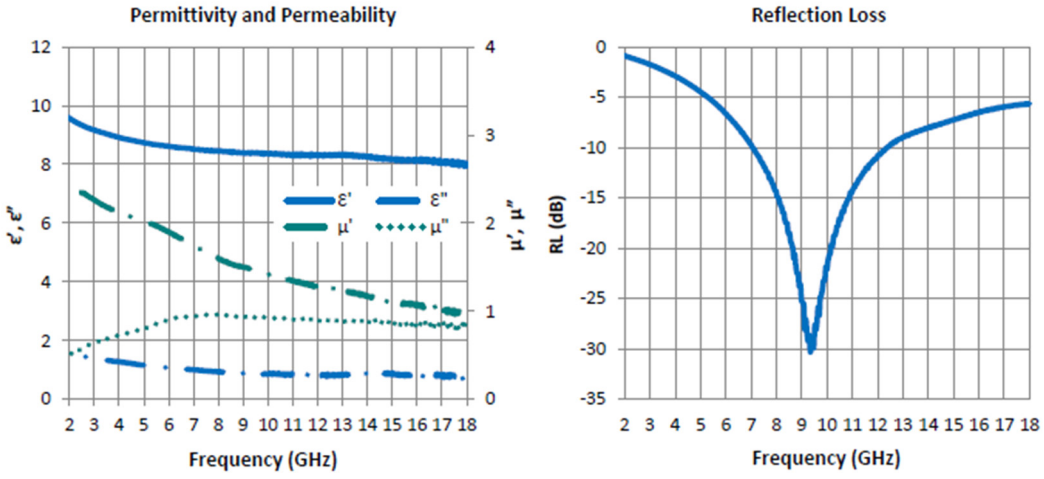

Figure 6.4 EM properties of UD-14502

- DD-10322:

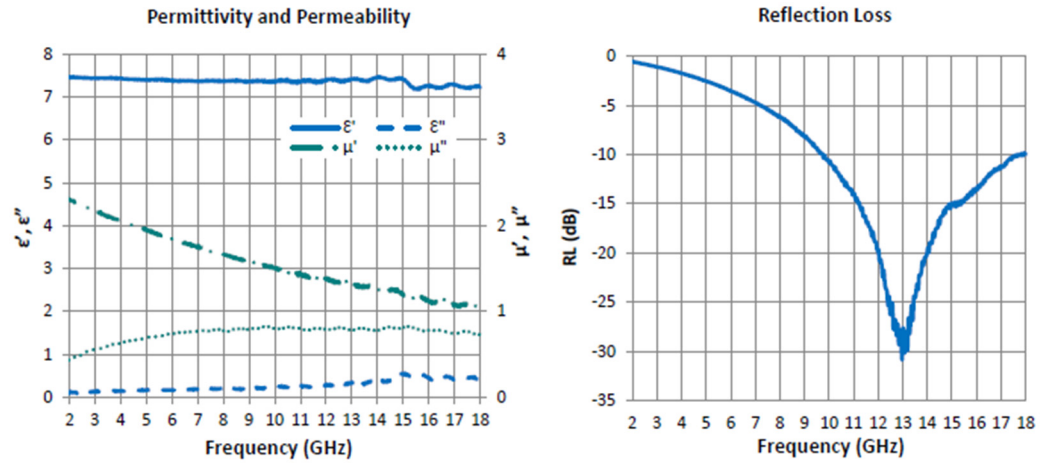

Figure 6.5 EM properties of DD-10322

- FD-12331:

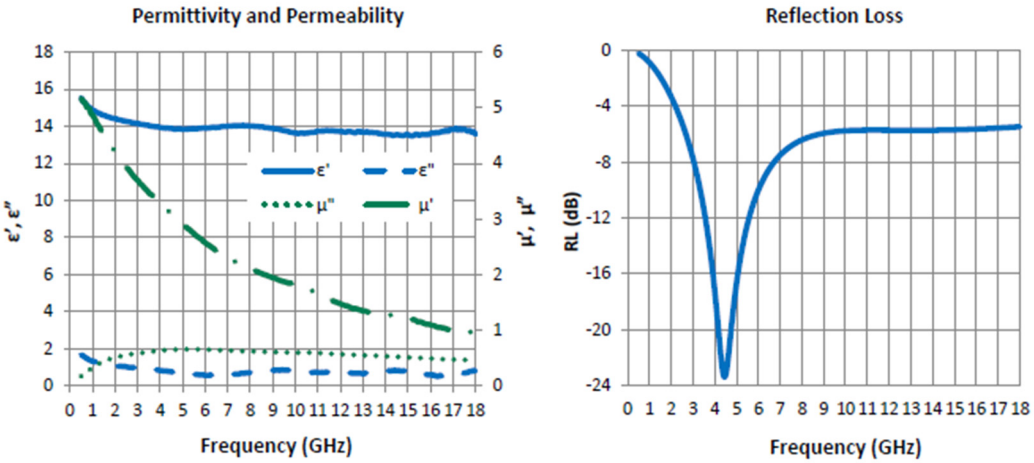

Figure 6.6 EM properties of FD-12331